The Clear-Sky Unpolarized Forward Model for the EOS Aura Microwave Limb Sounder (MLS)

William G. Read, Zvi Shippony, Michael J. Schwartz, Nathaniel J. Livesey, and W. Van Snyder

Abstract

This paper describes the Earth Observing System (EOS) Aura Microwave Limb Sounder (MLS) forward model for a clear sky atmosphere emitting unpolarized radiation. The viewing and orbital geometry of MLS on Aura enable a novel two dimensional (vertical and line-of-sight, horizontal) forward model that can be inverted in retrievals. Although the accuracy of the forward model is tunable subject to its approximations; in its current implementation, the accuracy is 0.2 K for the non-spectrally varying component plus a spectrally varying component which is the minimum of 0.2 K or 10% of the maximum line signal brightness.

Index Terms

Radiative Transfer, Spectroscopy

I. Introduction

The Microwave Limb Sounder (MLS) [1], [2] is one of four instruments on the Earth Observing System (EOS) Aura satellite that was placed into a near polar low Earth orbit on 15 July 2004. The Aura mission objective is to study the Earth's ozone, air quality, and climate. EOS MLS contributes to this objective by measuring temperature and several key molecules: O_3, H_2O, BrO, CH_3CN, ClO, CO, HCl, HCN, HNO_3, HO_2, HOCl, N_2O, OH, SO_2, and ice water content (IWC) of thick cirrus. The EOS MLS scans from 0 to 90 km; however, the expected useful vertical range of all these constituents is smaller; see [2] for more details.

This paper is a condensed synthesis of the EOS MLS forward model described in [3] used by the Level 2 software [4] to retrieve constituents from EOS MLS signals. It gives the appropriate forward model for a clear sky atmosphere

Manuscript received ???? ??, 2005; revised ???? ??, 2005. The work is done at the Jet Propulsion Laboratory, California Institute of Technology, under contract with the National Aeronautics and Space Administration.

W. G. Read, M. J. Schwartz, N. J. Livesey, and W. Van Snyder are with the Jet Propulsion Laboratory, Mail Stop 183-701, Oak Grove Drive, Pasadena, Ca. 91109.

Email: bill@mls.jpl.nasa.gov

Zvi Shippony, deceased, 24 July, 2002.

emitting unpolarized radiation. Extensions to include scattering for cirrus and polarization for mesospheric O_2 is given in companion papers [5], [6].

II. Measurement Description

The EOS MLS measures atmospheric thermal emission signals at specific frequencies between 118–2500 GHz (2500–120 μm). The EOS MLS instrument is a hetrodyne receiver where the incoming signal is combined with an internal frequency source called a local oscillator (LO). The intermediate frequency (IF) of the mixed signal is the absolute difference between the incoming signal and the LO. The IF signal is further mixed by internal oscillators, filtered and amplified. Except for the 118 GHz radiometer, MLS simultaneously measures signals having frequencies above and below its LO according to its IF. We refer to this pair of signals as sidebands. The 118 GHz radiometer is designed to reject the upper sideband. The spectral coverage showing deployment of bands is shown in Fig. 1. Radiometers and bands are deployed to optimize measurements of the targeted constituents [2].

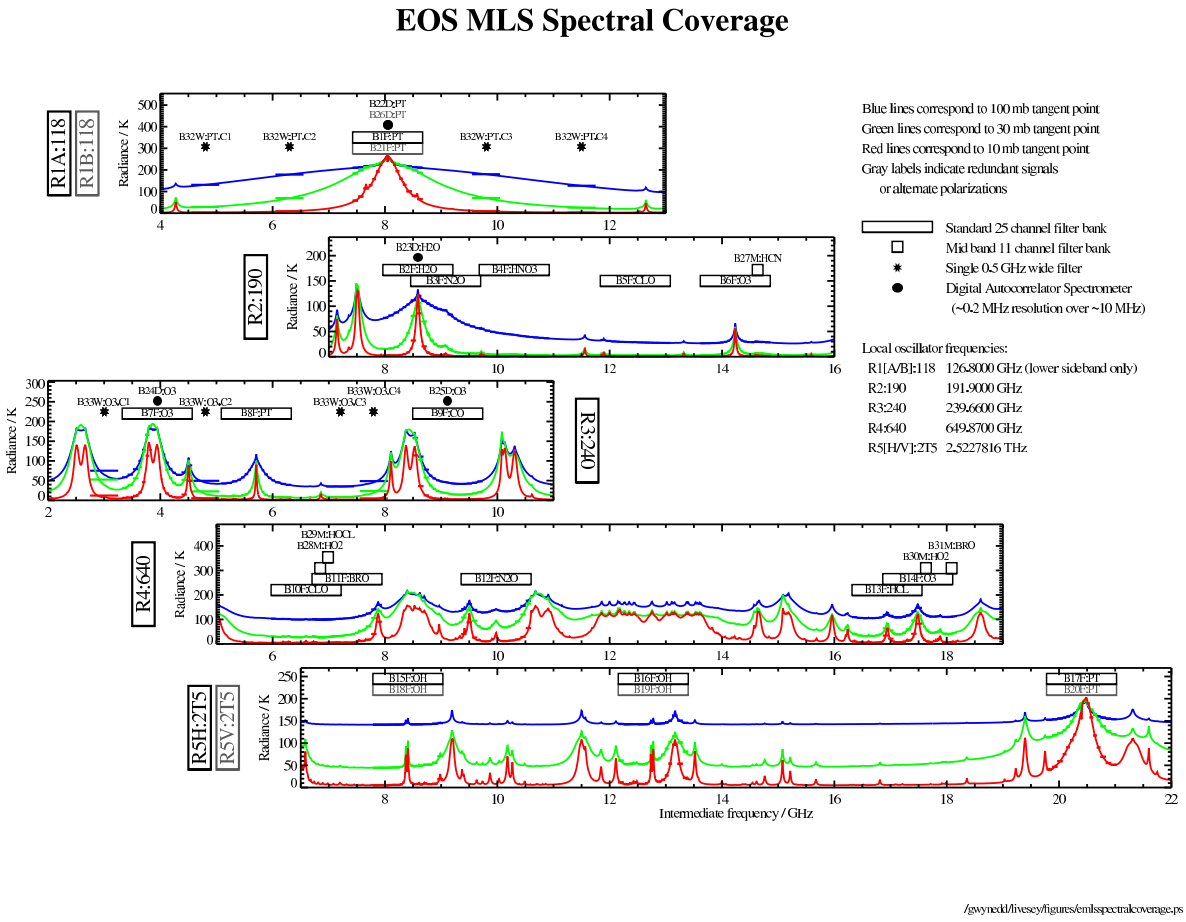

Fig. 1. Spectral regions measured by EOS MLS along with atmospheric signals at three limb tangent heights in these regions. This figure was prepared by Drs. N.J.Livesey and M.J.Filipiak and taken from [7]. The frequency scale is relative to the local oscillator and includes signals above and below the LO frequency except R1, which is designed only to receive frequencies less than the LO.

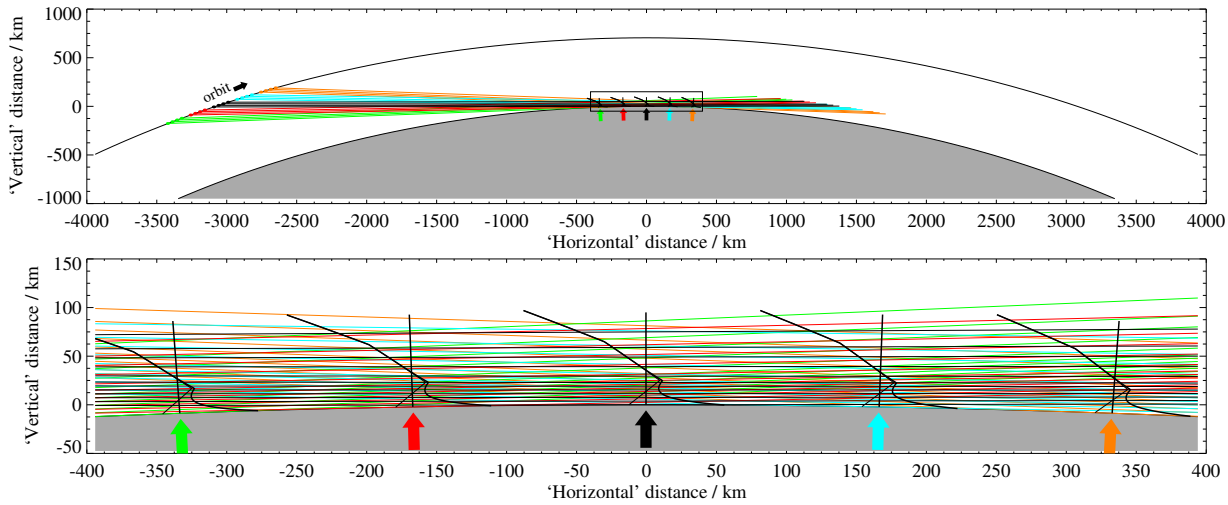

Fig. 2. The EOS MLS limb viewing geometry in the orbit plane. The top panel shows a large section of the Earth, which has been expanded in detail in the lower figure. The colored lines are measurements from a single scan whose tangent position is indicated by the colored arrow. The tangent locus is the thick zig-zag line on top of the thick vertical line, which represents the measured profile positions. The zig zag nature of the tangent loci is due to changes in scan rate and path refraction (the thin line underneath is the same without refraction). Notice that the lines of sight intersect several profiles (above the colored arrows) in each scan position. This figure is from [7].

Aura is in a sun-synchronous polar orbit (98.14° inclination at 705 Km). EOS MLS views forward and the measurement latitude covers 82°S to 82°N. Vertical resolution is achieved by measuring the radiation through a high-gain antenna that scans the atmospheric limb. A complete vertical scan takes 24.7 seconds and there are 240 scans per orbit or $\approx$ 3500 scans per day. The limb tangent of the scans proceeds from near the surface to 90 km in a continuous movement and measurements are taken every 1/6 second. The upward scan movement keeps the limb tangent point on a line that is nearly vertical to the Earth surface. The forward viewing geometry couples the vertical limb tangent measurements with horizontal line-of-sight (LOS) gradients. The measurement and the sampled atmosphere are confined to the same two dimensions (height and orbit track) as shown in Fig. 2, allowing vertical and horizontal gradients to be disentangled by the retrieval.

The signals received by EOS MLS are calibrated by viewing two scenes of known temperature. The instrument receivers periodically view an internal target, the Earths's limb, or cosmic space by rotating a mirror (switching mirror) that directs the receiver's field-of-view (FOV) at the desired scene. The internal target emits blackbody radiation according to its temperature which is continually monitored. Another view is looking at space away from the Earth and its atmosphere whose thermal temperature is 2.73 K [8]. These two views measure the signal strengths of two black body emitters of known temperature. The brightness of the signal recieved from the Earth's limb is determined from interpolation from measurements of the internal target and space as described in [9].

The EOS MLS forward model computes radiances (Level 1 calibrated signals) and radiance sensitivities to the two dimensional array of constituent profiles for the limb scans whose geometry is shown in Fig. 2. The process is as follows: 1) evaluates the atmospheric state (height, pressure, temperature, molecular compositions and volume

mixing ratio (VMR)) and atmospheric absorption for an ensemble of atmospheric LOS ray tracings, and frequencies, 2) solves the Schwartzchild radiative transfer equation for each member of the ensemble, 3) computes two channel radiances (one for each sideband) for several ray traced limb tangent heights weighting the radiance spectrum by the channel spectral response function and averaging, 4) for each channel sideband pair, computes the antenna radiance from a weighted average of the antenna gain response with the vertical radiance profile whose FOV directions for which the antenna averages are done are the measured limb tangent pressures, and 5) multiplies the two sidebands by their respective weights and adds them. The Aura spacecraft and the EOS MLS antenna scan encoder provide an independent limb tangent pointing measurement which can also be used to infer temperature and pressure. The scan residual model that links temperature and pressure to the limb tangent measurement is based on geometry and hydrostatic balance. Fig. 3 shows schematically how the forward model calculation is organized.

This paper is organized as follows: Section III gives the Level 1 data processing definition of a calibrated radiance, Section IV describes the profile representation and independent coordinates used in the forward model calculation, Sections V–XII describe the evaluation of the radiance forward model, Section XIII describes the scan residual model, Section XIV is a summary list of approximations made by this forward model and a simple estimate of its accuracy, Section XV describes the level 2 processing coefficients file which is linear representation of the radiance forward model, Section XVI shows some examples of measured and modeled spectra, and Section XVII describes how the forward model profile representation smoothes the true atmospheric profile.

III. Measurement Definitions

A. EOS MLS Radiance

Level 1 processing [9] produces radiances from instrument engineering data (Level 0). The Level 1 calibrated radiance is,

$$\left(\overset{\bullet}{I}-I_{\mathrm{bl}}\right)_{\mathrm{R,c}}(\mathbf{x}) = \mathrm{BL}_{\mathrm{R},t} + \frac{1}{t_2-t_1}\int_{t_1}^{t_2}\mathrm{d}t \times \left\{ r_{\mathrm{u,R,c}} \frac{\int_{\nu_{\mathrm{lo,R}}}^{\infty}\int_{\Omega_A} I\left(\nu,\mathbf{x}\left(\Omega\right)\right)\Phi_{\mathrm{R,c}}\left(\nu\right)G\left(\Omega,\Omega_t\left(t\right),\nu\right)\mathrm{d}\Omega\mathrm{d}\nu}{\int_{\nu_{\mathrm{lo,R}}}^{\infty}\int_{\Omega_A}\Phi_{\mathrm{R,c}}\left(\nu\right)G\left(\Omega,\Omega_t\left(t\right),\nu\right)\mathrm{d}\Omega\mathrm{d}\nu} + r_{\mathrm{l,R,c}}\frac{\int_{-\infty}^{\nu_{\mathrm{lo,R}}}\int_{\Omega_A} I\left(\nu,\mathbf{x}\left(\Omega\right)\right)\Phi_{\mathrm{R,c}}\left(\nu\right)G\left(\Omega,\Omega_t\left(t\right),\nu\right)\mathrm{d}\Omega\mathrm{d}\nu}{\int_{-\infty}^{\nu_{\mathrm{lo,R}}}\int_{\Omega_A}\Phi_{\mathrm{R,c}}\left(\nu\right)G\left(\Omega,\Omega_t\left(t\right),\nu\right)\mathrm{d}\Omega\mathrm{d}\nu} \right\}, \quad (1)$$

where $\left(\overset{\bullet}{I}-I_{\mathrm{bl}}\right)_{\mathrm{R,c}}(x)$ is the Level 1 calibrated radiance at the switching mirror with a correction for additional primary antenna system emissions [10] for band/channel, c, in radiometer R, $\mathrm{BL}_{\mathrm{R},t}$ is a radiometer dependent additive baseline when the instrument is pointing at limb tangent, subscript t, $r_{\mathrm{u,R,c}}$ is the higher frequency relative to the local oscillator (LO) frequency $\nu_{\mathrm{lo,R}}$ side band fraction, $r_{\mathrm{l,R,c}}$ is the lower sideband fraction, $I\left(\nu,\mathbf{x}\left(\Omega\right)\right)$ is the limb radiance, $\Phi_{\mathrm{R,c}}\left(\nu\right)$ is the instrument spectral response, $G\left(\Omega,\Omega_t\left(t\right),\nu\right)$ is the antenna response or FOV, ν is frequency, $\mathbf{x}$ is the state vector, Ω is solid angle, $\Omega_t\left(t\right)$ is the FOV direction and varies with time, t, during the measurement, a consequence of the continuous scan, and Ω_A is that portion of solid angle for which $G\left(\Omega,\Omega_t\left(t\right),\nu\right)$ is measured. The integrals in the denominator of (1) are normalizations of instrument response functions and are

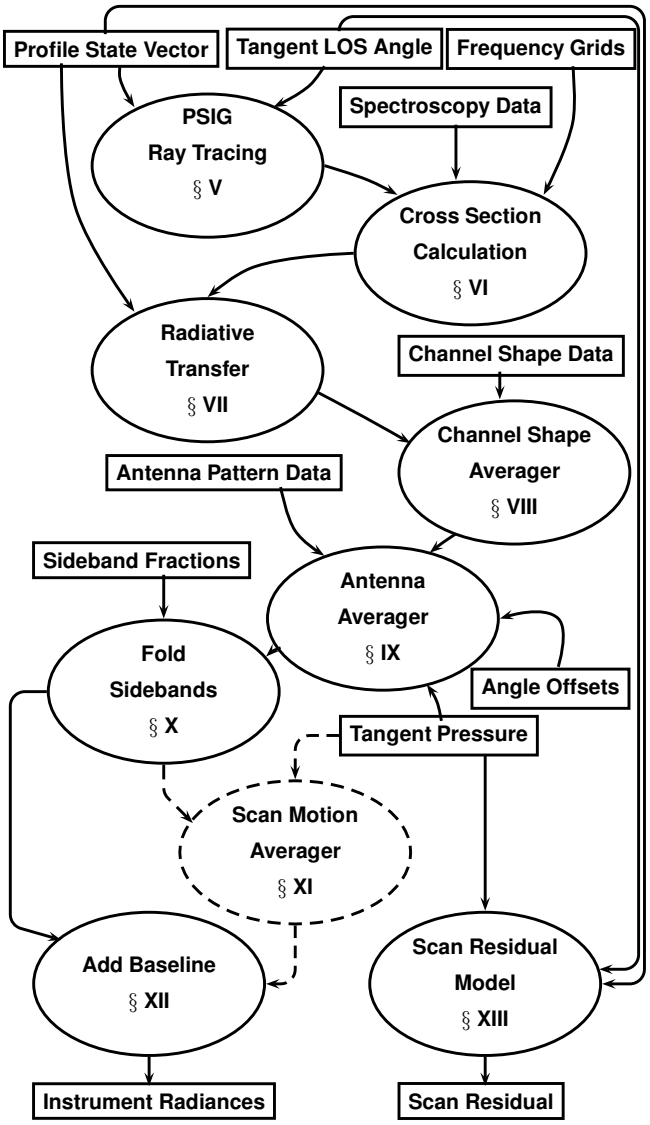

Fig. 3. Forward model calculation organization.

included to emphasize that a relative response function is needed. In practice these are "constants" that are folded into $\Phi_{\mathrm{R,c}}(\nu)$ and $G(\Omega,\Omega_t(t),\nu)$. The antenna gain normalizing integral is the integrated gain within Ω_A (~ 0.4 sterad) which is slightly less than 4π. Finally, quantities can be sideband, radiometer, and band/channel dependent. These are designated with subscripts, s = u or l, for sideband, R = R1A, R1B, R2, R3, R4, R5H, or R5V for radiometer, and c for a band = 1–34, channel = 1–129 combination. For some quantities, c would also include a switch network configuration [9].

The sideband fractions, $r_{\mathrm{u,R,c}}$ and $r_{\mathrm{l,R,c}}$ include the loss of limb signal through the antenna system as a consequence

of scattering, spill-over, and absorption. The sideband fractions $r_{\mathrm{u,R,c}}$ and $r_{\mathrm{l,R,c}}$ are defined as

$$\begin{aligned}
r_{\mathrm{u,R,c}} &= \eta^{A}_{\mathrm{u,R,c}} \rho^{A}_{\mathrm{R}} r'_{\mathrm{u,R,c}}, \\
r_{\mathrm{l,R,c}} &= \eta^{A}_{\mathrm{l,R,c}} \rho^{A}_{\mathrm{R}} r'_{\mathrm{l,R,c}}, \\
r'_{\mathrm{u,R,c}} &= \frac{\eta^{A}_{\mathrm{u,R,c}} r''_{\mathrm{u,R,c}}}{\eta^{A}_{\mathrm{u,R,c}} r''_{\mathrm{u,R,c}} + \eta^{A}_{\mathrm{l,R,c}} r''_{\mathrm{u,R,c}}}, \\
r'_{l,\mathrm{R,c}} &= \frac{\eta^{A}_{\mathrm{l,R,c}} r''_{l,\mathrm{R,c}}}{\eta^{A}_{\mathrm{u,R,c}} r''_{\mathrm{u,R,c}} + \eta^{A}_{\mathrm{l,R,c}} r''_{\mathrm{l,R,c}}}, \\
r''_{\mathrm{u,R,c}} &= \frac{\int_{\nu_{\mathrm{lo,R}}}^{\infty} \Phi_{\mathrm{R,c}}(\nu)\, \mathrm{d}\nu}{\int_{-\infty}^{\infty} \Phi_{\mathrm{R,c}}(\nu)\, \mathrm{d}\nu}, \\
r''_{\mathrm{l,R,c}} &= \frac{\int_{-\infty}^{\nu_{\mathrm{lo,R}}} \Phi_{\mathrm{R,c}}(\nu)\, \mathrm{d}\nu}{\int_{-\infty}^{\infty} \Phi_{\mathrm{R,c}}(\nu)\, \mathrm{d}\nu},
\end{aligned} \tag{2}$$

where $\eta^{A}_{\mathrm{l,R,c}}$ and $\eta^{A}_{\mathrm{u,R,c}}$ are the antenna efficiencies for the lower and upper frequency sidebands of R and c, and ρ^{A}_{R} (same for both sidebands) is the product of the ohmic losses of each reflector in the antenna system for R. The spectral function, $\Phi_{\mathrm{R,c}}$, has two peaked responses equidistant above and below the local oscillator frequency. The 118 GHz radiometer is an exception in that $\Phi_{\mathrm{R,c}}$ has a response only in the lower sideband. The radiometric sideband fractions $r''_{\mathrm{u,R,c}}$ and $r''_{\mathrm{l,R,c}}$ quantitatively describe the receiver's relative effectiveness at the sideband frequency. Conservation of power dictates, $r''_{\mathrm{u,R,c}} + r''_{\mathrm{l,R,c}} = 1$, but losses in the reflector system cause $r_{\mathrm{u,R,c}} + r_{\mathrm{l,R,c}} \leq 1$.

The terahertz module scan mirror is also used for viewing calibration sources. Consequently, there is no extra primary system antenna emission [11]; therefore $r_{\mathrm{u,R,c}} = r''_{\mathrm{u,R,c}}$, $r_{\mathrm{l,R,c}} = r''_{\mathrm{l,R,c}}$, and $I_{\mathrm{bl}} = 0$.

B. Aura Orbital Data

The Aura flight ephemeris provide detailed information on its location, attitude and velocity. EOS MLS provides encoder data, which is the angular position of its FOV direction. Using a straightforward geometric model [3], the longitude, latitude, and height of the EOS MLS FOV direction tangent height is estimated. The atmosphere is assumed to be in hydrostatic balance. Hydrostatic balance couples temperature, pressure, and altitude such that knowledge of any two is sufficient. The computed tangent locations from Aura flight operations and EOS MLS FOV encoder readings are used in a scan residual model to help measure temperature and limb tangent pressure and LOS angle.

C. State Vector

The state vector $\mathbf{x}$ consists of all the independent variables used in the forward model for which the level 2 processing requires radiance or scan residual model sensitivies. The state vector is composed of two parts, $\mathbf{x} = [\vec{x}_t, \mathbf{f}]$. The first part $\vec{x}_t$ consist of quantities that follow the measurement sequence, for example the FOV limb tangent height, global location both contained in $\Omega_t(t)$, and $\mathrm{BL}_{\mathrm{R},t}$ in (1). The subscript t means tangent and also indicates that these quantities are determined by the measurement characteristics of EOS MLS and the arrow $\rightarrow$ indicates that these are vectors with more than one element. These quantities behave irregularly, that is follow no specific patterns.

The second part, called the profile state vector, **f** has its values specified at certain heights, horizontal locations, and frequencies. Temperature and molecular composition are examples of profile state vector components. The profile state vector function is developed in Section IV.

The current (v1.5) Level 2 processing [4] state vector consists of limb tangent pressure, limb tangent LOS angle, an additive baseline, all irregular quantities, profiles for several molecular constituents and temperature, the latter being regular quantities. A more complete listing of the state vector is given in [3]. Although, the state vector except baseline is contained within $I(\nu,\mathbf{x}(\Omega))$ in (1), computationally it is more convenient to introduce parts of it at different computational steps as shown in Fig. 3. For example, the ray tracing calculation (PSIG Ray Tracing, Section V in Fig. 3) uses temperature coefficients and the tangent LOS to compute the two dimensional height-pressure-temperature state. Additionally, this module also needs the atmospheric composition and profile basis information to set up the appropriate ensemble of tangent pressures that are different than actual state vector tangent pressures for computing the radiance profile function that will later be used by the antenna averager module. When the antenna averager (or in a future version, the scan averager) does the vertical smoothing of the radiance profile it interpolates the result to the pressures in the state vector. The details and approximations of these calculations will be developed in later sections of the paper.

IV. Profile Representation

The EOS MLS forward model is a representation-basis driven algorithm, where components of **f** in the state vector **x** are represented by a weighted sum of basis functions. The constituent profile values are the weights. The weights and their associated basis functions are fully embedded throughout all parts of the calculation. Normally, the retrieved product requirements establish the basis parameters such as the vertical profile resolution and the same would be used in both the forward model and retrieval. The advantage offered by this approach is that the interface between retrieval and forward model is direct and simplified, that is there is no need for transformations between a lower resolution retrieval profile to a higher resolution forward model profile. Radiance sensitivities or derivatives are computed only for retrieved profile coefficients, again avoiding a down-sampling transformation between the forward model and retrieval, which saves computational time. Finally, the exact functional definition of the profile is preserved throughout the entire calculation.

A. Independent Coordinates

A fundamental issue is the choice of *independent* coordinates for gridding the state vector. The choice made here is based on Upper Atmosphere Research Satellite (UARS) MLS heritage and data output requirements. The state vector components can vary vertically, horizontally (along LOS), and spectrally (or EOS MLS channel). The vertical coordinate is, $\zeta = -\log(P)$ where P is pressure in hPa. Throughout this document, $\log = \log_{10}$ and $\ln = \log_e$. The LOS measurement track angle, ϕ, is the horizontal coordinate. Frequency, ν, is the spectral coordinate. All except the ϕ coordinate are self-explanatory. Referring to Fig. 2, ϕ refers to the horizontal locations, the colored arrows, of the profiles. Although the figure shows this as a horizontal distance, we have chosen to use a geodetic angular

coordinate because it is a periodic coordinate that more closely follows the elliptical shape of the Earth. Thus ϕ is the geodetic angle of a point on a suborbital ellipse defined by the EOS MLS Aura orbit. For EOS MLS we have chosen to place profiles every 1.5° and phased such that one profile is located at $n360°$, n = 0, 1, 2, ..., for a total of 240 profiles per orbit. For each day ϕ is an accumulated quantity being reset at the start of each day. The profile located at 0° is presumed to be crossing the equator on the ascending node. Therefore at the start of each processing day, the location of the first profile will have a negative value of ϕ that is close to the first limb tangent LOS scan angles such that when the first occurance of the ascending node crosses the equator, a profile is located at $\phi = 0°$ and all previous and subsequent profiles are properly aligned and phased. Therefore, ϕ modulo 360° has the following meaning: $0° \leq \phi < 90°$, northern hemisphere ascending node, $90° \leq \phi < 180°$, northern hemisphere descending node, $180° \leq \phi < 270°$, southern hemisphere descending node, and $270° \leq \phi < 360°$, southern hemisphere ascending node. The integer part of $\phi/360°$ gives the orbit number, which is of no concern here.

B. Profile Function

The EOS MLS forward model employs either linear or logarithmic representation basis functions. The linear representation is best for constituents where the radiance signal responds nearly linearly over the full range of concentration values. It is best for weak signal molecules because it allows for multiple profile averaging without introducing non-linear distortion in the averaged result and is used for the majority of state vector components represented with profiles. The logarithmic basis is best for molecules that have concentrations spanning decades of change and accompanied with a strongly non-linear radiance response. An example is tropospheric water vapor, which due to thermodynamic constraints of the Clausius-Clapeyron phase equilibrium equation naturally follows an exponential concentration gradient with temperature, and extinction, because it represents a molecular continuum, is proportional to P^2.

All linear state vector quantities are of the form:

$$\mathsf{f}^k(\zeta,\phi,\nu) = \sum_{l}^{\mathrm{NH}^k} \sum_{m}^{\mathrm{NP}^k} \sum_{n}^{\mathrm{NF}^k} f^k_{lmn} \eta^k_l(\zeta)\, \eta^k_m(\phi)\, \eta^k_n(\nu)\,, \tag{3}$$

and for the logarithmic basis are

$$\mathsf{f}^k(\zeta,\phi,\nu) = \exp\left[\sum_{l}^{\mathrm{NH}^k} \sum_{m}^{\mathrm{NP}^k} \sum_{n}^{\mathrm{NF}^k} \ln f^k_{lmn} \eta^k_l(\zeta)\, \eta^k_m(\phi)\, \eta^k_n(\nu) \right], \tag{4}$$

where $\mathsf{f}^k(\zeta,\phi,\nu)$ is a *profile* that can have height, horizontal, and spectral variability. f^k is a state vector *component* function identified by superscript k. f^k_{lmn} is an *element* of state vector component k. k covers everything to be differentiated by the forward model e.g., $k =$ "temperature", "ozone", or "radiometer sideband" are allowable choices. The η are basis functions in each of the three coordinates l,m,n for component k. NH, NP, and NF are the total number of basis functions in each of the three allowable dimensions. Any or all of these can be unity, which allows components to be scalars, up to three dimensions. The EOS MLS representation basis are triangular

functions given by

$$\eta_l^k(\zeta) = \begin{array}{ll} 0 & \zeta \geq \zeta_{l+1}^k \\ \frac{\zeta_{l+1}^k - \zeta}{\Delta\zeta_l^k} & \zeta_{l+1}^k > \zeta \geq \zeta_l^k \\ \frac{\zeta - \zeta_{l-1}^k}{\Delta\zeta_{l-1}^k} & \zeta_l^k > \zeta > \zeta_{l-1}^k \\ 0 & \zeta_{l-1}^k \geq \zeta \end{array}, \tag{5}$$

where $1 < l < \mathrm{NH}^k$, ζ_l^k is a grid-point height for the kth component, and $\Delta\zeta_l^k = \zeta_{l+1}^k - \zeta_l^k$. The special case, $l = 1$ is

$$\eta_1^k(\zeta) = \begin{array}{ll} 0 & \zeta \geq \zeta_2^k \\ \frac{\zeta_2^k - \zeta}{\Delta\zeta_1^k} & \zeta_2^k > \zeta \geq \zeta_1^k \\ 1 & \zeta_1^k > \zeta \end{array}, \tag{6}$$

and $l = \mathrm{NH}^k$ is

$$\eta_{\mathrm{NH}}^k(\zeta) = \begin{array}{ll} 1 & \zeta \geq \zeta_{\mathrm{NH}}^k \\ \frac{\zeta - \zeta_{\mathrm{NH}-1}^k}{\Delta\zeta_{\mathrm{NH}-1}^k} & \zeta_{\mathrm{NH}}^k > \zeta > \zeta_{\mathrm{NH}-1}^k \\ 0 & \zeta_{\mathrm{NH}-1}^k \geq \zeta \end{array}. \tag{7}$$

When combined with (3) or (4), the profile looks like linear or exponential segments where the coefficients define the breakpoint values. The profile is constant, having the value of the first and last coefficient below and above the first and last breakpoint ζ value. The special case where NH^k = 1 uses

$$\eta_1^k(\zeta) = 1. \tag{8}$$

Identical forms are used for $\eta_m^k(\phi)$ and $\eta_n^k(\nu)$. Fig. 4 gives an example of horizontal and vertical bases functions.

The regular state vector $\mathbf{f}$ usually consists of several components. All profile coefficients for a given component in all dimensions are designated as $\mathbf{f}^k$, where k indicates the specific component. The continuous representation of all profiles in all dimensions is designated as f. The continuous representation for temperature is $T = \mathsf{f}^T$.

V. Ray Tracing

A. Earth Figure

The EOS MLS forward model requires tangent pressure and tangent LOS angle. Fig. 5 shows these quantities (except here tangent height is shown) in the LOS frame (LOSF). The LOS ray s in Fig. 5 is one limb ray shown in Fig. 2. The Earth figure is defined to be an ellipse of constant geopotential ($U_o = 62.636860850$ km^2/sec^2) having major and minor axes lengths of 6378.137 and 6356.7523141 km, respectively (1980 Geodetic Reference System [12]). The ellipse shown is the projection of the Earth figure ellipse onto a plane formed by the center of the Earth figure ellipse and the LOS ray. The LOSF ellipse function is given by

$$1 = \frac{x^2}{a^2} + \frac{y^2}{c^2} \tag{9}$$

where x and y are Cartesian coordinates in the LOSF and c is the LOSF minor axis given by

$$c^2 = \frac{a^2 b^2}{a^2 \sin^2\beta + b^2 \cos^2\beta} \tag{10}$$

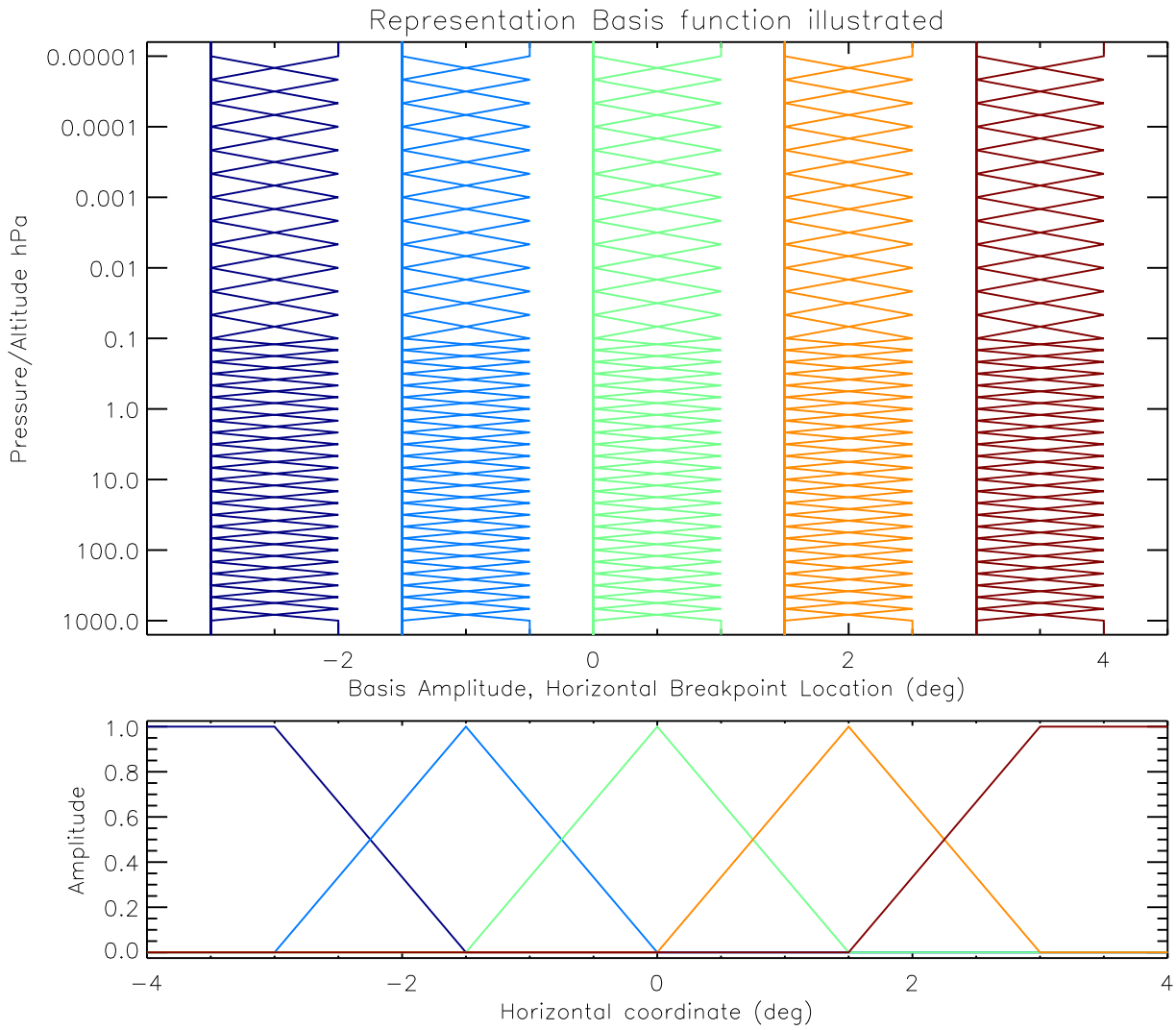

Fig. 4. Bases functions shown for a state vector component having 37 vertical (ζ_l^k) and 5 horizontal (ϕ_m^k) coefficient breakpoints. The top panel shows the 37 vertical bases functions for each of its 5 horizontal coefficients. The bottom panel shows the 5 horizontal bases functions.

where a and b are the Earth figure ellipse major and minor axes, and β is an incline angle between the plane formed by the center of Earth, satellite, and limb tangent position and the Earth centered rotating frame z-axis inclination angle. For EOS MLS it is well approximated by the orbital inclination angle (98.14 degrees nominal). This gives $c = 6357.1789319$ km for the projected ellipse.

The tangent point along the LOS is defined as the point where a line perpendicular to the LOS line is normal to the LOSF Earth figure ellipse and is characterized by the geodetic height h_t and angle ϕ_t, where subscript t indicates tangent. The EOS MLS forward model requires tangent pressure (when combined with temperature and

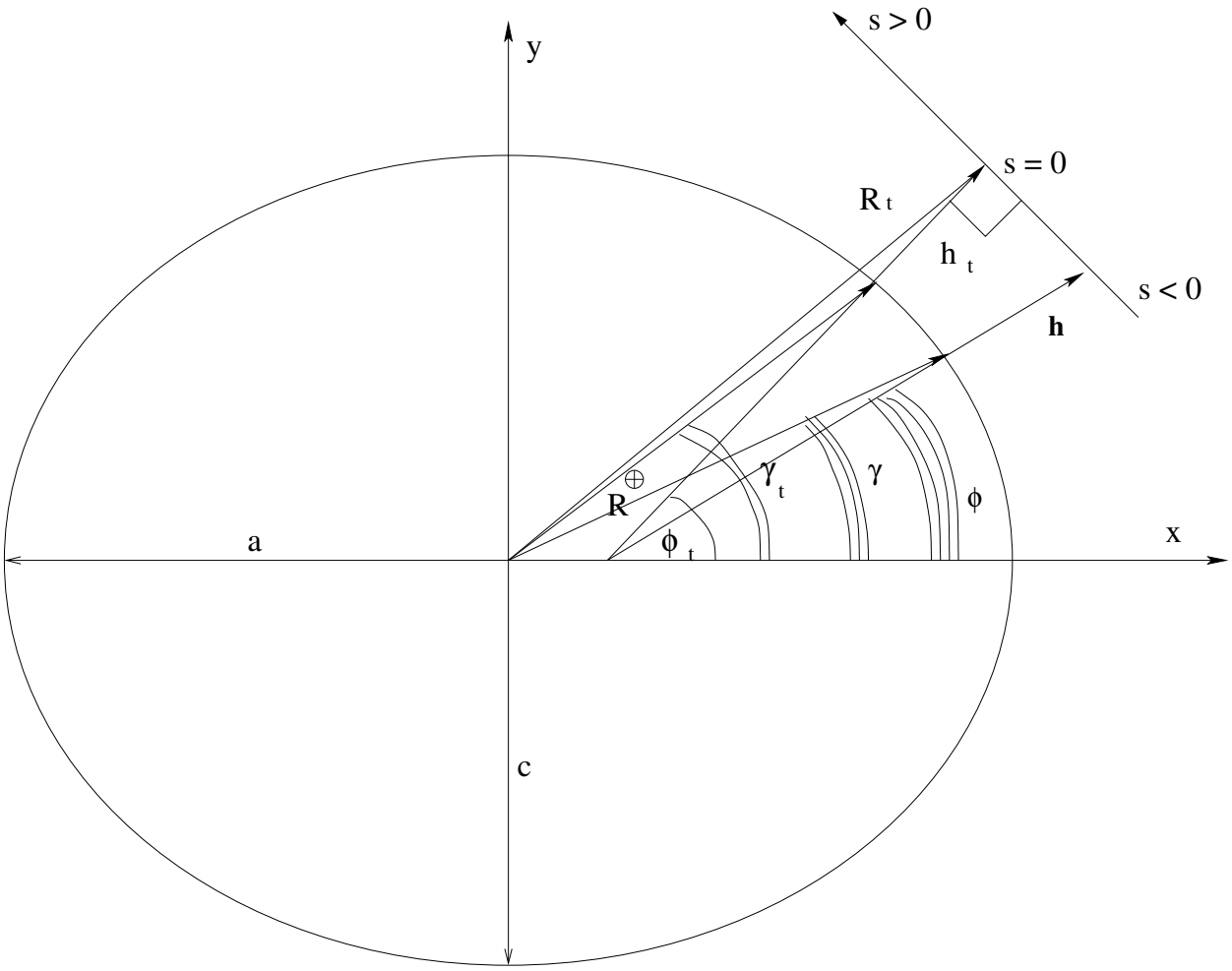

Fig. 5. Variables illustrated in relation to the Earth figure ellipse projected onto the x-y plane of the Line of Sight Frame (LOSF). The z axis points out of the page.

surface pressure gives the tangent height) and tangent LOSF angle as inputs. Therefore the LOS ray $\vec{R}$ is given by

$$\vec{R} = \vec{R}_t + \vec{n}_d s, \tag{11}$$

where $\vec{n}_d$ is a unit vector perpendicular to the limb tangent or tangent to the ellipse at ϕ_t, which is

$$\vec{n}_d = (-\sin\phi_t, \cos\phi_t, 0)\,. \tag{12}$$

The ray described in (11) neglects refraction; the handling of refraction is discussed later.

B. PreSelected Integration Grid (PSIG)

Solving the radiative transfer equation requires integrating the atmospheric state function along s, where the latter is chopped into many discrete steps to insure accurate results. Since the EOS MLS FOV scans the limb vertically as shown in Fig. 2, several radiance calculations at many tangent heights and tangent LOSF angles are

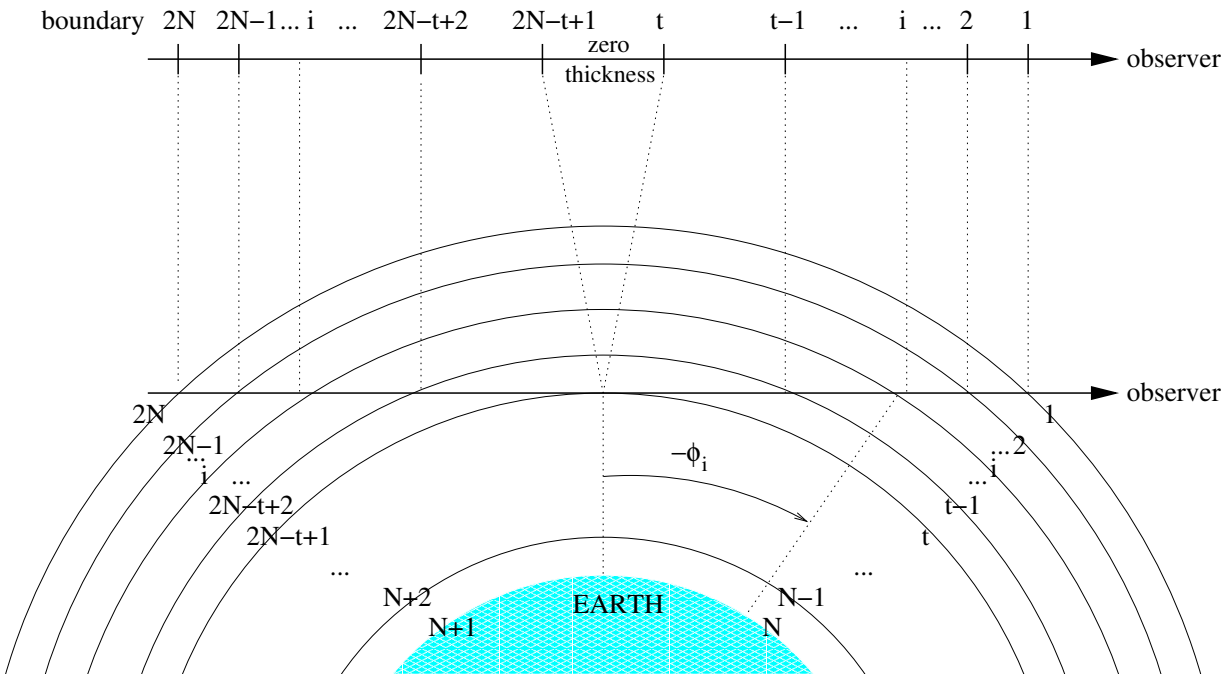

Fig. 6. Level indexing notation for discrete radiative transfer calculations. Note that each line of sight path is associated with a tangent pressure, t, and a pressure/angle index, i. The atmospheric state including height can be different along an isobar curve (e.g. $t \rightarrow 2N-t+1$).

required. s is subdivided according to the vertical representation bases of the inputted state vector. The preselected integration grid is formed from a sorted vector of all the unique ζ_l^k making up the profile state vector. The PSIG also establishes the tangent pressures for each s to be computed. A PSIG constructed this way is a minimum grid for making computations and does not necessarily provide sufficiently accurate results, especially where the radiance or profile gradients are large. Therefore, the EOS MLS forward model allows for oversampling this minimum PSIG. We achieve acceptable accuracy when we add extra ζs half-way between the minimum PSIG ζs for ζs less than -1.3333. The resulting PSIG is the minimum PSIG oversampled by 2 over a portion of its vertical range. Two times oversampling doubles the number of grid points and tangent heights to compute, therefore oversampling has a quadratic impact upon computational speed. The PSIG defines the atmospheric layering for the radiative transfer calculation as shown in Fig. 6. The integration quadrature requires additional points other than the basis ζ_l^k breakpoints (or multiples thereof) to produce accurate results. Therefore the PSIG is augmented with extra ζs. The integration uses a three point Gauss-Legendre (GL) quadrature described later (three additional ζs for each ζ in the PSIG). The GL method specifies the ζ values that are augmented to the PSIG. We do not compute additional tangent rays for these points; therefore, increasing the GL order leads to a linear decrease in computational speed.

Subsurface rays are inputted as negative tangent heights relative to the reference geopotential (Approximate sea level of Earth). Subsurface heights are supplied explicitly; there are no automatic selections for these rays.

C. Hydrostatic Model

Evaluating the atmospheric state along s requires ζ and ϕ ($\vec{R}$ in (11)) and so far, the augmented PSIG only supplies ζ. The LOS angle ϕ can be computed from heights using geometry. A set of basis heights, that is heights of the augmented PSIG evaluated at each temperature profile ϕ_m^{T} location, is computed using hydrostatic balance.

The heights of pressures are given by

$$\begin{aligned} h\left(\zeta,\phi_m^{\mathrm{T}}\right) &= \frac{g_o \overset{\star}{R}_o^{\,2}}{g_o \overset{\star}{R}_o - \mathsf{k}\ln 10 \sum_l^{\mathrm{NH^T}} \sum_m^{\mathrm{NP}^T} \left(f_{lm}^T \eta_m^T\left(\phi_m^{\mathrm{T}}\right) P_l\right)} \\ &- \overset{\star}{R}_o + R_o - R^{\oplus}, \end{aligned} \tag{13}$$

where k, is the Boltzmann constant, P_l is the integral

$$P_l = \int_{\zeta_o}^{\zeta} \frac{\eta_l^T(\zeta)}{\mathcal{M}(\zeta)} \mathrm{d}\zeta, \tag{14}$$

ζ_o is a reference pressure where the height, R_o, with respect to the center of the Earth is known and $\mathcal{M}$ is the mean molecular mass of the atmosphere. It is preferred that ζ_o is the hydrostatically equivalent pressure of a surface defined by U_o at the Earth figure ellipse. The gravitational acceleration is given by

$$g_o = -\mid \vec{\nabla} U_r\left(R_o,\phi_m^{\mathrm{T}}\right) \mid, \tag{15}$$

where $U_r\left(R_o,\phi_m^{\mathrm{T}}\right)$ is the geopotential function evaluated at R_o and the equivalent latitude and longitude represented by ϕ_m^{T}. The geopotential used here is

$$U_r = \frac{GM}{R}\left(1 - \sum_{i=1}^{2} J_{2i} P_{2i}(\lambda)\left(\frac{a}{R}\right)^{2i}\right) + \frac{\omega^2 R^2 \cos^2\lambda}{2}, \tag{16}$$

where R is the distance from the center of the Earth, J_{2i} are form factors, P_{2i} are Legendre polynomials, GM is the Gravitational constant times the mass of the Earth, ω is the angular velocity of the Earth and λ is the latitude of ϕ_m^{T} (conversion is straightforward see [3]). These constants are [12]:

$$\begin{aligned} J_2 &= 0.0010826256, \\ J_4 &= -0.0000023709122, \\ GM &= 3986005 \times 10^8 \mathrm{m^3 s^{-2}}, \\ \omega &= 7292115 \times 10^{-11} \mathrm{rad\ s^{-1}}, \\ P_2 &= \tfrac{1}{2}\left(3\sin^2\lambda - 1\right), \\ P_4 &= \tfrac{1}{8}\left(35\sin^4\lambda - 30\sin^2\lambda + 3\right). \end{aligned}$$

Expansion of (16) to J_4 is adequate for our purposes. To account for centrifugal effects, (13) is derived assuming a $1/R^2$ gravitational fall-off satisfying two boundary conditions: the gravitational acceleration and the vertical gravitational gradient at the reference height [13]. Equation (15) defines the former and the latter is satisfied by defining an "effective" height $\overset{\star}{R}_o$ according to

$$\overset{\star}{R}_o = \frac{2 g_o}{-\left(\partial g/\partial R\right)_{R=R_o}}. \tag{17}$$

The reference height R_o is the geometric height of the reference geopotential height. We use R_o to compute the surface pressure, then the reference height R_o is reset to the surface of the Earth reference ellipsoid $R^{\oplus}$, which is convenient because it serves as a boundary condition of the radiative transfer for reflected rays. ζ_o in (14) is set to the computed surface pressure.

The radiance temperature derivatives need the hydrostatic temperature derivative of (13) which is given by

$$\frac{\mathrm{d}h}{\mathrm{d}f_{lm}^T} = \frac{g_o \mathsf{k} \ln 10 \overset{\star}{R}_o^2 \eta_m^T\left(\phi_m^{\mathrm{T}}\right) P_l}{\left[g_o \overset{\star}{R}_o - \mathsf{k} \ln 10 \sum_l^{\mathrm{NT^T}} \sum_m^{\mathrm{NP^T}} \left(f_{lm}^T \eta_m^T\left(\phi_m^{\mathrm{T}}\right) P_l\right)\right]^2}. \tag{18}$$

D. Two Dimensional Atmospheric State

The LOS ray ϕs are calculated for the augmented PSIG. The measurement tangent pressures and tangent LOS angles are supplied. Using linear interpolation, a set of tangent PSIG LOS angles are estimated. For each PSIG tangent ϕ_t, the heights of the augmented PSIG ζs are estimated by linear interpolation of the two height profiles in $h\left(\zeta, \phi_m^{\mathrm{T}}\right)$ having ϕ_m^{T} adjacent to ϕ_t. Next we compute the ray $\vec{R}$ from these heights. Unfortunately it is not possible to express ϕ as a function of h (although the reverse is possible) in elliptical coordinates without iteration. Therefore an equivalent circular Earth approximation is invoked as shown in Fig. 7. Here, the LOSF projected Earth figure ellipse is approximated by a circle whose radius matches the curvature of the ellipse at ϕ_t given by

$$H_t^{\oplus} = N\left(\phi_t\right) \sqrt{\sin^2 \phi_t + \frac{c^4}{a^4} \cos^2 \phi_t}. \tag{19}$$

where $N(\phi) = a^2 / \sqrt{a^2 \cos^2 \phi + c^2 \sin^2 \phi}$. Note that h_t if extended indefinitely below the Earth surface passes through the center of the equivalent circle. The distance from the LOSF Earth ellipse is

$$\begin{aligned} x &= \left(N\left(\phi_t\right) - H_t^{\oplus}\right) \cos \phi_t, \\ y &= \left(\frac{c^2}{a^2} N\left(\phi_t\right) - H_t^{\oplus}\right) \sin \phi_t, \\ \vec{d} &= [x, y, 0]. \end{aligned} \tag{20}$$

Now the ray ϕ is easily evaluated according to

$$\phi = \phi_t \pm \arccos\left[\frac{\left(h_t + H_t^{\oplus}\right)}{\left(h + H_t^{\oplus}\right)}\right]. \tag{21}$$

The choice of the sign depends on which side of the tangent h is. The incoming Earth intersecting ray is computed according to

$$\phi = \phi_t + \arccos\left[\frac{H_t^{\oplus} \cos\left(\phi_{\mathrm{surf}} - \phi_t\right)}{h + H_t^{\oplus}}\right], \tag{22}$$

and the outgoing ray is

$$\phi = \phi_t - 2\phi_{\mathrm{surf}} - \arccos\left[\frac{H_t^{\oplus} \cos(\phi_{\mathrm{surf}} - \phi_t)}{h + H_t^{\oplus}}\right], \tag{23}$$

where $\phi_{\mathrm{surf}} = \phi_t - \arccos\left[\left(h_t + H_t^{\oplus}\right) / H_t^{\oplus}\right]$ and $h_t < 0$. The resulting ray ϕ does not account for horizontal gradients in temperature. To do so a new set of ray hs are computed from the ray ϕs using linear interpolation of $h\left(\zeta, \phi_m^{\mathrm{T}}\right)$. Using (21), or (22) and (23) a new set of ray ϕ is computed. This process is repeated until the ray h change

from the previous iteration is less than 10m. A limitation in the technique is its implied requirement that the minimum path ζ occurs where the path geodetic height is minimum. This is only true for the 1-D case or 2-D cases where the temperature gradient at the tangent is zero. In the general case, the minimum path ζ is slightly off the geodetic tangent. If the 2-D temperature gradient is large enough, it can cause convergence problems for the method outlined above. At present we do not have a capability for handling a variably adjusting ζ PSIG, therefore when non convergence occurs, linear interpolation is used to estimate the heights of pressures between ζ_t and its nearest converged ζ/h pair. Fig. 8 shows an example of ζ and LOS ϕ computed for an atmosphere with a large horizontal temperature gradient.

The final ray ϕs are now used to evaluate the atmospheric state using (3) or (4). The temperature derivative of the hydrostatic function is evaluated along the ray ϕs using linear interpolation of (18).

Fig. 9 shows the error introduced by using the equivalent circle approximation to the Earth figure ellipse shown in Fig. 5 and Fig. 7. There is no error at the tangent point and it slowly accumulates as one moves away from it. The path length s ($= H_t \tan(\phi)$), is accurate to 0.1% or better, and h better than 100 m. For the first three degrees of ϕ about ϕ_t, which covers 5 coefficients, h is accurate to 10 m and the s difference is negligible. At the orbital poles and equator, the errors are 10 times smaller. From the figure, it shows that the path length error at $s = \pm 500$ km about ϕ_t is 0.01%. Assuming a radiance weighting function 1000 km wide and optically thin situations, would lead to a radiance error of $\sim$0.01% or 0.01 K at 100 K. The error for optically thick situations should be smaller because the path length sensitivity is attenuated by the transmission function. Therefore, the equivalent circle representation for ray-tracing is an excellent approximation.

The state vector component, LOS tangent ϕ_t must include refraction. The Aura ephemeris provides unrefracted LOS angle ϕ_t^{geom} based on spacecraft location, attitude and EOS MLS FOV direction encoder data. The ϕ_t^{geom} is adjusted for refraction according to [3]

$$\begin{aligned} \phi_t \equiv \phi_t^{\text{refr}} &= \phi_t^{\text{geom}} + \int_{\text{MAX}(H_t, H^{\oplus})}^{H_s} \frac{\mathcal{N}_t H_t \, \mathrm{d}H}{H} \\ &\times \left(\frac{1}{\sqrt{\mathcal{N}^2 H^2 - \mathcal{N}_t^2 H_t^2}} \right. \\ &- \left. \frac{1}{\sqrt{\mathcal{N}_t^2 H^2 - \mathcal{N}_t^2 H_t^2}} \right), \end{aligned} \tag{24}$$

where $H = h + H_t^{\oplus}$, $H_t = h_t + H_t^{\oplus}$, H_s is the spacecraft height (or any height where refraction is negligible), and $\mathcal{N}$ is the refractive index of air. The refractive index of air is

$$\mathcal{N} = 1 + \frac{0.0000776}{T(\zeta,\phi)\, 10^{\zeta}} \left(1 + 4810 \frac{\mathrm{f}^{\text{H2O}}(\zeta,\phi)}{T(\zeta,\phi)} \right). \tag{25}$$

Fig. 10 shows the difference between unrefracted and refracted ϕ_t for two orbits of simulated February data showing the variability of this difference. At pressures less than 100 hPa, the difference is small, being 0.07° or 5% of the EOS MLS horizontal grid spacing. The difference grows to 0.18 ° or 20% at 500 hPa however the variability is not extreme. At pressures greater than 500 hPa, the difference and its variability are very large. Since EOS MLS

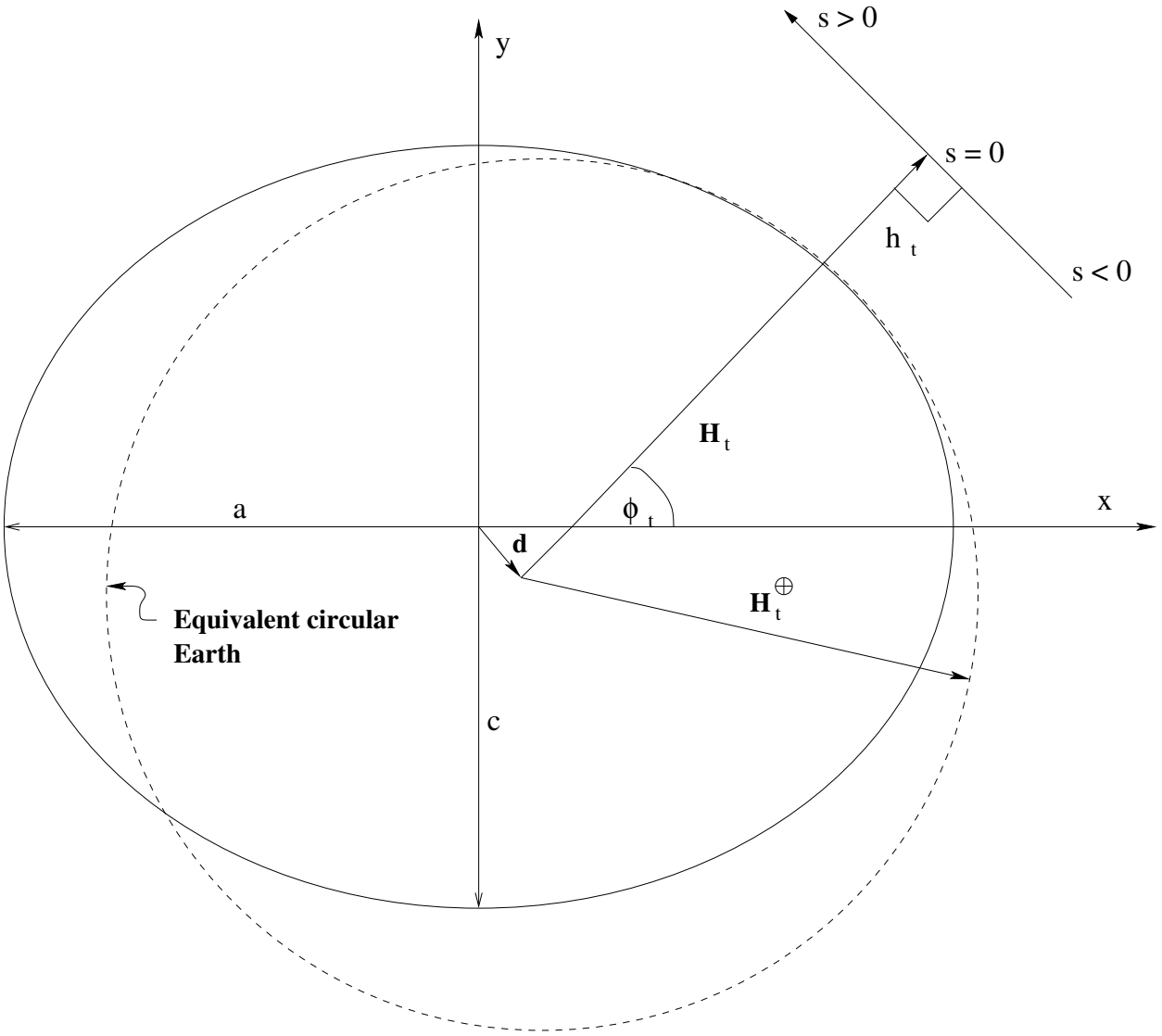

Fig. 7. The equivalent circular Earth representation in the LOSF.

profile measurements do not extend to pressures higher than 500 hPa one can use a table generated from this figure to do the correction. Unfortunately an oversight in the v1.5 EOS MLS software development did not make this adjustment and we currently use ϕ_t^{geom} in the forward model. Also related is that the ϕs generated for the 2-D rays should also be corrected for refraction. The correction is calculated from (24) with the upper integration limit changed from H_s to the PSIG H for the ϕ being corrected. Currently this correction is also neglected.

TABLE I

MOLECULES CONSIDERED IN EOS MLS FORWARD MODEL

^{79}BrO	$^{79}BrO(\nu_1)$	^{81}BrO	$^{81}BrO(\nu_1)$	CH_3CN	CH_3COCH_3	CH_3Cl	$CH_3^{35}Cl$	$CH_3^{37}Cl$	CH_3OH	CO	^{13}CO
$C^{17}O$	$C^{18}O$	$OC^{18}O$	^{35}ClO	$^{35}ClO(\nu_1)$	^{37}ClO	$^{37}ClO(\nu_1)$	COF_2	$^{35}ClOO^{35}Cl$	$^{35}ClOO^{37}Cl$	$^{35}ClONO_2$	$^{37}ClONO_2$
$H^{79}Br$	$H^{81}Br$	$H^{35}Cl$	$H^{37}Cl$	$D^{35}Cl$	$D^{37}Cl$	HCN	$HCN(\nu_2)$	$H^{13}CN$	$HC^{15}N$	$HCOOH$	HF
DF	H_2CO	$H_2^{13}CO$	$H_2C^{18}O$	H_2O	$H_2O(\nu_2)$	$H_2^{17}O$	$H_2^{17}O(\nu_2)$	$H_2^{18}O$	$H_2^{18}O(\nu_2)$	D_2O	HDO
$HDO(\nu_2)$	$HD^{17}O$	$HD^{18}O$	H_2O_2	$H_2^{32}S$	$H_2^{32}SO_4$	HNO_3	$HNO_3(\nu_5)$	$HNO_3(\nu_6)$	$HNO_3(\nu_7)$	$HNO_3(\nu_8)$	$HNO_3(\nu_9)$
$H^{15}NO_3$	$HO^{79}Br$	$HO^{81}Br$	$HO^{35}Cl$	$HO^{37}Cl$	HO_2	$HOONO_2$	N_2	N_2O	$N_2O(\nu_1)$	$N_2O(\nu_2)$	$N_2O(2\nu_2)$
^{15}NNO	$N^{15}NO$	$N_2^{17}O$	$N_2^{18}O$	NO	NO_2	O	^{17}O	^{18}O	$O^{35}ClO$	$O^{37}ClO$	$OC^{32}S$
$OC^{34}S$	$O^{13}C^{32}S$	OH	^{18}OH	OD	O_2	$O_2(\nu_1)$	$O^{17}O$	$O^{18}O$	$O^{18}O(\nu_1)$	$^1\Delta_g O_2$	$^1\Delta_g^{18}OO$
O_3	$O_3(\nu_{1,3})$	$O_3(\nu_2)$	$O_3(2\nu_2)$	$O_3(\nu_{1,3}+\nu_2)$	$O_2^{17}O$	$O^{17}OO$	$O_2^{18}O$	$O_2^{18}O(\nu_2)$	$O^{18}OO$	$O^{18}OO(\nu_2)$	$^{32}SO_2$
$^{32}SO_2(\nu_2)$	$^{33}SO_2$	$^{34}SO_2$									

VI. SPECTROSCOPY

A. Molecules Considered

The EOS MLS bands have considerable spectral coverage (see Fig. 1) and are affected by signals from additional molecules that are not part of the targeted suite. Therefore a first task is to identify all lines and molecules that may contribute measurable signals. Table I lists all the molecules including vibrational states and isotopes that have been considered. The isotope mass number is dropped for atoms whose most abundant isotope exceeds 95%. With the exception of $H^{15}NO_3$ these molecules exist in the JPL Spectroscopy Catalog [14] or the HITRAN database [15]. $H^{15}NO_3$ is expected to be added to the JPL Spectroscopy Catalog soon.

B. The EOS MLS Molecule Catalog

The EOS MLS molecule catalog consists of two parts, molecule data and line data for computing the line-by-line absorption. Table II gives an example of molecule data. The molecule data table gives spectroscopic data that are common to molecular lines selected for the EOS MLS radiometer band. The molecular data table includes the isotopic abundance, mass, partition function values, and line shape continuum parameters. Tables III and IV give an example of line data, which consist of spectroscopic data that is line specific. This includes line position, line strength, lower state energy, pressure broadening parameter and temperature dependence, pressure shift parameter and temperature dependence, four intramolecular line interference parameters [16], a modified JPL Spectroscopy Catalog quantum number format, the upper state quantum numbers, the lower state quantum numbers, the EOS MLS bands the line is applied to, and the data source of the broadening parameters. The complete tables are published in [3].

The data in the EOS MLS spectroscopy catalog are derived from many sources. The line positions, strengths, lower state energies, and quantum numbers are from the JPL Spectroscopy Catalog when available, otherwise the

HITRAN values are used. The quantum number format is slightly modified from the JPL catalog to include the number of combined lines. Whenever there are multiple lines having the same line position and lower state energy, these degenerate lines are combined to form a single line that is the sum of the strengths and tabulated in the catalog. The quantum number format reflects this by adding the number of merged lines times 10000 added to the JPL Spectroscopy Catalog quantum number format. The quantum numbers for the merged line are those for one of the merged lines. Laboratory measurements of shape parameters including shifts and interferences are separately maintained in files. The lines in these files are identified by their quantum numbers. It is believed that a quantum number tag is a more robust identifier than the line position frequency, which may change in future revisions of the JPL Spectroscopy catalog. If a laboratory measurement is not available in our files, then the HITRAN database value is used. If it is not available from HITRAN then an educated guess is used. The column in Table IV labeled "LS ref" shows the heritage of the lineshape data having "M" for laboratory measured, "H" for HITRAN, or "G" for guess. The column labeled "EOS Bands" indicate which bands this line should be used for. This is an efficiency step that limits the number of line-by-line computations in the forward model. The isotopic abundances are based on crustal values of the elements except for ^{18}OO which is based on atmospheric measurements [17]. The mass is the sum of the atomic masses composing the molecule which are available from any modern periodic chart. The partition functions are the total partition function including rotation, vibration and electronic energy levels. Most of the partition functions come from the HITRAN catalog because it includes the vibrational and rotational partition functions. The JPL Spectroscopy Catalog partition functions usually only include the rotational component, which can cause significant errors. When the JPL Spectroscopy Catalog includes the vibrational and/or electronic component, then we preferentially use it. There are some cases where the JPL partition function is larger than the HITRAN value even though HITRAN includes the vibrational contribution. This is caused by a maximum state truncation error (did not include enough rotational states) in the HITRAN partition function calculation. In these cases, an adjusted JPL partition function is used, where it is multiplied by an estimate of the vibrational contribution. Whenever the partition function differs from that in its respective database, the strength has been multiplied by the ratio of the old (usually JPL Spectroscopy Catalog) partition function to the new partition function. It is well known that the line-by-line calculation does not capture all the line absorption observed. Therefore to account for the excess absorption, we have allowed storage for 6 continuum parameters. The continuum parameters can be global or EOS MLS radiometer specific. In the case of radiometer specific, using H_2O as an example, a few lines are used in the line-by-line calculation as indicated by the "EOS Bands" column and the remaining absorption from the neglected H_2O lines have a simple continuum-like parameterization given by a molecule designated as H_2O-r2 for EOS MLS radiometer R2. The continuum under the main molecule heading e.g., H_2O, N_2, and O_2 apply to all radiometers.

C. Molecule and Line Selection

Molecules and lines are selected based on their likely signal strength. First molecules that are likely to have both line and continuum contributions are selected. This list is N_2, O_2, H_2O, and O_3. The lines selected are tested with

TABLE II

EXAMPLES OF MOLECULE DATA

molecule, k	isotopic abundance $\mathcal{R}^k$	mass $\mathcal{M}^k$ AMU	Partition Function Q^K at 300 K	225 K	150 K	cont_1^k ($\mathrm{km^{-1}hPa^{-2}MHz^{-2}}$)	cont_2^k	cont_3^k ($\mathrm{MHz^{-2}}$)	cont_4^k ($\mathrm{km^{-1}hPa^{-1}MHz^{-4}}$)	cont_5^k ($\mathrm{MHz^{-2}}$)	cont_6^k MHz
H_2O	0.99729	18.011	178.115	116.011	63.680	5.376×10^{-16}	4.80	0.000	0.000	0.000	0.000
H_2O-r2	0.99729	18.011	0.0000	0.0000	0.0000	2.446×10^{-16}	3.495	0.000	0.000	0.000	0.000
N_2	0.99269	28.006	0.000	0.000	0.000	5.727×10^{-20}	3.964	1.669×10^{-12}	9.997×10^{-33}	1.113×10^{-13}	1.798×10^{6}
O_2	0.99519	31.990	218.6754	164.1345	109.5973	6.87×10^{-9}	2.8	0.56	0.8	0.000	0.000
O_3	0.99279	47.984	3563.3512	2235.0190	1200.4721	0.000	0.0	0.000	0.000	0.000	0.000
…	…	…	…	…	…	…	…	…	…	…	…

TABLE III

EXAMPLES OF LINE DATA PART I

molecule	ν^k_{0j} (MHz)	I^k_j(300 K) ($\mathrm{nm^2MHz}$)	$E\ell^k_j$ ($\mathrm{cm^{-1}}$)	w^k_{cj}(300 K) (MHz $\mathrm{hPa^{-1}}$)	n^k_{cj}	$\Delta\nu^k_{0j}$(300 K) (MHz $\mathrm{hPa^{-1}}$)	$n^k_{\Delta\nu_{0j}}$	δ^k_j(300 K) ($\mathrm{hPa^{-1}}$)	$n^k_{\delta_j}$	γ^k_j(300 K) ($\mathrm{hPa^{-1}}$)	$n^k_{\gamma_j}$
H_2O	22235.0800	446.5107	-5.8875	2.658	0.640	0.000	0.000	0.00e+00	0.00	0.00e+00	0.00
	183310.1170	136.1639	-3.6465	2.830	0.750	-0.060	1.375	0.00e+00	0.00	0.00e+00	0.00
	…	…	…	…	…	…	…	…	…	…	…
O_2	…	…	…	…	…	…	…	…	…	…	…
	118750.3430	0.0000	-6.5312	1.528	0.979	0.000	0.000	-3.60e-05	0.80	9.00e-06	1.80
	…	…	…	…	…	…	…	…	…	…	…

TABLE IV

EXAMPLES OF LINE DATA PART II

molecule	ν^k_{0j} (MHz)	QN fmt	QNu	QNl	EOS Bands	LS ref
H_2O	22235.0800	1404	6 1 6 0	5 2 3 0		H
	183310.1170	1404	3 1 3 0	2 2 0 0	B2L, B3L, B4L, B5L, B6L, B23L, B27L B2U, B3U, B4U, B5U, B6U, B23U, B27U	M
	…	…	…	…	…	…
O_2	…	…	…	…	…	…
	118750.3430	102	1 1	1 0	B1L, B21L, B22L, B26L, B32L, B34L	M
	…	…	…	…	…	…

this simple optically thin radiance estimate

$$\begin{aligned} I &= \mathsf{f}^k \beta^k s, \\ s &\approx 2\sqrt{2H_t \Delta h}, \end{aligned} \tag{26}$$

where β^k is the molecule cross section (given later) at the line center frequency and f^k is a representative volume mixing ratio for molecule k. The path length s = 500 km is approximately a Δh =5 km thick vertical layer. For these molecules we keep any line where $I > 1$ K between 0–3 THz. N_2 has no lines but has a significant continuum. Within each radiometer frequency coverage range (both sidebands) a full line-by-line absorption calculation is performed for each of these molecules (except N_2). Then a subset of lines in the vicinity of the radiometer is selected and another line-by-line calculation is performed. A continuum function of the form $\text{cont\_1}\, p^2 \left(300/T\right)^{\text{cont\_2}} \nu^2$ where cont_1 and cont_2 is fitted to the difference between the full and partial line-by-line absorption calculation. When the fitted continuum function models the frequency, pressure, and temperature dependence of the excess absorption between the full and partial absorption within 10%, then the lines in the partial calculation are designated for all the bands in the radiometer (indicated in "EOS Bands") and an extra radiometer-specific continuum for the molecule is added to the molecular table (e.g. H_2O-r1a, H_2O-r1b, H_2O-r2, H_2O-r3, H_2O-r4, H_2O-r5h, H_2O-r5v, O_3-r1a, O_3-r1b, O_3-r2, O_3-r3, O_3-r4, O_3-r5h, O_3-r5v).

Individual EOS MLS bands or groups of bands when they overlap or are spectrally close are scanned for lines for all the molecules listed in Table I. For each molecule in Table I, all lines that fall within the extreme frequency coverage of the scanned band(s) plus/minus the edge channel width are tested with (26) against a threshold value. Lines with signal strengths greater than the threshold are added to the EOS MLS catalog and their respective "EOS Bands" is identified. The thresholds are: R1A, R1B, 1 K, R2, 0.05 K, R3, 1 K, R4, 0.05 K, and R5H, R5V, 0.5 K. The different thresholds are based on the strengths of the targeted lines and processing speed limitations.

D. Calculating Cross Sections

The cross-section β^k for the kth species is given by

$$\beta^k = \beta^k_{\text{LxL}} + \beta^k_{\text{cont}} \tag{27}$$

where β^k_{LxL} is the line-by-line contribution and β^k_{cont} is any excess contribution that is not accounted for in the line-by-line calculation typically referred as continuum. The line-by-line cross section is [18]

$$\begin{aligned} \beta^k_{\text{LxL}} &= \mathcal{R}^k \sqrt{\frac{\ln 2}{\pi}} \frac{10^{-13}}{\mathsf{k} T w_d^k} P \tanh\left\{\mathsf{h}\nu/\left(2\mathsf{k}T\right)\right\} \\ &\times \sum_j 10^{s_j^k} \text{LineShape}\left(x_j^k(\nu), y_j^k(\nu), z_j^k(\nu)\right) \end{aligned} \tag{28}$$

where

$$\begin{aligned} \mathcal{S}_j^k &= I_j^k(300) + \frac{\mathsf{hc}E\ell_j^k}{\mathsf{k}}\left(\frac{1}{300} - \frac{1}{T}\right) + \log\left[\frac{Q^k(300)}{Q^k(T)}\right] \\ &+ \log\left[\frac{\left(1+\exp\left\{-\mathsf{h}\nu_j^k/\left(\mathsf{k}T\right)\right\}\right)}{\left(1-\exp\left\{-\mathsf{h}\nu_{0j}^k/\left(\mathsf{k}300\right)\right\}\right)}\right], \end{aligned} \tag{29}$$

T is temperature in Kelvins, P is pressure in hPa, $\mathcal{R}^k$ is the isotopic fraction for the species, $I_j^k(300)$ is the logarithm of the integrated intensity in nm^{2}MHz at 300 K, ν is frequency in MHz, ν_j^k is the pressure shifted line center frequency in MHz, ν_{0j}^k is the zero pressure line center frequency in MHz, $E\ell_j^k$ is the ground state energy in cm^{-1}, $Q^k(T)$ is the partition function, $w_d^k = \sqrt{2\ln 2k}\nu\sqrt{\frac{T}{\mathcal{M}^k}}/\mathsf{c}$ is the Doppler width in MHz, $\mathcal{M}^k$ is the absorber molecular mass in amu, c is the speed of light, $\sqrt{\frac{\ln 2}{\pi}}\frac{10^{-13}}{\mathsf{k}}$ = 3.402136078 $\times 10^9$ K hPa^{-1}nm^{-2}km^{-1}, is proportional to the reciprocal Boltzmann constant, k in JK^{-1}, LineShape$\left(x_j^k(\nu), y_j^k(\nu), z_j^k(\nu)\right)$ is the lineshape function and j identifies the individual lines in the molecule. The constants, $\sqrt{2\ln 2k}/\mathsf{c} = 3.58117369 \times 10^{-7}$ AMU$^{\frac{1}{2}}$T$^{-\frac{1}{2}}$, $\mathsf{k}/\mathsf{hc} = 1.600386$ cm^{-1}K^{-1}, $\mathsf{k}/\mathsf{h} = 20836.74$ MHz K^{-1}. The temperature dependence of the logarithm of the ratio of the partition function at 300K to T is approximated by

$$\log\left[\frac{Q^k(300)}{Q^k(T)}\right] = \log\left[\frac{Q^k(300)}{Q^k(T_0)}\right] + \frac{\log\left[\frac{Q^k(T_1)}{Q^k(T_0)}\right]}{\log\left[\frac{T_1}{T_0}\right]}\log\left[\frac{T_0}{T}\right], \tag{30}$$

where $Q^k(T_1)$ and $Q^k(T_0)$ are tabulated partition functions at temperatures T_1 and T_0, which are, preferably, greater than and less than T (or vice-versa), respectively, and $Q^k(300)$ is the partition function evaluated at 300K. The partition function includes all the rotational, vibrational, and electronic states. The partition function for EOS MLS calculations is tabulated at 300, 225, and 150K.

The LineShape function is

$$\begin{aligned}
&\text{LineShape}\left(x_j^k(\nu), y_j^k(\nu), z_j^k(\nu)\right) = \\
&\left(\frac{\nu}{\nu_{0j}^k}\right)\left\{\frac{1}{\pi}\int_{-\infty}^{\infty}\frac{\left[y_j^k(\nu) - Y_j^k\left(x_j^k(\nu)-t\right)\right]\exp\left(-t^2\right)}{\left(y_j^k(\nu)\right)^2 + \left(x_j^k(\nu)-t\right)^2}\mathrm{d}t\right. \\
&+ \left.\frac{1}{\sqrt{\pi}}\frac{y_j^k(\nu) - Y_j^k z_j^k(\nu)}{\left(z_j^k(\nu)\right)^2 + \left(y_j^k(\nu)\right)^2}\right\},
\end{aligned} \tag{31}$$

where $x_j^k(\nu) = \frac{\sqrt{\ln 2}\left(\nu-\nu_j'^k\right)}{w_d^k}$, $y_j^k(\nu) = \frac{\sqrt{\ln 2}w_{cj}^k P}{w_d^k}\left(\frac{300}{T}\right)^{n_{cj}^k}$, $z_j^k(\nu) = \frac{\sqrt{\ln 2}\left(\nu+\nu_j'^k\right)}{w_d^k}$, w_{cj}^k is the collision width in MHz hPa^{-1}, n_{cj}^k is its temperature dependence, and Y_j^k is an intramolecular line interference coefficient. All temperature dependent quantities such as strengths, widths, shifts and interferences are for 300 K. The $\left(\frac{\nu}{\nu_{0j}^k}\right)$ term, which is virtually constant over a Doppler width, has been pulled outside the integral. The integral is related to the Fadeeva function (eq. 7.1.4 in [19]). The numerator of the integrand with $y_j^k(\nu)$ is a Voigt function (real part of the Fadeeva function). The numerator of the integrand with Y_j^k is the imaginary part of the Fadeeva function. The Fadeeva function is evaluated according to [20]. The line center frequency is pressure shifted and Doppler shifted according to

$$\begin{aligned}
\nu_j^k &= \left[\nu_{0j}^k + \Delta\nu_{0j}^k P\left(\frac{300}{T}\right)^{n_{\Delta\nu_{0j}^k}}\right], \\
\nu_j'^k &= \nu_j^k\left(1 + \frac{\mathrm{d}s}{\mathrm{d}t}/\mathsf{c}\right)
\end{aligned} \tag{32}$$

where $n_{\Delta\nu_{0j}^k}$ is the temperature dependence of ν_j^k and $\frac{ds}{dt}$ is the projection of the spacecraft orbital velocity along ray s in Fig. 5 or Fig. 7. $\Delta\nu_{0j}^k$ is the pressure shift parameter in MHz hPa^{-1}. The temperature dependence of the shift is often not known for the few cases where the shift is measured. In those cases we use $n_{\Delta\nu_{0j}^k} = \left(1+6n_{cj}^k\right)/4$ based on a theory developed by [21]. The interference coefficient is parameterized according to

$$Y_j^k = P\left[\delta_j^k\left(\frac{300}{T}\right)^{n_{\delta j}^k} + \gamma_j^k\left(\frac{300}{T}\right)^{n_{\gamma j}^k}\right]; \tag{33}$$

at this time it is only known for some O_2 lines [16] and is zero for all other molecules.

Some molecules have continuum contributions. Except for EXTINCTION, N_2, and O_2 (defined later), the continuum parametrization is given by

$$\beta_{\text{cont}}^k = \mathcal{R}^k \text{cont\_1}^k \nu^2 P^2 (300/T)^{\text{cont\_2}^k}, \tag{34}$$

where cont_x (x=1–6) is a continuum parameter. Eq. 34 is the continuum due to collisions in dry air, therefore in the case of H_2O, the self-absorption (which has different parameters and scales by $\left(f^{H_2O}\right)^2$) is ignored. The continuum parameters for H_2O-r2 and H_2O-r3 are from total absorption measurements by [A.Meshkev and F. DeLucia, personal communication, 2004]. The continuum parameterization of H_2O-r5v and H_2O-r5h are from laboratory measurements by [H. Pickett, personal communication, 2004]. We have created an entity called EXTINCTION, which is present for retrieving an additive baseline in molecular absorption units. It can act as a proxy for atmospheric absorption from unknown molecules or certain types of clouds (that emit without scattering radiation). The cross section function for EXTINCTION is

$$\beta^{\text{EXTINCTION}} = \text{cont\_1}^{\text{EXTINCTION}}, \tag{35}$$

Where $\text{cont\_1}^{\text{EXTINCTION}} = 1$ (unitless). The retrievable $\mathbf{f}^{\text{EXTINCTION}}$ has units of km^{-1}. The N_2 cross section is parameterized according to [22]

$$\begin{aligned}\beta^{N_2} &= P^2\nu^2(300/T)^{\text{cont\_2}^{N_2}} \\ &\times \left[\text{cont\_1}^{N_2}\exp\left\{-\text{cont\_3}^{N_2}\nu^2\left(\frac{300}{T}\right)\right\}\right. \\ &+ \text{cont\_4}^{N_2}\exp\left\{-\text{cont\_5}^{N_2}\nu^2\left(\frac{300}{T}\right)\right\} \\ &\times \left.\left(\left\{\text{cont\_6}^{N_2}\right\}^2+\nu^2\right)\right].\end{aligned} \tag{36}$$

Eq. 36 is an empirical function that fits the N_2 Collision Induced Absorption (CIA) spectrum from 0–3 THz. The N_2 absorption coefficient is $\left(f^{N_2}\right)^2\beta^{N_2}$ where $f^{N_2} = 0.79$. Pardo [23] has found that in the atmosphere, dry absorption due to N_2–N_2, N_2–O_2, O_2–N_2, and O_2–O_2 pairs can be adequately fitted by multiplying eq. 36 by 0.81 = (1.29×0.79^2). The continuum parameters in Table II are from total absorption measurements of air by [A. Meshkev and F. DeLucia, personal communication, 2004]. The continuum parameterization for O_2 is the Debye spectrum according to [16]

$$\beta_{\text{cont}}^{O_2} = \mathcal{R}^{O_2}\frac{\text{cont\_1}^{O_2}\nu^2P^2(300/T)^{\text{cont\_2}^{O_2}}}{\nu^2+\left(\text{cont\_3}^{O_2}P(300/T)^{\text{cont\_4}^{O_2}}\right)^2}. \tag{37}$$

The Debye continuum absorption coefficient is $f^{O_2}\beta_{\text{cont}}^{O_2}$. Equation (37) must be added to the line-by-line contribution for O_2 to yield the total cross section for O_2.

The isotopic fraction $\mathcal{R}^k$ allows the user to input a volume mixing ratio for the total molecule yet have the computed cross sections scaled appropriately. The software implements a feature that allows the user to combine a number of molecules and treat the combination as one. The feature allows one to combine the most abundant isotope with its excited vibrational states, and less abundant isotopic components of the same molecule. The combined β^k is simply a sum over the individual β^k's of the combined species, times their isotopic fractions $\mathcal{R}^k$. The software can also be run where the isotopic fraction is ignored, that is, $\mathcal{R}^k = 1$. The two options are necessary because for some molecules (e.g. H_2O), the isotopic fractions in the upper atmosphere differ significantly from that found at the Earth's surface [24].

The forward model also computes derivatives of the cross section with respect to temperature, line position, line broadening, and line broadening temperature dependence. These derivatives are straightforward to derive; however, the resulting equations are long and complicated, and they are available in [3].

VII. Radiative Transfer

The radiative transfer model described here is for the special case of a clear sky atmosphere in local thermodynamic equilibrium emitting unpolarized radiation. The main emphasis is the rapid yet accurate calculation of derivatives that are needed by the inversion algorithm (Level 2).

A. Discrete Radiative Transfer Solution

The radiative transfer equation in local thermodynamic equilibrium through the atmosphere is

$$\frac{\mathrm{d}I(\nu,\mathbf{x}(s))}{\mathrm{d}s} + \kappa(\nu,\mathbf{x}(s))\,I(\nu,\mathbf{x}(s)) = \kappa(\nu,\mathbf{x}(s))\,B(\nu,\mathbf{x}(s)) \tag{38}$$

where $\kappa(\nu,\mathbf{x}(s)) = \sum_k f^k\beta^k$ is the atmospheric absorption coefficient and $B(\nu,\mathbf{x}(s))$ is the source function. Equation (38) is converted to an integral equation and solved discretely with numerical quadratures. The notation used to designate levels and ray paths is shown in Fig. 6. The atmosphere is partitioned into N concentric shells or levels. A ray path cuts through all the levels above the tangent level. The outermost level is 1 nearest the observer and each level is numbered consecutively to the tangent level t. The next level that initiates the ray on the atmospheric side opposite to the observer is $2N-t+1$ and the levels are then numbered consecutively until the ray leaves the last level now on the far side of the observer at $2N$. Levels t and $2N-t+1$ point to the exact same spot in the atmosphere bounding a "zero-thickness" layer. The level redundancy provides a simple algorithm for handling Earth reflections and emissions. This is accomplished by choosing an appropriate value for the tangent level emission efficiency value Υ (= 1, for non-Earth-intersecting rays and is < 1, the Earth reflectivity coefficient otherwise). The levels in Fig. 6 correspond to the PSIG ζ (without the extra quadrature points) described in section V. Section V also provides the algorithm for computing ϕ, temperature and other profile quantities at the layer boundaries.

The discrete radiative transfer equation is

$$I(\nu, \mathbf{x}(\Omega)) = \sum_{i=1}^{2N} \Delta B_i \mathcal{T}_i, \tag{39}$$

where ΔB_i is the differential temperature source function given by

$$\begin{aligned}
\Delta B_1 &= \frac{B_1 + B_2}{2}, \\
\Delta B_i &= \frac{B_{i+1} - B_{i-1}}{2}, \\
\Delta B_t &= \frac{B_{2N-t+1} - B_{t-1}}{2}, \\
\Delta B_{2N-t+1} &= \frac{B_{2N-t+2} - B_t}{2}, \\
\Delta B_{2N-i+1} &= \frac{B_{2N-i+2} - B_{2N-i}}{2}, \\
\Delta B_{2N} &= I_o - \frac{B_{2N-1} + B_{2N}}{2},
\end{aligned} \tag{40}$$

I_o is the background cosmic radiance incident on the top of the atmosphere, B is the thermal Planck radiation function,

$$B_i = B(\nu, \mathbf{x}(s_i)) = \frac{\mathsf{h}\nu}{\mathsf{k}\left[\exp\left(\frac{\mathsf{h}\nu}{\mathsf{k}T_i}\right) - 1\right]}, \tag{41}$$

h is the Planck constant, k is the Boltzmann constant, ν is the radiation frequency and T_i is temperature at the ith level. $\mathcal{T}_i$ is the transmission function at the ith level given by

$$\begin{aligned}
&\text{for } i \le t, \\
&\mathcal{T}_1 = 1, \\
&\mathcal{T}_i = \exp\left(-\sum_{j=2}^{i} \Delta\delta_{j \to j-1}\right), \\
&\text{for } t < i < 2N - t + 1, \\
&\mathcal{T}_i = 0, \\
&\text{for } i = 2N - t + 1, \\
&\mathcal{T}_{2N-t+1} = \Upsilon \mathcal{T}_t, \\
&\text{for } i > 2N - t + 1, \\
&\mathcal{T}_i = \mathcal{T}_{2N-t+1} \exp\left(-\sum_{j=2N-t+2}^{i} \Delta\delta_{j-1 \to j}\right),
\end{aligned} \tag{42}$$

where $\Delta\delta_{j \to j-1}$ is the incremental opacity between levels $j \to j-1$. The limits for the incremental opacity integral are reversed for $i > t$ to keep the lower limit closest to the tangent surface. In limb viewing, the atmosphere is usually not transmissive enough to see the surface. Therefore we assume $\Upsilon = 0.05$ with the reflection boundary occurring at the reference geopotential. Variations in Υ and surface topography are not considered.

There is sometimes confusion regarding how the differential temperature radiative transfer (39) works in the vicinity of the tangent, which we clarify now. Expanding (39) and showing only the terms about $i = t$ gives

$$\begin{aligned} I(\nu, \mathbf{x}(\Omega)) = \cdots + \Delta B_{t-1}\mathcal{T}_{t-1} + \Delta B_t \mathcal{T}_t + \Delta B_{2N-t+1}\mathcal{T}_{2N-t+1} \\ + \Delta B_{2N-t+2}\mathcal{T}_{2N-t+2} + \cdots \\ = \cdots + \frac{B_t - B_{t-2}}{2}\mathcal{T}_{t-1} + \frac{B_{2N-t+1} - B_{t-1}}{2}\mathcal{T}_t \\ + \frac{B_{2N-t+2} - B_t}{2}\mathcal{T}_{2N-t+1} + \frac{B_{2N-t+3} - B_{2N-t+1}}{2}\mathcal{T}_{2N-t+2} + \cdots . \end{aligned} \tag{43}$$

Recognize that index t and $2N-t+1$ are the same point on the LOS path, which requires $B_t = B_{2N-t+1}$ and from (42), $\mathcal{T}_{2N-t+1} = \Upsilon\mathcal{T}_t$. We also set $\mathcal{T}_{2N-t+2} = \Upsilon\mathcal{T}_t\Delta\mathcal{T}_{2N-t+1\to 2N-t+2}$ where $\Delta\mathcal{T}_{2N-t+1\to 2N-t+2} = \exp(-\Delta\delta_{t+1\to t+2})$. Adding and subtracting $\frac{B_t}{2}(1-\Upsilon)$ to (43) and collecting all the terms that involve B_t and B_{2N-t+1} gives

$$\begin{aligned} I(\nu, \mathbf{x}(\Omega)) = \cdots + \frac{B_t + B_{t-1}}{2}(\mathcal{T}_{t-1} - \mathcal{T}_t) + B_t(1-\Upsilon)\mathcal{T}_t \\ + \frac{B_{2N-t+2} + B_t}{2}\mathcal{T}_t\Upsilon(1 - \Delta\mathcal{T}_{2N-t+1\to 2N-t+2}) + \cdots . \end{aligned} \tag{44}$$

The terms as arranged in this equation show that the linear average temperature in the layer is multiplied by the difference in the transmission function between the layer boundaries (first and third terms). The solution is exact if temperature is linear in transmission. This result is consistent with the differential transmission form of the radiative transfer equation. The second term right of = contains the Earth reflectivity effect. If the LOS ray is above the Earth surface, then $\Upsilon = 1$ and the second term disappears. For Earth intersecting rays, $\Upsilon \neq 1$, the second term is the surface emission from the Earth attenuated by the atmospheric transmission, and the Earth intersecting part of the LOS (third term onward) is scaled by the surface reflectivity.

B. Discrete Radiative Transfer Derivative

The derivative form of (39) is

$$\frac{\mathrm{d}I(\nu, \mathbf{x}(\Omega))}{\mathrm{d}x_j} = \sum_{i=1}^{2N} Q_i \mathcal{T}_i, \tag{45}$$

where x_j is an element in state vector $(\mathbf{x})$. This is identical to (39) except Q_i replaces ΔB_i and is given by

$$Q_i = \frac{\partial \Delta B_i}{\partial x_j} - \Delta B_i \mathcal{W}_i, \tag{46}$$

where $\mathcal{W}_i$ is the transmittance derivative given by

$$\begin{aligned}
\mathcal{W}_1 &= 0, \\
\text{for } i &\leq t, \\
\mathcal{W}_i &= \mathcal{W}_{i-1} + \frac{\partial \Delta\delta_{i\rightarrow i-1}}{\partial x_j}, \\
\text{for } t &< i < 2N-t+1, \\
\mathcal{W}_i &= 0, \\
\mathcal{W}_{2N-t+1} &= \mathcal{W}_t, \\
\text{for } i &> 2N-t+1, \\
\mathcal{W}_i &= \mathcal{W}_{i-1} + \frac{\partial \Delta\delta_{i-1\rightarrow i}}{\partial x_j},
\end{aligned} \tag{47}$$

where $\frac{\partial \Delta\delta_{i\rightarrow i-1}}{\partial x_j}$ is the layer opacity derivative with respect to state vector element x_j.

C. Incremental Opacity Integral

The incremental opacity is given by

$$\Delta\delta_{i\rightarrow i-1} = \sum_{k=1}^{NS} \Delta\delta_{i\rightarrow i-1}^{k}, \tag{48}$$

which is a summation of each species contribution to the incremental opacity. The species incremental opacity integral is

$$\begin{aligned}
\Delta\delta_{i\rightarrow i-1}^{k} &= \frac{\Delta s_{i\rightarrow i-1}^{\text{refr}}}{\Delta s_{i\rightarrow i-1}} \int_{\zeta_i}^{\zeta_{i-1}} \mathsf{f}^k(\zeta,\phi(\zeta),\nu)\,\beta^k(P(\zeta),T(\zeta),\nu) \\
&\times \frac{(h(\zeta)+H^{\oplus}(\phi_t))}{\sqrt{(h(\zeta)+H^{\oplus}(\phi_t))^2-(h(\zeta_t)+H^{\oplus}(\phi_t))^2}} \\
&\times \frac{\left[h(\zeta)+\overset{\star}{R}_o(\phi(\zeta))-R_o(\phi(\zeta))+R^{\oplus}(\phi(\zeta))\right]^2}{g_o(\phi(\zeta))\,\overset{\star}{R}_o^{\,2}(\phi(\zeta))\,\mathcal{M}(\zeta)} \\
&\times T(\zeta)\,\mathsf{k}\ln 10\mathrm{d}\zeta,
\end{aligned} \tag{49}$$

where f^k is either from (3) or (4) and $\beta^k(P(\zeta),T(\zeta),\nu)=\beta^k$ is the cross section for the kth species. ζ is the LOS path coordinate; it establishes h and ϕ in addition to ζ as described in section V. The term following the first "$\times$" is $\frac{\mathrm{d}s}{\mathrm{d}h}$. The last two lines of (49) are $\frac{\mathrm{d}h}{\mathrm{d}\zeta}$. The last three lines chain-rule path length to the independent variable, ζ. The geometric model is based on the equivalent circular Earth and the hydrostatic model is based on a geocentric gravitational model and is the source of the many different R's involved. Refraction causes a path-lengthening effect relative to the straight-line path differences used here. This is compensated for by scaling the opacity integral by the ratio of the straight path length to the refracted one. Numerical experiments have shown this to be a completely satisfactory approximation (< 0.01 K). The path length ratio is given by

$$\frac{\Delta s_{i\rightarrow i-1}^{\text{refr}}}{\Delta s_{i\rightarrow i-1}} = \int_{\zeta_i}^{\zeta_{i-1}} \frac{\mathcal{N}H}{\sqrt{\mathcal{N}^2H^2-\mathcal{N}_t^2H_t^2}} \frac{\mathrm{d}h}{\mathrm{d}\zeta}\mathrm{d}\zeta \Big/ \int_{\zeta_i}^{\zeta_{i-1}} \frac{\mathrm{d}s}{\mathrm{d}h}\frac{\mathrm{d}h}{\mathrm{d}\zeta}\mathrm{d}\zeta, \tag{50}$$

where $\mathcal{N}$ is the refractive index given in (25). The derivation of (50) is given in [3]. The tangent point singularity in Equation (50) is handled by changing the integration variable, $x^2 = \mathcal{N}^2 H^2, 2x\mathrm{d}x = 2\left(\mathcal{N}^2 H + \mathcal{N} H^2 \frac{\mathrm{d}\mathcal{N}}{\mathrm{d}H}\right)$ and integrating with GL in x. This requires a root solver that gives H and $\mathcal{N}$ for each GL x. Another consideration is the effect of path lengthening on the ray traced ϕ. It is currently ignored but can be included by integrating (24). The state vector quantities such as temperature would be evaluated with the corrected ϕ. Note that ϕ_t is not affected and that the error (the horizontal component for evaluating state vector components) increases as the horizontal distance from the tangent increases. The magnitude of this error has not been quantified. In future software upgrades, we will add the horizontal correction according to (24).

These integrals are evaluated with a 3-point Gauss-Legendre quadrature based on pressure griding. The integrand in (49) has a singularity at the tangent point. A simple method for handling singularities is to recast (49) as

$$\int_{\zeta_i}^{\zeta_{i-1}} F(\zeta) \frac{\mathrm{d}s}{\mathrm{d}h}\frac{\mathrm{d}h}{\mathrm{d}\zeta}\mathrm{d}\zeta = F(\zeta_i)\int_{\zeta_i}^{\zeta_{i-1}} \frac{\mathrm{d}s}{\mathrm{d}h}\frac{\mathrm{d}h}{\mathrm{d}\zeta}\mathrm{d}\zeta + \int_{\zeta_i}^{\zeta_{i-1}} [F(\zeta) - F(\zeta_i)] \frac{\mathrm{d}s}{\mathrm{d}h}\frac{\mathrm{d}h}{\mathrm{d}\zeta}\mathrm{d}\zeta, \quad (51)$$

where $F(\zeta)$ contains a non-singular function. The first integral on the right of $=$ has a singularity but can be integrated analytically because it is the path length, $\Delta s_{i\rightarrow i-1}$. The second term right of $=$ still has a singularity but if the $F(\zeta) - F(\zeta_i)$ part is higher order than the path length derivative then a well-behaved solution results. In this case F is proportional to β, which is nearly exponential in ζ; the result is very well behaved and this trick provides a good solution. This method does not apply to (50) hence a different method is used to evaluate it. Having the vertical breakpoints of the representation basis functions coincide with the PSIG improves the accuracy of the derivative calculation by eliminating integrations across the breakpoints of the basis functions, where its first derivative is discontinuous.

The forward model calculation uses a semi-adaptive approach for computing (49). The first integral right of the = in (51) is evaluated at each PSIG point. This requires one absorption coefficient and a simple path length calculation (the analytical solution to the integral) per PSIG point. From this, an estimate of the radiative transfer error along the transmission path is calculated,

$$\Delta I(\nu, \mathbf{x}(\Omega)) = 250.0\,(\delta_{i+1} - \delta_{i-1})\,\mathcal{T}_i, \quad (52)$$

where $\delta_i = \sum_{j=2}^{i} \Delta\delta_{j\rightarrow j-1}$ or $\delta_i = \delta_t + \sum_{j=2N-t+2}^{i} \Delta\delta_{j-1\rightarrow j}$ and the 250 is a representative value for temperature. The indices in the PSIG where $\Delta I(\mathbf{x})$ exceeds a threshold value (usually 0.2K for the strong signals), the second term right of the = in (51) is computed with the 3-point GL quadrature. This saves 3 absorption coefficient evaluations and an integration for each PSIG point having a radiance contribution error smaller than the threshold.

D. Opacity and Source Function Derivatives

The radiative transfer derivative in (45) is a function of the opacity derivative and the differential temperature derivative (source function). For EOS MLS, this comes in three forms, mixing ratio, temperature, and β specific. These forms are given below

1) Mixing ratio: The derivative of the source function with respect to mixing ratio is zero so that term in (46) vanishes. The opacity derivative with respect to mixing ratio using the linear basis is

$$\begin{aligned}\frac{\mathrm{d}\Delta\delta^k_{i\to i-1}}{\mathrm{d}f^k_{lmn}} &= \frac{\Delta s^{\mathrm{refr}}_{i\to i-1}}{\Delta s_{i\to i-1}}\int_{\zeta_i}^{\zeta_{i-1}} \eta^k_l(\zeta)\,\eta^k_m(\phi(\zeta))\,\eta^k_n(\nu) \\ &\times \quad \beta^k(P(\zeta),T(\zeta),\nu)\,\frac{\mathrm{d}s}{\mathrm{d}h}\frac{\mathrm{d}h}{\mathrm{d}\zeta}\mathrm{d}\zeta. \end{aligned} \tag{53}$$

It is worth noting that summing these integrals times the mixing ratio coefficient f^k_{lmn} over all four indices also gives the incremental opacity in (48). The frequency dependence is retained because one of the species, EXTINCTION, allows for spectral structure.

The opacity derivative with respect to mixing ratio using the logarithmic basis is

$$\begin{aligned}\frac{\mathrm{d}\Delta\delta^k_{i\to i-1}}{\mathrm{d}f^k_{lmn}} &= \frac{\Delta s^{\mathrm{refr}}_{i\to i-1}}{\Delta s_{i\to i-1}}\int_{\zeta_i}^{\zeta_{i-1}} \frac{\eta^k_l(\zeta)\,\eta^k_m(\phi(\zeta))\,\eta^k_n(\nu)}{f^k_{lmn}} \\ &\times \quad \mathsf{f}^k(\zeta,\phi(\zeta),\nu)\,\beta^k(P(\zeta),T(\zeta),\nu)\,\frac{\mathrm{d}s}{\mathrm{d}h}\frac{\mathrm{d}h}{\mathrm{d}\zeta}\mathrm{d}\zeta. \end{aligned} \tag{54}$$

Note that $f^k_{lmn} > 0$ always; therefore this representation is not appropriate for weak and noisy products.

2) Temperature: The temperature derivative is quite complicated because it affects the cross section, hydrostatic model, and the path length. Some simplifying assumptions are made to make this problem simpler. The sensitivity of these equations to the change in refraction due to temperature is ignored and $\frac{\mathrm{d}h}{\mathrm{d}\zeta} = H^2\mathsf{k}T\ln 10/\left(g_o R_o^2 \mathcal{M}\right)$ is assumed where H is in the equivalent circular Earth system. The path length derivative, $\frac{\mathrm{d}s}{\mathrm{d}h} = H/\sqrt{H^2 - H_t^2}$. Since temperature is independent of frequency, $\eta_n(\nu) = 1$. The temperature derivative of the incremental opacity is

$$\begin{aligned}\frac{\mathrm{d}\Delta\delta^k_{i\to i-1}}{\mathrm{d}f^T_{lmn}} &\approx \frac{\Delta s^{\mathrm{refr}}_{i\to i-1}}{\Delta s_{i\to i-1}}\int_{\zeta_{i-1}}^{\zeta_i} \mathrm{d}\zeta \\ &\times \quad \left\{ \mathsf{f}^k(\zeta,\phi(\zeta),\nu)\,\frac{\mathrm{d}\beta^k(P(\zeta),T(\zeta),\nu)}{\mathrm{d}f^T_{lmn}}\,\frac{H^3}{\sqrt{H^2-H_t^2}}\,\frac{T\mathsf{k}\ln 10}{g_o R_o^2\mathcal{M}}\right. \\ &+ \quad \mathsf{f}^k(\zeta,\phi(\zeta),\nu)\,\beta^k(P(\zeta),T(\zeta),\nu) \\ &\times \quad \frac{T\mathsf{k}\ln 10}{g_o R_o^2\mathcal{M}}\,\frac{\mathrm{d}\left(H^3/\sqrt{H^2-H_t^2}\right)}{\mathrm{d}f^T_{lmn}} \\ &+ \quad \mathsf{f}^k(\zeta,\phi(\zeta),\nu)\,\beta^k(P(\zeta),T(\zeta),\nu) \\ &\times \quad \left.\frac{H^3}{\sqrt{H^2-H_t^2}}\,\frac{\mathrm{d}\left[T\mathsf{k}\ln 10/\left(g_o R_o^2\mathcal{M}\right)\right]}{\mathrm{d}f^T_{lmn}}\right\}. \end{aligned} \tag{55}$$

$\frac{\mathrm{d}\beta^k(P(\zeta),T(\zeta),\mathrm{v})}{\mathrm{d}f^T_{lmn}} = \frac{\mathrm{d}\beta^k(P(\zeta),T(\zeta),\mathrm{v})}{\mathrm{d}T}\eta^T_l(\zeta)\eta^T_m(\phi(\zeta))$ where $\frac{\mathrm{d}\beta^k(P(\zeta),T(\zeta),\mathrm{v})}{\mathrm{d}T}$ computed analytically from (28) is given in [3]. Equation (55) is rewritten as

$$\begin{aligned}\frac{\mathrm{d}\Delta\delta^k_{i\to i-1}}{\mathrm{d}f^T_{lmn}} \approx & \frac{\Delta s^{\mathrm{refr}}_{i\to i-1}}{\Delta s_{i\to i-1}}\int_{\zeta_i}^{\zeta_{i-1}}\mathrm{d}\zeta \\ \times & \left\{\mathrm{f}^k\frac{\mathrm{d}\beta^k}{\mathrm{d}T}\frac{\eta^T_l(\zeta)\eta^T_m(\phi(\zeta))}{T}\frac{\mathrm{d}s}{\mathrm{d}h}\frac{\mathrm{d}h}{\mathrm{d}\zeta}\right. \\ + & \mathrm{f}^k\beta^k\frac{2H^2\frac{\mathrm{d}H}{\mathrm{d}f^T_{lm}} - 3H_t^2\frac{\mathrm{d}H}{\mathrm{d}f^T_{lm}} + HH_t\frac{\mathrm{d}H_t}{\mathrm{d}f^T_{lm}}}{\left(H^2-H_t^2\right)^{\frac{3}{2}}}\frac{\mathrm{d}h}{\mathrm{d}\zeta} \\ + & \left.\mathrm{f}^k\beta^k\frac{\eta^T_l(\zeta)\eta^T_m(\phi(\zeta))}{T}\frac{\mathrm{d}s}{\mathrm{d}h}\frac{\mathrm{d}h}{\mathrm{d}\zeta}\right\}. \end{aligned} \tag{56}$$

The first term in (56) is the temperature sensitivity due to the cross section and the second two terms are the temperature sensitivity to changes in the radiative transfer geometry that are brought about by the hydrostatic relationship. Now it would seem quite natural to combine the first and third summed terms and integrate but there is a strategic reason for not doing this. These equations, like (49) have a singularity that can be taken out by performing the integration according to (51). When that approach is used on the last two summed terms right of the $=$, their integral becomes

$$\begin{aligned}\frac{\Delta s^{\mathrm{refr}}_{i\to i-1}}{\Delta s_{i\to i-1}}\mathrm{f}^k_i\beta^k_i\int_{\zeta_{i-1}}^{\zeta_i}\frac{\mathrm{d}\frac{\mathrm{d}s}{\mathrm{d}h}\frac{\mathrm{d}h}{\mathrm{d}\zeta}}{\mathrm{d}T_{lm}}\mathrm{d}\zeta = & \frac{\Delta s^{\mathrm{refr}}_{i\to i-1}}{\Delta s_{i\to i-1}}\mathrm{f}^k_i\beta^k_i \\ \times & \left(\frac{H_i\frac{\mathrm{d}H_i}{\mathrm{d}T_{lm}} - H_t\frac{\mathrm{d}H_t}{\mathrm{d}T_{lm}}}{\sqrt{H_i^2-H_t^2}} - \frac{H_{i-1}\frac{\mathrm{d}H_{i-1}}{\mathrm{d}T_{lm}} - H_t\frac{\mathrm{d}H_t}{\mathrm{d}T_{lm}}}{\sqrt{H_{i-1}^2-H_t^2}}\right), \end{aligned} \tag{57}$$

where H_i is added and subtracted to both sides of (56). When this is done, $\mathrm{f}^k_i\beta^k_i$ is subtracted from the integrand in the last two terms right of the $=$ in (56) and integrated. Do not use (57) then combine the first and third terms in a GL integration, which will give the wrong answer. The first term right of the $=$ is integrated like (49).

The source function derivative $\frac{\mathrm{d}\Delta B_i}{\mathrm{d}T_{lm}}$ for temperature is

$$\begin{aligned}\frac{\mathrm{d}\Delta B_i}{\mathrm{d}T_{lm}} &= \frac{\frac{\mathrm{d}B_{i+1}}{\mathrm{d}T_{lm}} - \frac{\mathrm{d}B_{i-1}}{\mathrm{d}T_{lm}}}{2}, \text{where,} \\ \frac{\mathrm{d}B_i}{\mathrm{d}T_{lm}} &= \frac{B_i^2\exp\left\{\frac{\mathrm{h}\nu}{\mathrm{k}T_i}\right\}}{T_i^2}\eta^T_l(\zeta_i)\eta^T_m(\phi(\zeta_i)). \end{aligned} \tag{58}$$

3) β specific derivatives: The β specific derivatives pertain to those state vector components (except temperature) that affect β. Specifically these include spectroscopic parameters such as the broadening parameter, its temperature dependence, and line position. Radiance sensitivities to β are given by

$$\frac{\mathrm{d}\Delta\delta^k_{i\to i-1}}{\mathrm{d}x_j} = \frac{\Delta s^{\mathrm{refr}}_{i\to i-1}}{\Delta s_{i\to i-1}}\int_{\zeta_i}^{\zeta_{i-1}}\mathrm{f}^k\frac{\mathrm{d}\beta^k}{\mathrm{d}x_j}\frac{\mathrm{d}s}{\mathrm{d}h}\frac{\mathrm{d}h}{\mathrm{d}\zeta}\mathrm{d}\zeta. \tag{59}$$

This is identical to the opacity integral ((49)) where β^k is replaced with $\frac{\mathrm{d}\beta^k}{\mathrm{d}x_j}$ and evaluated accordingly. When the singularity separation is done, the differential term, which now involves $\frac{\mathrm{d}\beta^k}{\mathrm{d}x_j}$ must go to zero faster than the singularity. Given that β behaves exponentially and satisfies the condition, the derivative will behave exponentially and should satisfy the condition also.

VIII. Spectral Integration

The EOS MLS instrument channels measure radiation over a finite bandwidth of frequencies. This causes the resulting signal to distort or spectrally smear the lineshape relative to a monochromatic measurement. The methodology for computing the spectral integral in (1) is described here.

A. Evaluation

The radiative transfer equation (section VII) is evaluated at several frequencies and convolved with the spectral response as given in (1). Since the radiative transfer calculations are time consuming there is an effort to minimize the number of its computations. This is done by computing a radiative transfer spectrum at selected frequencies across the radiometer bandpass. The frequencies are selected using a variable frequency step-size selecting algorithm such that the brightness temperature for any frequency can be accurately computed with interpolation. Each tangent pressure and radiometer band(s) has its own optimized spectral grid. "Frequency grids" in Fig. 3 consists of the spectral grids. The full band spectral computation was incorporated by Hugh Pumphrey [25] for the 183 GHz band in UARS MLS with very good results. Next we assume that the antenna gain function is invariant over the channel response and pull it outside the spectral averaging integral, thus replacing $G(\Omega,\Omega_t(t),\nu) = G_{\mathrm{s,R,c}}(\Omega,\Omega_t(t))$. The motivation for separating the antenna averaging integral from the spectral integral and computing the spectral integral first is to minimize the number of antenna averaging integrations. The frequency coordinate in the Frequency grids file differs for each LOS tangent height and for some heights there are more than an order of magnitude more frequency points than there are channels. Performing the antenna averaging before the spectral averaging would require us to establish a common frequency grid, a union of all the frequencies selected for all the LOS tangent heights, and perform an antenna smoothing integration for each frequency. Reversing the antenna and spectral integrations and separating the two as done here saves a lot of antenna averaging integrations without appreciable sacrifice in accuracy. The channel radiance for each height is

$$I_{\mathrm{u,R,c}}(\mathbf{x}(\Omega)) = \frac{\int_{\nu_{\mathrm{lo,R}}}^{\infty} I(\nu,\mathbf{x}(\Omega))\,\Phi_{\mathrm{R,c}}(\nu)\,\mathrm{d}\nu}{\int_{\nu_{\mathrm{lo,R}}}^{\infty} \Phi_{\mathrm{R,c}}(\nu)\,\mathrm{d}\nu} \tag{60}$$

There is an analogous equation for the lower side-band (see (1)). The filter shape data $\Phi_{\mathrm{R,c}}(\nu)$ is "Channel shape data" in Fig. 3. The response of each channel of each of the standard filter banks has been tabulated and they are integrated using a trapezoidal quadrature. The actual quadrature is not considered to be a critical issue since the frequency gridding of the radiative transfer calculation and the ability to interpolate in frequency are the accuracy-limiting aspects.

B. Derivatives

The forward model derivatives with respect to all the state vector elements need to be processed through the spectral averaging algorithms. The calculation is

$$\frac{\mathrm{d}I_{\mathrm{u,R,c}}(\mathbf{x},(\Omega))}{\mathrm{d}x_j} = \frac{\int_{\nu_{\mathrm{lo,R}}}^{\infty} \frac{\mathrm{d}I(\nu,\mathbf{x},(\Omega))}{\mathrm{d}x_j}\Phi_{\mathrm{R,c}}(\nu)\,\mathrm{d}\nu}{\int_{\nu_{\mathrm{lo,R}}}^{\infty} \Phi_{\mathrm{R,c}}(\nu)\,\mathrm{d}\nu} \tag{61}$$

None of the state vector quantities are expected to alter the channel filter shape so unlike the antenna averaging problem which requires special differential forms, none are needed for spectral averaging. The center frequency of the spectral channels may change during operations due to varying thermal environments. A first order correction for this effect can be done by shifting the molecular line positions whose derivative forms are given in Sections VI, VII, and [3].

C. DACS

Digital autocorrelator spectrometers (DACS) resolve narrow-line, Doppler-broadened emission from the Mesosphere and lower Thermosphere with 129 channels equally spaced across 12.5 MHz. DACS channels have $\sin(x)/x$ character where $x = \pi(\nu - \nu_{R,c})/\Delta\nu$ and $\Delta\nu$ is the channel spacing. The ringing tails of the channel responses are only significant when spectral features are sharp enough to be significantly truncated in the time (Fourier) domain by the limited number of lags in the autocorrelator. All DACS channels in a band may be modeled, in parallel, by boxcar truncation in the time domain of radiative transfer (and its derivative) calculations made on a high-spectral-resolution grid.

Each DACS receives power from the lower sideband of a single-sideband mixer with its LO at 905 MHz in the IF of a standard MLS 25-channel filter bank. This puts the center of the corresponding filter bank at 5 MHz in the DACS. A 10-MHz low-pass filter, $\Phi_{R,c}(\nu)$, after the DACS mixer prevents significant aliasing of signals from image bands above 12.5 MHz in the DACS IF. Note here that $\Phi_{R,c}(\nu)$ is common to all DACS channels in a band. Image bands are attenuated by 27 dB or more by the combined single-sideband mixer and low-pass cutoff of $\Phi_{R,c}(\nu)$, and are neglected in our calculations. Were their inclusion deemed to be necessary, radiative transfer calculations in image bands could be gridded, multiplied by the tails of $\Phi_{R,c}(\nu)$, and folded into the values used here.

When considering very sharp spectral features, the purity of the first local oscillators in the radiometers also becomes an issue. One can account for LO shape, $L_R(\nu)$, either by convolving it with the forward model radiative transfer calculations or by deconvolving it from measured radiances in level 1. In the former case, any blurring or multiple imaging caused by $L_R(\nu)$ is duplicated in the forward model, but the noise covariance of channels is nearly diagonal. In the latter case, spectral features are sharpened and multiple images are eliminated, but system noise, which is injected after the first mixer, is correlated between channels. MLS retrieval algorithms [4] do not account for off-diagonal noise-covariance elements, so we generally prefer to include convolution with $L_R(\nu)$ in the forward model. The variable magnitude of the spurs on the R3 LO is an exception, which is retrieved and deconvolved in level 1 processing [9].

The Discrete Cosine Transform (DCT) is used since the autocorrelation functions are real and symmetric in time. Convolution is implemented as multiplication in the Fourier domain.

Radiative transfer calculations are performed at discrete frequencies, which captures high-resolution spectral features. These values are interpolated to a 513-element grid over the range 0-12.5 MHz in the DACS IF, giving $I_k = I(\nu_k, \mathbf{x}, (\Omega))$ or $I_k = \frac{dI(\nu_k, \mathbf{x}, (\Omega))}{dx_j}$ on a 4x-oversampled, uniform grid. Ideally, one first convolves these radiances

with $L_{\mathrm{R}}(\nu)$, then multiplies by $\Phi_{\mathrm{R,c}}(\nu)$, performs a 513-element DCT, truncates to 129 elements in the time domain, and performs a 129-element inverse DCT. Channel normalizations are calculated by setting I_k to unity.

Were image bands to be included, $\Phi_{\mathrm{R,c}}(\nu)$ would cover all relevant spectra, and images would be folded in prior to the DCT. It has been shown in simulations that reversing the order of the convolution with $L_{\mathrm{R}}(\nu)$ and the multiplication with $\Phi_{\mathrm{R,c}}(\nu)$ does not significantly impact results in channels (20-80), which are used in MLS retrievals. This reversal allows us to eliminate the separate pair of DCT/DCT^{-1} transforms associated with $L_{\mathrm{R}}(\nu)$ convolution.

For DACS channels $\mathrm{c} = 0 \ldots 128$, channel radiances are

$$F = \frac{1}{N_{\mathrm{c}}} \sum_{j=-127}^{128} \sum_{i=-511}^{512} F_{|i|} \Phi_{|i|} \mathcal{L}_{|j|} \cos\left(\frac{ij\pi}{512}\right) \cos\left(\frac{\mathrm{c}\, j\pi}{128}\right) \tag{62}$$

where the normalization is

$$N_{\mathrm{c}} = \sum_{j=-127}^{128} \sum_{i=-511}^{512} \Phi_{|i|} \mathcal{L}_{|j|} \cos\left(\frac{ij\pi}{512}\right) \cos\left(\frac{\mathrm{c}\, j\pi}{128}\right) \tag{63}$$

and the DCT of the LO shape is

$$\mathcal{L}_j = \sum_{k=-127}^{128} L_{|k|} \cos\left(\frac{jk\pi}{128}\right), \tag{64}$$

where $F = I_{\mathrm{s,R,c}}(\mathbf{x}(\Omega))$ or $\frac{\mathrm{d}I_{\mathrm{s,R,c}}(\mathbf{x},(\Omega))}{\mathrm{d}x_j}$, $F_{|i|} = I(\nu_i, \mathbf{x}, (\Omega))$ or $\frac{\mathrm{d}I(\nu_i,\mathbf{x},(\Omega))}{\mathrm{d}x_j}$, $\Phi_{|i|} = \Phi_{\mathrm{R,c}}(\nu_i)$ and $L_{|j|} = L_{\mathrm{R}}(\nu_j)$. The vectors N, $\Phi_{\mathrm{R,c}}(\nu_i)$ and $\mathcal{L}$ are pre-tabulated.

IX. Field of View Integration

The far-field beam width of the EOS MLS receiving antenna contributes to the vertical shape of the radiance weighting function. This is the reason why (1) includes the weighted average of the antenna gain function G and the radiances I over the solid angle Ω.

A. Antenna Averaging

The spatial averaging part of (1) is expanded below [26]

$$\begin{aligned} I_{\mathrm{s,R,c}}(\mathbf{x}(\varepsilon_t, \alpha_t)) = \mathrm{Tr} \int_{\alpha_A} \int_{\varepsilon_A} & \mathbf{I}_{\mathrm{s,R,c}}(\mathbf{x}(\varepsilon, \alpha)) \\ & \times \mathbf{G}_{\mathrm{s,R,c}}(\varepsilon_t - \varepsilon, \alpha_t - \alpha) \cos\varepsilon \mathrm{d}\varepsilon \mathrm{d}\alpha \\ & / \mathrm{Tr} \int_{\alpha_A} \int_{\varepsilon_A} \mathbf{G}_{\mathrm{s,R,c}}(\varepsilon_t - \varepsilon, \alpha_t - \alpha) \cos\varepsilon \mathrm{d}\varepsilon \mathrm{d}\alpha, \end{aligned} \tag{65}$$

where $\mathbf{G}_{\mathrm{s,R,c}}(\varepsilon_t - \varepsilon, \alpha_t - \alpha)$ is the polarized far field antenna pattern, Tr is the trace of a matrix, $\mathbf{I}_{\mathrm{s,R,c}}(\mathbf{x}(\varepsilon, \alpha))$, the channel averaged radiance in coherency matrix format [27], angles ε and α are elevation (vertical) and azimuth (cross-track) angular components of solid angle, Ω, and α_A and ε_A are a portion of the total solid angle Ω for which $\mathbf{G}_{\mathrm{s,R,c}}(\varepsilon_t - \varepsilon, \alpha_t - \alpha)$ has been measured. As usual subscript t refers to the ray path tangent. The angles ε_t and α_t are defined in the instrument FOV pointing frame (IFOVPF) where the origin is the observatory, z axis is

coincident with s in Fig. 7, x points down, toward the Earth, nominally in the orbital plane or the x-y plane of Fig. 7, and y is perpendicular in a right-handed axis system. The solution of this equation is described in detail in [28].

Equation (65) is transformed into a convolution equation. $\mathbf{I}_{\mathrm{s,R,c}}\left(\mathbf{x}\left(\varepsilon,\alpha\right)\right)$ for unpolarized radiation is $I_{\mathrm{s,R,c}}\left(\mathbf{x}\left(\varepsilon,\alpha\right)\right)\mathbf{1}$ where $\mathbf{1}$ is an identity matrix. We neglect cross-track gradients (variations in α). This approximation is necessary because it would be necessary to add another dimension (a cross-track angle) to the state vector components. The EOS MLS radiance data and spatial sampling do not provide the necessary information to measure the cross-track gradient. Neglecting cross-track gradients should be relatively minor because The cross-track beam width of the EOS MLS antenna (3–12 km, depending on radiometer frequency), is much smaller than the along-track basis sampling ($\sim$160 km) resolution. Neglecting cross-track gradients collapses the antenna pattern calculation into one dimension. Finally, elevation angle ε is assumed to be in the LOSF x–y plane, Fig. 7. In general, the plane ε defines is slightly skewed from the x-y plane of Fig. 7 because there are always imperfections in instrument mounting and spacecraft attitude. Folding in these approximations gives

$$I_{\mathrm{s,R,c}}\left(\mathbf{x}\left(\chi_{\mathrm{eq}}^{\mathrm{refr}}\right)\right)=\int_{-\infty}^{\infty}I_{\mathrm{s,R,c}}\left(\mathbf{x}\left(\chi\right)\right)\overline{G}_{\mathrm{s,R,c}}\left(\chi_{\mathrm{eq}}^{\mathrm{refr}}-\chi\right)\mathrm{d}\chi, \tag{66}$$

where the "linearized" independent coordinate χ is the elevation angle in the LOSF (not IFOVPF), $I_{\mathrm{s,R,c}}\left(\mathbf{x}\left(\chi\right)\right)$ is the channel averaged radiance (Section VIII), $\overline{G}_{\mathrm{s,R,c}}\left(\chi_{\mathrm{eq}}^{\mathrm{refr}}-\chi\right)$ is the sum of the co- and cross-polarized antenna gain functions. $\overline{G}_{\mathrm{s,R,c}}$ is normalized to unit area. The approximation neglecting the projection of the antenna pattern in a plane defined by ε as projected onto a plane defined by χ causes an underestimate of the HPBW. This is because in the general case the antenna pattern in χ coordinates is a linear combination of the elevation and azimuthal patterns, the latter being twice as broad. However, for the small difference between these planes expected here, the additional broadening is a negligible second order effect.

Independent coordinate χ is linearized by applying the small angle approximation $\sin\left(\varepsilon_t-\varepsilon\right)\approx\chi_{\mathrm{eq}}^{\mathrm{refr}}-\chi$. The direction angle $\chi_{\mathrm{eq}}^{\mathrm{refr}}$ is the pointing angle corrected for refraction pointing to a ζ_t in the equivalent circular Earth coordinates (Fig. 7). The refracted angle relates to the tangent height according to

$$\sin\chi_{\mathrm{eq}}^{\mathrm{refr}}=\mathcal{N}_t\frac{H_t}{H_s}, \tag{67}$$

Where H_s is the spacecraft distance from the equivalent circular Earth. H_s is not the same as R_s, the geocentric spacecraft height supplied by Aura flight operations. The conversion is straightforward but requires a considerable amount of additional data [3]. $\vec{H}_s$ can be computed with adequate accuracy with the following empirical formula

$$H_s\approx R_s\left(\mathrm{ECR\ or\ ECI}\right)+38.9\sin\left[2\left(\phi_t-51.6\right)\right]. \tag{68}$$

For EOS MLS, the error in eq. 68 is less than 0.55 km. It can be shown that this has negligible impact. The spacecraft geocentric height affects the accuracy of the forward model by distorting the antenna shape. The half power beam width (HPBW) is an angular characteristic of the antenna's FOV that describes its resolving ability. More important is the projection of the antenna HPBW on the limb tangent, given by

$$\Delta h_{\mathrm{hpbw}}=\Delta\chi_{\mathrm{hpbw}}\sqrt{H_s^2-\left(H_t^{\oplus}+h\right)^2}, \tag{69}$$

where $\Delta\chi_{\text{hpbw}}$ is the antenna HPBW in radians. Differentiating (69) gives

$$\mathrm{d}\Delta h_{\text{hpbw}} = \frac{\Delta\chi_{\text{hpbw}}\left[H_s \mathrm{d}H_s - \left(H_t^{\oplus}+h\right)\left(\mathrm{d}H_t^{\oplus} + \frac{\mathrm{d}h}{\mathrm{d}T}\mathrm{d}T\right)\right]}{\sqrt{H_s^2 - \left(H_t^{\oplus}+h\right)^2}}. \tag{70}$$

According to (70), an error of 0.6 km for $H_s$is equivalent to a HPBW error of 3 meters in tangent height for an antenna with a HPBW of 6 km. This is 0.05% of the HPBW, which is entirely negligible compared to the uncertainty in knowledge of the antenna HPBW (a few percent) [10], [11].

Equation (66) is solved using fast Fourier transforms (FFT). The FFT solution requires that the antenna beam width doesn't change with scan position. The antenna shape is measured prior to launch as part of instrument calibration including its scan dependence. It can be shown that the measured pattern at the scan extrema of ($\sim$ 150 km tangent) if applied at a nominal tangent of 30 km could lead to radiance errors as large as 0.5 K where the radiance growth rate with respect to height is fastest [10]. In practice, the pattern used is much more closely matched to the altitude where the radiance growth curve is maximum and therefore the scan dependence error should be much less but is yet to be quantified. The FFT convolution requires $I(\chi)$ to be evaluated for several χs. The spatial averaging of $I(\chi)$ uses radiances calculated along the scanned LOS ϕ_t instead of those instantly observed by the FOV at a given LOS tangent ϕ_t. Fig. 11 shows the implication of this approximation. The diamonds show the scanned LOS ϕ_t with refraction included, the triangles show the instantaneous ϕ_t seen by the antenna for one FOV direction LOS ϕ_t (middle triangle). The vertical spread of the triangles is for the EOS MLS 118 GHz radiometer that has the largest HPBW. When there are ϕ_t gradients, an error in the antenna averaging is introduced by the lack of co-alignment between the diamonds and triangles. The error is most severe in the troposphere and lower stratosphere where the scanned LOS ϕ_t and instantaneous FOV LOS ϕ_t have opposite slopes but fortunately refraction of the scanned LOS ϕ_t helps to mitigate this difference. The error implied by this approximation is not known. A rough estimate of this error, at a given ζ_t, should be proportional to the difference in the instantaneous difference between the antenna observed ϕ_t and the scanned ϕ_t times the horizontal radiance gradient $\frac{\mathrm{d}I}{\mathrm{d}\phi_t}$. This approximation is tolerable because the difference between the antenna received ϕ_t and the scanned ϕ_t within the HPBW of the antenna is usually less than 10% of the basis sampling.

The Fourier transform theorem of convolutions is

$$\mathcal{F}t\left(I_{\text{s,R,c}}\left(\mathbf{x}\left(\chi_{\text{eq}}^{\text{refr}}\right)\right)\right) = \mathcal{F}t\left(I_{\text{s,R,c}}\left(\mathbf{x}\left(\chi\right)\right)\right) \times \mathcal{F}t\left(\overline{G}_{\text{mi,s,R,c}}\left(\chi\right)\right). \tag{71}$$

The Fourier transform convolution theorem requires that $\overline{G}_{\text{mi,s,R,c}}(\chi)$ is the mirror image of $\overline{G}_{\text{s,R,c}}\left(\chi_{\text{eq}}^{\text{refr}} - \chi\right)$. The Fourier transform of the antenna gain pattern can be calculated and stored. An advantage to doing this in addition to avoiding repetitive FFT calculations is that the resulting autocorrelation of the field pattern should be zero beyond twice the aperture distance; the first point in the pattern is the normalization factor and negating the imaginary part of the aperture autocorrelation pattern is the required mirror image. Truncating the aperture autocorrelation pattern provides some noise filtering. This was not done for EOS MLS GHz patterns because of uncertainty of the actual aperture size; however, it is done for the THz patterns.

A 4096 point FFT is used in (71). 2050 points are used for the limb radiances covering the measured antenna pattern, which is 140 m per point. The remaining 2046 points are the mirror image of limb radiances (not including point 1 and 2050, which must remain unique to produce a real transform). The Earth surface limb radiance is point 738. This causes the Earth to fill 36% of the entire FOV as it does in orbit, but recognize that this is purely a cosmetic feature because we only consider about 6° of antenna pattern. However it produces a graceful means of joining the low space radiances to the high Earth viewing radiances, which is necessary to avoid high frequency oscillations in the transform that would result if there is a sudden transition between the Earth and space radiance values. The interpolation of radiances, which is based on tangent pressures given in the PSIG to 2050 χ values uses cubic spline interpolation according to

$$I_{s,R,c}\left(\mathbf{x}\left(\chi_{eq}^{refr}(2050)\right)\right) = \text{Interp}\left(\chi_{eq}^{refr}(PSIG), I_{s,R,c}\left(\mathbf{x}\left(\chi_{eq}^{refr}(PSIG)\right)\right), \chi_{eq}^{refr}(2050)\right), \quad (72)$$

where the Interp operator estimates the function given in its second argument whose independent coordinate is given in the first argument (both on the PSIG) at the values given in the third argument (2050 equally spaced χ_{eq}^{refr} values) with cubic splines.

B. Radiometer Offsets

The FOV directions of the instrument radiometers are not exactly co-aligned; however, it is advantageous to reference the pointings of the bands of radiometers to a common reference. This allows one tangent pressure measurement to be applied to all the bands. Therefore the χ_{eq}^{refr}, are adjusted for these radiometer alignment differences according to

$$\chi_{eq}^{ref,refr} = \chi_{eq}^{refr} - \Delta\chi_{eq,s,R,c}^{refr}, \quad (73)$$

where $\Delta\chi_{eq,s,R,c}^{refr}$ is the radiometer FOV direction offset angle between radiometer R, band/channel c, for sideband, s, and the reference $\chi_{eq}^{ref,refr}$ in the LOSF (a positive offset points lower than the reference). χ_{eq}^{refr} are the angles of the tangent pressures in the PSIG used to compute $I(\nu, \mathbf{x}(\Omega))$, (39).

C. Measured Limb Radiances

The radiances on the scan LOS tangents are computed according to

$$I_{s,R,c}\left(\mathbf{x}\left(\chi_{eq}^{ref,refr}\right)\right) = \text{Interp}\left(\chi_{eq}^{refr}, I_{s,R,c}\left(\mathbf{x}\left(\chi_{eq}^{refr}\right)\right), \chi_{eq}^{refr} - \Delta\chi_{eq,s,R,c}^{refr}\right), \quad (74)$$

where the first two arguments are the 4096 angles and radiances following (71), the third argument is the scanned LOS measured χ_{eq}^{refr} evaluated at the measured reference tangent ζ_t. The Interp operator for radiances is a cubic spline interpolator.

D. Radiance derivatives

The radiance derivative with respect to tangent pressure is immediately available from the cubic spline coefficients used to get the radiances. If the interpolation is done in pointing angle units, then the radiance derivative with respect to pointing angle needs to be multiplied by $\frac{\mathrm{d}\zeta_t}{\mathrm{d}\chi_{\mathrm{eq}}^{\mathrm{ref,refr}}} = H_s \frac{\mathcal{N}_t \cos\chi_{\mathrm{eq}}^{\mathrm{refr}} - \sin\chi_{\mathrm{eq}}^{\mathrm{refr}} (\mathrm{d}\mathcal{N}_t/\mathrm{d}\zeta_t)}{\mathcal{N}_t^2} \frac{\mathrm{d}\zeta_t}{\mathrm{d}H_t}$, where $\frac{\mathrm{d}\zeta_t}{\mathrm{d}H_t}$ is the reciprocal of the last two lines in (49). The derivative of the antenna smeared radiance with respect to a state vector element (except tangent pressure or LOS angle) is given by

$$\begin{aligned}\frac{\mathrm{d}I_{\mathrm{s,R,c}}\left(\mathbf{x}\left(\chi_{\mathrm{eq}}^{\mathrm{ref,refr}}\right)\right)}{\mathrm{d}x_j} = & \\ & \int_{-\infty}^{\infty}\left[\frac{\mathrm{d}I}{\mathrm{d}x_j} + I\frac{\mathrm{d}}{\mathrm{d}\chi}\left(\frac{\mathrm{d}\chi}{\mathrm{d}x_j}\right)\right]\overline{G}_{\mathrm{s,R,c}}\left(\chi_{\mathrm{eq}}^{\mathrm{refr}} - \chi\right)\mathrm{d}\chi \\ & + \frac{\mathrm{d}\chi_{\mathrm{eq}}^{\mathrm{refr}}}{\mathrm{d}x_j}\int_{-\infty}^{\infty} I\frac{\mathrm{d}\overline{G}_{\mathrm{s,R,c}}\left(\chi_{\mathrm{eq}}^{\mathrm{refr}} - \chi\right)}{\mathrm{d}\left(\chi_{\mathrm{eq}}^{\mathrm{refr}} - \chi\right)}\mathrm{d}\chi \\ & - \int_{-\infty}^{\infty} I\frac{\mathrm{d}\chi}{\mathrm{d}x_j}\frac{\mathrm{d}\overline{G}_{\mathrm{s,R,c}}\left(\chi_{\mathrm{eq}}^{\mathrm{refr}} - \chi\right)}{\mathrm{d}\left(\chi_{\mathrm{eq}}^{\mathrm{refr}} - \chi\right)}\mathrm{d}\chi, \end{aligned} \quad (75)$$

where x_j is a state vector element and $I \equiv I_{\mathrm{s,R,c}}\left(\mathbf{x}\left(\chi_{\mathrm{eq}}^{\mathrm{refr}}\right)\right)$ for brevity. In most cases, x_j is non geometrical (that is, has no effect on heights of pressure surfaces) and all the $\frac{\mathrm{d}\chi}{\mathrm{d}x_j} = 0$, simplifying (75) considerably. Exceptions to this are temperature (affects heights through the hydrostatic model), equivalent circular Earth radius and spacecraft geocentric altitude. Although the antenna pattern is invariant in its angular properties, its beam width in pressure units does change whenever the observing geometry is altered.

The angular derivatives in (75) are given by

$$\begin{aligned}\frac{\mathrm{d}\chi}{\mathrm{d}f_{lm}^T} &= \frac{\tan\chi}{H_t}\frac{\mathrm{d}H_t}{\mathrm{d}f_{lm}^T}, \\ \frac{\mathrm{d}}{\mathrm{d}\chi}\left(\frac{\mathrm{d}\chi}{\mathrm{d}f_{lm}^T}\right) &= \frac{2+\tan^2\chi}{H_t}\frac{\mathrm{d}H_t}{\mathrm{d}f_{lm}^T} + \frac{\eta_l^T\eta_m^T}{T_t}, \\ &= \frac{\tan^2\chi}{H_t}\frac{\mathrm{d}H_t}{\mathrm{d}f_{lm}^T} + \frac{\mathrm{d}}{\mathrm{d}H_t}\left(\frac{\mathrm{d}H_t}{\mathrm{d}f_{lm}^T}\right), \\ \frac{\mathrm{d}\chi}{\mathrm{d}H_s} &= -\frac{\tan\chi}{H_s}, \\ \frac{\mathrm{d}}{\mathrm{d}\chi}\left(\frac{\mathrm{d}\chi}{\mathrm{d}H_s}\right) &= -\frac{1}{H_s\cos^2\chi}, \\ \frac{\mathrm{d}\chi}{\mathrm{d}H_t^{\oplus}} &= \frac{\tan\chi}{H_t}, \\ \frac{\mathrm{d}}{\mathrm{d}\chi}\left(\frac{\mathrm{d}\chi}{\mathrm{d}H_t^{\oplus}}\right), &= \frac{1}{H_t\cos^2\chi}, \end{aligned} \quad (76)$$

where T_t is temperature at the limb tangent. The derivations of the temperature forms are given in [3]. Contributions from $\frac{\mathrm{d}\mathcal{N}_t}{\mathrm{d}T}$ have been neglected. Expanded forms including $\frac{\mathrm{d}\mathcal{N}_t}{\mathrm{d}T}$ are in [3], but numerical experiments show that these contributions can be ignored. The H_t is evaluated for each tangent height for all the ray tracings. $\frac{\mathrm{d}\overline{G}_{\mathrm{s,R,c}}\left(\chi_{\mathrm{eq}}^{\mathrm{refr}} - \chi\right)}{\mathrm{d}\left(\chi_{\mathrm{eq}}^{\mathrm{refr}} - \chi\right)}$ is

evaluated using the FT derivative property

$$\mathcal{F}t\left(\frac{\mathrm{d}\overline{G}_{\mathrm{mi,s,R,c}}(\chi)}{\mathrm{d}\chi}\right) = iq\mathcal{F}t\left(\overline{G}_{\mathrm{mi,s,R,c}}(\chi)\right) \tag{77}$$

where q is the aperture independent coordinate (number of wavelengths), and $i=\sqrt{-1}$. This definition is convenient because the pattern is stored as $\mathcal{F}t\left(\overline{G}_{\mathrm{mi,s,R,c}}(\chi)\right)$ and ensures internal consistency between the pattern and its derivative. Equation (75) is evaluated with a 4096 point transform. However, linear interpolation is used in (72) and (74) because the radiance derivatives with respect to many of the state vector elements may be too stiff for cubic splines.

Here we discuss some practical issues with evaluating (75). First, since rays reflect off the Earth surface, temperature cannot influence H_t when it is less than $H_t^{\oplus}$ and state vector variable ζ_t doesn't exist. If one ignores this fact by artificially extrapolating the pressure to larger values, an erroneous spike in the lowest coefficient of $\frac{\mathrm{d}I}{\mathrm{d}f_{lm}^T}$ occurs. To eliminate this and also do the calculation in the physically correct fashion, $\frac{\mathrm{d}\chi}{\mathrm{d}f_{lm}^T}=0$ for all $\chi_{\mathrm{eq}}^{\mathrm{refr}}$ that point below $H_t^{\oplus}$. Therefore one has to be careful that the same Earth radius is used throughout the calculation. The second problem is numerical. The following must be true,

$$\int_{-\infty}^{\infty}\frac{\mathrm{d}}{\mathrm{d}\chi}\left(\frac{\mathrm{d}\chi}{\mathrm{d}x_j}\right)\overline{G}_{\mathrm{s,R,c}}\left(\chi_{\mathrm{eq}}^{\mathrm{refr}}-\chi\right)\mathrm{d}\chi - \int_{-\infty}^{\infty}\frac{\mathrm{d}\chi}{\mathrm{d}x_j}\frac{\mathrm{d}\overline{G}_{\mathrm{s,R,c}}\left(\chi_{\mathrm{eq}}^{\mathrm{refr}}-\chi\right)}{\mathrm{d}\left(\chi_{\mathrm{eq}}^{\mathrm{refr}}-\chi\right)}\mathrm{d}\chi = 0. \tag{78}$$

In other words there should be no sensitivity to the antenna beam shape if there is no gradient in the radiance profile. Calculations assuming constant I showed that this is not the case, a result of imperfect numerics. The error peaks at the maximum of $\frac{\mathrm{d}}{\mathrm{d}\chi}\left(\frac{\mathrm{d}\chi}{\mathrm{d}x_j}\right)$. Therefore to mitigate this error we subtract the anticipated error pattern from the calculation of (75). This is easily done by setting $I=I-I_M$ in the first and third terms on the right-hand side of (75), where I_M is I at the height where $\frac{\mathrm{d}}{\mathrm{d}\chi}\left(\frac{\mathrm{d}\chi}{\mathrm{d}x_j}\right)$ is maximum. This trick eliminated an annoying spike-like feature that affected all temperature coefficients with non-zero $\eta_m^k(\phi_t)$ and improved agreement with finite difference comparisons.

X. Fold Sidebands

Following the antenna averaging, the upper and lower sidebands are folded according to

$$\begin{aligned} I_{\mathrm{R,c}}\left(\mathbf{x}\left(\chi_{\mathrm{eq}}^{\mathrm{ref,refr}}\right)\right) = {} & r_{\mathrm{u,R,c}}I_{\mathrm{u,R,c}}\left(\mathbf{x}\left(\chi_{\mathrm{eq}}^{\mathrm{ref,refr}}\right)\right) \\ & + r_{\mathrm{l,R,c}}I_{\mathrm{l,R,c}}\left(\mathbf{x}\left(\chi_{\mathrm{eq}}^{\mathrm{ref,refr}}\right)\right) \end{aligned} \tag{79}$$

XI. Scan Averaging

The EOS MLS scans continuously while the radiometric measurement is being made, which means that there will be some additional spatial averaging on top of that done by the FOV. This is the time integral in (1). Although the v1.5 Level 2 processing ignores the scan averaging effect, it is useful to provide the algorithm because scan averaging will be included in the next EOS MLS processing version and it provides an error estimate incurred

from its exclusion. The amount of movement is expected to be small relative to the FOV patterns and therefore less critical to modeling details. The scan angle change with respect to time may follow a function like

$$\chi_{\mathrm{eq}}^{\mathrm{ref,refr}}(t) = \chi_{\mathrm{eq}}^{\mathrm{ref,refr}}(t_1) + \frac{\Delta\chi_{\mathrm{eq}}^{\mathrm{ref,refr}}}{\Delta t}(t-t_1) + \Delta\chi_A \sin(\omega t + \phi(t_1)), \quad (80)$$

where $\Delta\chi_{\mathrm{eq}}^{\mathrm{ref,refr}} = \chi_{\mathrm{eq}}^{\mathrm{ref,refr}}(t_2) - \chi_{\mathrm{eq}}^{\mathrm{ref,refr}}(t_1)$ and $\Delta t = t_2 - t_1$. This equation assumes a linear (constant velocity) change in pointing angle with respect to time. Added to this is an oscillation (jitter) function having a peak-to-peak value of $2\Delta\chi_A$, frequency ω and initial phase $\phi(t_1)$. Let $I_{\mathrm{R,c}}\left(\mathbf{x}\left(\chi_{\mathrm{eq}}^{\mathrm{ref,refr}}\right)\right)$ be a vector of instantaneous radiances ((71)) corresponding to $\chi_{\mathrm{eq}}^{\mathrm{ref,refr}}$. Let $I'_{\mathrm{R,c}}\left(\mathbf{x}\left(\chi_{\mathrm{eq}}^{\mathrm{ref,refr}}\right)\right)$ be the first derivative with respect to $\chi_{\mathrm{eq}}^{\mathrm{ref,refr}}$. The time averaged radiance for an integration between t_1 and t_2 assuming a cubic spline-like function between time t_1 and t_2 is

$$\begin{aligned}\left(\overset{\bullet}{I} - I_{\mathrm{bl}}\right)_{\mathrm{R,c}}(\mathbf{x}) - \mathrm{BL}_{\mathrm{R},t} = \\ \frac{1}{\Delta t}\int_{t_1}^{t_2} & I_{\mathrm{R,c}}\left(\mathbf{x}\left(\chi_{\mathrm{eq}}^{\mathrm{ref,refr}}(t_1)\right)\right)(1-x)^2(1+2x) \\ & + I_{\mathrm{R,c}}\left(\mathbf{x}\left(\chi_{\mathrm{eq}}^{\mathrm{ref,refr}}(t_2)\right)\right)x^2(3-2x) \\ & + I'_{\mathrm{R,c}}\left(\mathbf{x}\left(\chi_{\mathrm{eq}}^{\mathrm{ref,refr}}(t_1)\right)\right)\Delta\chi_{\mathrm{eq}}^{\mathrm{ref,refr}} x(1-x)^2 \\ & + I'_{\mathrm{R,c}}\left(\mathbf{x}\left(\chi_{\mathrm{eq}}^{\mathrm{ref,refr}}(t_2)\right)\right)\Delta\chi_{\mathrm{eq}}^{\mathrm{ref,refr}} x^2(x-1)\,\mathrm{d}t, \quad (81)\end{aligned}$$

where $I_{\mathrm{R,c}}\left(\mathbf{x}\left(\chi_{\mathrm{eq}}^{\mathrm{ref,refr}}(t)\right)\right)$ and $I'_{\mathrm{R,c}}\left(\mathbf{x}\left(\chi_{\mathrm{eq}}^{\mathrm{ref,refr}}(t)\right)\right)$ are evaluated from a cubic spline at $t = t_1$, and t_2, and x is $\left(\chi_{\mathrm{eq}}^{\mathrm{ref,refr}}(t) - \chi_{\mathrm{eq}}^{\mathrm{ref,refr}}(t_1)\right)/\Delta\chi_{\mathrm{eq}}^{\mathrm{ref,refr}}$. Substituting (80) into (81) and integrating gives the result. If the jitter term in (80) is ignored the scan motion integral is

$$\begin{aligned}\left(\overset{\bullet}{I} - I_{\mathrm{bl}}\right)_{\mathrm{R,c}}(\mathbf{x}) - \mathrm{BL}_{\mathrm{R},t} = \\ \frac{1}{2}\left(I_{\mathrm{R,c}}\left(\mathbf{x}\left(\chi_{\mathrm{eq}}^{\mathrm{ref,refr}}(t_1)\right)\right) + I_{\mathrm{R,c}}\left(\mathbf{x}\left(\chi_{\mathrm{eq}}^{\mathrm{ref,refr}}(t_2)\right)\right)\right) \\ + \frac{\Delta\chi_{\mathrm{eq}}^{\mathrm{ref,refr}}}{12}\left(I'_{\mathrm{R,c}}\left(\mathbf{x}\left(\chi_{\mathrm{eq}}^{\mathrm{ref,refr}}(t_1)\right)\right) - I'_{\mathrm{R,c}}\left(\mathbf{x}\left(\chi_{\mathrm{eq}}^{\mathrm{ref,refr}}(t_2)\right)\right)\right). \quad (82)\end{aligned}$$

As it stands (82) is awkward because it introduces two pointings (at t_1 and t_2) for each radiance. Cubic spline interpolation is used to evaluate $\chi_{\mathrm{eq}}^{\mathrm{ref,refr}}(t)$ and $I_{\mathrm{R,c}}\left(\mathbf{x}\left(\chi_{\mathrm{eq}}^{\mathrm{ref,refr}}(t)\right)\right)$ at t_1 and t_2. The tangent pressure of $\left(\overset{\bullet}{I} - I_{\mathrm{bl}}\right)_{\mathrm{R,c}}(\mathbf{x})$ is the tangent pressure at $0.5(t_1+t_2)$.

A. Derivatives

The basic derivative form is

$$\begin{aligned}\frac{\mathrm{d}\left(\overset{\bullet}{I} - I_{\mathrm{bl}}\right)_{\mathrm{R,c}}(\mathbf{x}) - \mathrm{BL}_{\mathrm{R},t}}{\mathrm{d}x_j} = \\ \frac{1}{2}\left(\frac{\mathrm{d}I_1}{\mathrm{d}x_j} + \frac{\mathrm{d}I_2}{\mathrm{d}x_j}\right) + \frac{\Delta\chi_{\mathrm{eq}}^{\mathrm{ref,refr}}}{12}\left(\frac{\mathrm{d}I'_1}{\mathrm{d}x_j} - \frac{\mathrm{d}I'_2}{\mathrm{d}x_j}\right), \quad (83)\end{aligned}$$

where $I_1 = I_{\mathrm{R,c}}\left(\mathbf{x}\left(\chi_{\mathrm{eq}}^{\mathrm{ref,refr}}(t_1)\right)\right)$, $I_2 = I_{\mathrm{R,c}}\left(\mathbf{x}\left(\chi_{\mathrm{eq}}^{\mathrm{ref,refr}}(t_2)\right)\right)$, and x_j is any state vector element. The derivatives $\frac{\mathrm{d}I_1}{\mathrm{d}x_j}$and $\frac{\mathrm{d}I_2}{\mathrm{d}x_j}$ are evaluated at the time boundaries with linear interpolation.

Errors caused by neglecting scan averaging in the Level 2 processing is given here. The first term in eq. 82 is simply the average of the two instantaneous radiances at the boundaries. If the radiance growth between the breakpoints is linear and the antenna scans at constant velocity, the scan smoothed radiance field is the same as the instantaneous radiance at $t = 0.5\,(t_1 + t_2)$, which is consistent with the level 2 usage. However, non-linearities of the radiance growth field affect the scan averaging and within the limitations stated above, is given in the second term of eq. 82. Therefore the second term of eq. 82 is an error estimate caused by neglecting the scan smoothing. The typical maximum error is 0.15 K over that portion of the radiance profile where $\mid \frac{\mathrm{d}I}{\mathrm{d}\chi_{\mathrm{eq}}^{\mathrm{ref,refr}}} \mid$ is largest; however, some notable exceptions are: R1 it is 0.3 K in the stratosphere and 0.6 K in the mesosphere and R5H or R5V it is 1.1 K in the troposphere, 0.05 K in the stratosphere and 0.2 K in the mesosphere. The higher values are consistent with the scan rate, which is largest in the mesosphere for the GHz radiometers and largest in the troposphere for the terahertz radiometer.

XII. Add Baseline

The final operation is adding $\mathrm{BL}_{\mathrm{R},t}$ to the result from (82). As presented, the baseline is a spectrally flat additive quantity that empirically accounts for unmodelled instrument artifacts such as errors in evaluating the $(I_{\mathrm{bl}})_{\mathrm{R,c}}$ term. Although such errors are not expected to be scan dependent, experience from both UARS and EOS MLS experiments have shown that retrieved $\mathrm{BL}_{\mathrm{R},t}$ has psuedo-vertical structure possibly suggesting an atmospheric component or a temporal instrumental effect. Another baseline-like quantity is EXTINCTION which is an additive absorption coefficient. When the atmosphere is optically thin, EXTINCTION and $\mathrm{BL}_{\mathrm{R},t}$ affect the radiances similarly. Their behavior is different when the atmosphere is optically thick. EXTINCTION will cause some distortion of molecular line shapes in optically thick situations and when the atmosphere becomes opaque, the forward model has no sensitivity to EXTINCTION and therefore it is unable to influence the radiances. In contrast, $\mathrm{BL}_{\mathrm{R},t}$ never distorts line shapes and can influence radiances regardless of the atmospheric opacity. If unexplained radiance is coming from the atmospheric absorption, then EXTINCTION is a better baseline parameter; however, if the unexplained radiance is mostly an instrumental effect or a radiation scattering effect from thick clouds, then $\mathrm{BL}_{\mathrm{R},t}$ is better because $\mathrm{BL}_{\mathrm{R},t}$ can influence radiances in optically thick situations and follow radiance supression caused by radiation scattering from thick clouds [5]. Due to the robust nature of $\mathrm{BL}_{\mathrm{R},t}$, we decided to use it instead of EXTINCTION in the early EOS MLS Level 2 processing versions. It is also noteworthy that $\vec{\mathrm{BL}}_{\mathrm{R},t}$ constitute a significant number of state vector elements (437000 per day per radiometer). Initially, baseline was handled like a regular quantity, that is it had a predefined vertical and horizontal basis like temperature, but shortly after launch, parameterizing baseline this way produced very poor results especially for noisy species like BrO [4]. It has since been discovered that the instrument noise in R4 is highly correlated across its channels [9] and that a baseline set up as an irregular quantity as described here worked much better.

The derivative of the radiances with respect to baseline is,

$$\frac{\mathrm{d}\left(\overset{\bullet}{I}-I_{\mathrm{bl}}\right)_{\mathrm{R,c}}(\mathbf{x})-\mathrm{BL}_{\mathrm{R},t}}{\mathrm{dBL}_{\mathrm{R}',t'}}=\begin{cases}1 & t'=t \text{ and } \mathrm{R}'=\mathrm{R}\\ 0 & t'\neq t \text{ or } \mathrm{R}'\neq\mathrm{R},\end{cases} \tag{84}$$

where t and R are the limb tangent and radiometer for the radiance calculation and t' and R$'$ are the same for the baseline state vector element.

The derivative of the radiance with respect to the non baseline state vector elements is

$$\frac{\mathrm{d}\left(\overset{\bullet}{I}-I_{\mathrm{bl}}\right)_{\mathrm{R,c}}(\mathbf{x})}{\mathrm{d}x_j}=\frac{\mathrm{d}\left(\overset{\bullet}{I}-I_{\mathrm{bl}}\right)_{\mathrm{R,c}}(\mathbf{x})-\mathrm{BL}_{\mathrm{R},t}}{\mathrm{d}x_j}+\frac{\mathrm{dBL}_{\mathrm{R},t}}{\mathrm{d}x_j}. \tag{85}$$

The derivative of the baseline with respect to x_j doesn't exist for any non baseline element. It is arguable if $\frac{\mathrm{dBL}_{\mathrm{R},t}}{\mathrm{d}\zeta_t}=\frac{\mathrm{dBL}_{\mathrm{R},t}}{\mathrm{d}\phi_t}=0$. These derivatives are zero if the baseline is coming from the instrument in a scan independent way. In other words the baseline retrieval is responding to temporal variations in the instrument. Because of the correlated noise observed in R4 [9], the current level 2 processing assumes this to be the case [4].

XIII. The Scan Model

The EOS MLS FOV is scanned through the atmosphere and the FOV direction (i.e. angle) is measured and available for use. The scan measurements are the level 1 unrefracted tangent heights midway through the minor frame (i.e. $0.5\,(t_1+t_2)$). The level 1 heights are convenient because they include the effects of many alignment and spacecraft attitude angles and the spacecraft velocity into one measurement quantity and as long as one is not particularly interested in retrieving or properly accounting for covariances in any of these quantities except for the height itself, this approach is easier. The measurement to fit is

$$\vec{0}=\left[U_r\left(\vec{R}_t\right)-\Delta U_r\left(\vec{\zeta}_t\right)-U_r\left(R_{\mathrm{ref}}\right)\right]/g_o, \tag{86}$$

where $\vec{0}$ is the scan residual, $U_r\left(\vec{R}_t\right)$ is the geopotential (16) computed from heights given by orbit attitude measurements, $\Delta U_r\left(\vec{\zeta}_t\right)$ is the atmospheric geopotential offset relative to $Z_{\mathrm{refgeopot}}$, $U_r\left(R_{\mathrm{ref}}\right)$ is the geopotential of the reference geopotential height, $Z_{\mathrm{refgeopot}}$, R_{ref} is the reference geometric height, and $g_o=9.80665\ \mathrm{ms}^{-2}$ (converts geopotential units to height units). The scan model uses geometric quantities defined with respect to the center of the Earth figure ellipse in Fig. 5. The vector designation means that this quantity is a that is irregularly gridded whose height points are given by state vector component "tangent pressure, ζ_t." These are sampling points during a single profile scan [29]. The scan residual $\vec{0}$ has geopotential height units (m) with an uncertainty that is the diagonal elements of the root sum square of the covariances of all the quantities used to compute height. The geocentric heights in (86) of the state vector component ζ_t include refraction, which itself depends on pressure, temperature and water vapor, all state vector quantities. A simple way to get all the state vector quantities to the right of the = in (86) is to reference the measurement against zero with an uncertainty as previously defined. This avoids the need to invert (16) for geocentric height.

The orbit attitude derived heights do not include refraction; they are converted to a refracted height according to,

$$\vec{R}_t = \frac{\vec{R}_{\text{geom}}}{\vec{\mathcal{N}}_t}, \tag{87}$$

where $\vec{R}_{\text{geom}}$ are the orbit attitude estimated geocentric heights, and $\vec{\mathcal{N}}_t$ is the refractive index given in (25). Tangent pressure for a subsurface height is not defined; however, to accommodate the level 2 retrieval, which extrapolates tangent pressure downward, we freeze $\vec{\mathcal{N}}_t$ to the surface value for $\vec{R}$ pointing below the surface.

Fig. 10 and Fig. 11, ϕ_t depends on refraction. The difference between the refracted and unrefracted ϕ_t (a level 1 quantity) can be computed according to (24) or a table of corrections as suggested in section V; however, due to a software development oversight, the refraction correction on ϕ_t is ignored.

$\Delta U\left(\vec{\zeta}_t\right)$ is the geopotential, which is the second term in the denominator of (13),

$$\Delta U\left(\vec{\zeta}_t\right) = \mathrm{k}\ln 10 \sum_{l}^{\mathrm{NH^T}} \sum_{m}^{\mathrm{NP}^T} \left(f_{lm}^T \eta_m^T\left(\vec{\phi}_t\right) P_l\left(\vec{\zeta}_t\right)\right). \tag{88}$$

The reference geopotential is computed from the reference geometric height, which is related to the reference geopotential height, $Z_{\mathbf{refgeopot}}$, according to

$$R_{\text{ref}} = \frac{g_o^{\oplus}\left(\overset{\star}{R}_o^{\oplus}\right)^2}{\overset{\star}{g_o^{\oplus}} R_o^{\oplus} - g_o Z_{\text{refgeopot}}} - \overset{\star}{R}_o^{\oplus} + R^{\oplus}, \tag{89}$$

where $g_o^{\oplus}$ and $\overset{\star}{R}_o^{\oplus}$ are the gravitational acceleration and effective Earth radius computed at the Earth surface using (15) and (16) respectively. Remember that $Z_{\mathbf{refgeopot}}$ is horizontally (LOS angle) resolved (i.e. $Z_{\mathbf{refgeopot}} = \sum_m^{\mathrm{NH^T}} f_m^{\text{refgeopot}} \eta_m^T\left(\vec{\phi}_t\right)$).

Formulas for the derivatives of the scan residual with respect to the limb tangent pressure, temperature and reference geopotential are

$$\begin{aligned}
\frac{\mathrm{d}\vec{0}}{\mathrm{d}\vec{\zeta}_t} &= \mathrm{k}\ln 10 \sum_{l}^{\mathrm{NH^T}} \sum_{m}^{\mathrm{NP}^T} f_{lm}^T \eta_m^T\left(\vec{\phi}_t\right) \eta_l^T\left(\vec{\zeta}_t\right) / \left[g_o \mathcal{M}\left(\vec{\zeta}_t\right)\right] \\
&\quad + \frac{\mathrm{d}U_r}{\mathrm{d}\vec{R}_t} \frac{\vec{R}_t}{g_o \vec{\mathcal{N}}_t} \left[\left(\vec{\mathcal{N}}_t - 1\right)\left(\ln 10 + \frac{\mathrm{d}\ln \vec{T}_t}{\mathrm{d}\vec{\zeta}_t}\right)\right. \\
&\quad \left. + \frac{b' \vec{f}_t^{H_2O}}{\vec{T}_t 10^{\vec{\zeta}_t}}\left(\frac{\mathrm{d}\ln \vec{f}_t^{H_2O}}{\mathrm{d}\vec{\zeta}_t} - \frac{\mathrm{d}\ln \vec{T}_t}{\mathrm{d}\vec{\zeta}_t}\right)\right],
\end{aligned} \tag{90}$$

$$\begin{aligned}
\frac{\mathrm{d}\vec{0}}{\mathrm{d}f_{lm}^T} &= \frac{\mathrm{k}\ln 10}{g_o} \eta_m^T\left(\vec{\phi}_t\right) \eta_l^T\left(\vec{\zeta}_t\right) \\
&\quad + \frac{\mathrm{d}U_r}{\mathrm{d}\vec{R}_t} \frac{\vec{R}_t\left(\vec{\mathcal{N}}_t - 1 + \frac{b' \vec{f}_t^{H_2O}}{\vec{T}_t^2 10^{\vec{\zeta}_t}}\right)}{g_o \vec{T}_t \vec{\mathcal{N}}_t} \eta_l^T\left(\vec{\zeta}_t\right) \eta_m^T\left(\vec{\phi}_t\right),
\end{aligned} \tag{91}$$

$$\frac{\mathrm{d}\vec{0}}{\mathrm{d}f_m^{\text{refgeopot}}} = \frac{\mathrm{d}U_r}{\mathrm{d}R_{\text{ref}}} \eta_m^T\left(\vec{\phi}_t\right) \frac{R_{\text{ref}} - R^{\oplus} + \overset{\star}{R}^{\oplus}}{\overset{\star}{g_o^{\oplus}} \overset{\star}{R}^{\oplus} - g_o \sum_m^{\mathrm{NH^T}} f_m^{\text{refgeopot}} \eta_m^T\left(\vec{\phi}_t\right)}. \tag{92}$$

The $\frac{d\vec{0}}{d\vec{\zeta}_t}$ derivative is a sum of two contributions. The first term is a hydrostatic contribution and the second two terms are an index of refraction contribution. When $R_t < R^{\oplus}$, the second two terms are zero, that is it is not added to the first term. Although water vapor is included in $\mathcal{N}_t$, we have not worked out the derivatives for it because we do not use the scan model to retrieve H_2O.

XIV. Summary of Approximations and Accuracy

A forward model algorithm including its derivatives has been described. The model described here is the two dimensional extension of the forward model that was successfully implemented for UARS MLS [1], [30]. Table V provides a summary of the approximations that the forward model makes.

The table shows which section describes the approximation in detail, and if known how large its significance. The approximations have been cataloged by their purpose. A means an approximation that helps simplify a calculation or improves an interface to other data sets and users. D is an approximation that was chosen to be implemented at this time. N is a necessary approximation. It usually acts to reduce degrees of freedom in the state vector or reflects current state of knowledge. O is an approximation caused by an oversight in the software development.

Apart from the approximations listed above, the error in the forward model is a sum of an error that is proportional to the vertical and spectral gradients. Both of these are tunable. In the case of the vertical gradient sensitivity, the threshold for the adaptive integration, the order of the Gauss-Legendre integration and the selection of the PSIG impact the accuracy. The spectral error is dictated by the selection of the optimized grid. A simple estimate of the computational error is

$$\Delta\left(\overset{\bullet}{I}-I_{\rm bl}\right)_{\rm R,c} = \varepsilon_I \frac{{\rm d}\left(\overset{\bullet}{I}-I_{\rm bl}\right)_{\rm R,c}}{{\rm d}\zeta} \Big/ \left[\frac{{\rm d}\left(\overset{\bullet}{I}-I_{\rm bl}\right)_{\rm R,c}}{{\rm d}\zeta}\right]_{\rm max} + {\rm MIN}\left(\varepsilon_I, I/10.0\right) \tag{93}$$

where ε_I is the target maximum error for the vertical and spectral gradient errors, ${\rm d}\left(\overset{\bullet}{I}-I_{\rm bl}\right)_{\rm R,c}/{\rm d}\zeta$ is the vertical radiance gradient, $\left[{\rm d}\left(\overset{\bullet}{I}-I_{\rm bl}\right)_{\rm R,c}/{\rm d}\zeta\right]_{\rm max}$ is the maximum vertical gradient, and I is the maximum signal strength of a given absorber as estimated with (26). The first term right of the $=$ is an estimate of the error proportional to the vertical gradient which is the ratio of the actual vertical gradient to the maximum vertical gradient times the target maximum error which is usually 0.2 K for our calculations. The second term is the spectral component which is the minimum of the target maximum error or the ratio of the maximum signal strength to 10 K. When selecting frequency grid points in the optimized frequency grids file, it is important that all lines are at least ~ 10 K strong so as to avoid large signal descrepancies between weak and strong lines. Therefore we inflate the concentrations of weak species such that they give a ~ 10 K signal to insure that their lines are accurately gridded in the presence of stronger lines when producing an optimized frequency grids file. With a target maximum error of 0.2 K, this insures that this error term should not exceed 10% of the weak line signal strength.

It is convenient to express radiance errors in terms of non-spectrally and spectrally varying components because, the non-spectrally component is absorbed in the baseline retrieval and only the spectrally varying part contaminates

TABLE V

SUMMARY OF FORWARD MODEL APPROXIMATIONS OR UNCERTAINTIES

Approximation or uncertainty	Section	Purpose
Representation basis functions.	IV	A
PSIG driven quadrature.	V	A
Hydrostatic balance.	V	N
Co-alignment of orbital and LOSF planes.	V	N
Equivalent circular Earth.	V	A
Neglect refraction in LOS ϕ_t	V	O
Neglect refraction on path ϕ	V	A
Minimum ζ_t and h_t are coincident.	V	A
Summed line $\times$ line Van Vleck Weiskoff Voigt lineshape.	VI	D
Estimated values for some spectroscopic parameters.	VI	N
Line selection thresholds	VI	N
Refractive path length scaling	VII	A
LOS rays reflect off the reference geopotential surface ignoring surface topography.	VII	D
Separate frequency and spatial integrations	VIII	A
Neglect 2nd IF image sideband in DACS spectral integration	VIII	A
Neglect radiance cross track gradients in FOV	IX	N
Antenna pattern elevation axis is in the LOSF plane	IX	A
Antenna pattern is scan independent	IX	A
FFT approximation to convolution	IX	A
Empirical geocentric height formula	IX	A
Neglect difference between scanned ϕ_t and instantaneously observed FOV ϕ_t	IX	A
Neglect refraction in radiance T derivative	IX	A
Neglect scan motion	XI	D

A = advantageous, D = discretionary, N = necessary, O = oversight

the concentration retrieval. In general, forward model errors do not conveniently partition themselves this way except for one situation. If the molecular line component is optically thin and the continuum is mostly responsible for the transition from optically thin to opaque then the first term right of = in (93) is the non spectrally varying error and the second term is spectrally varying error. Thus for BrO which has a signal strength of 0.1 K, the spectral error would be 0.002 K. For strong, non optically thin lines, both terms right of the = in (93) are spectrally varying because the vertical radiance growth gradient is spectrally varying and therefore the spectrally varying component is likely to be 0.4 K.

XV. Level 2 Processing Coefficients File

The Level 2 Processing Coefficients (L2PC) file is a file that contains the first order Taylor series coefficients describing (1). Weak signals, especially if the background continuum absorption is weak, can be very well modeled with a first order Taylor series given by

$$\overset{\bullet}{I} - I_{\rm bl} = \overset{\star}{I} + \sum_j \frac{{\rm d}\overset{\star}{I}}{{\rm d}x_j}\left(x_j - \overset{\star}{x}_j\right), \tag{94}$$

where $\overset{\star}{I}$ is the calculated radiance (sections III–XI) at state vector element $\overset{\star}{x}_j$. The state vector contains ζ_t, constituent and temperature profiles, $\mathbf{f}$. In future versions, ϕ_t, radiometer offset angles, and spectroscopic parameters (position and lineshape), will be added to the state vector. Currently, the L2PC calculation includes effects and sensitivities to profiles from 5 adjacent LOS angles with the LOS tangent angle co-aligned with the center basis ϕ. The zig-zag nature of the scan in ϕ_t is ignored at present. Radiances are computed for several tangent pressures. Estimated model radiances are evaluated using (94) at all the tangent pressures in the L2PC $\overset{\star}{\mathbf{x}}$. The resulting radiances are interpolated to the measured tangent pressures with cubic splines. Derivatives for the retrieval are interpolated to the measured tangent pressures with linear interpolation. Tables of $\overset{\star}{x}_j$, $\overset{\star}{I}$, and $\frac{{\rm d}\overset{\star}{I}}{{\rm d}x_j}$ are stored in files for each radiometer band. A file for each month of the year is created and in each file, radiances and derivatives are computed for 15° latitude bins. The corresponding $\overset{\star}{x}_j$ for each 15° latitude bin is a climatological zonal mean. For the strongly emitting diurnal species OH, the L2PC file includes a diurnal $\overset{\star}{\mathbf{f}}^{\rm OH}$ as part of the $\overset{\star}{x}_j$'s. Polarized L2PC files [6] are calculated for a single climatology for an array of magnetic field strengths and orientations. The accuracy of the L2PC file may be extended by including the second order derivatives in a future upgrade. Computing the second order derivative is a straightforward extension of (45) and was developed and demonstrated for UARS MLS but not implemented in production.

XVI. Examples of Measured and Fitted Spectra

Fig. 12 shows an example of signals measured by EOS MLS. All good channels in all bands that are normally active during science operations are shown. The radiances are a daily average of all good radiances for minor frames (MIF) 30, 40, 50, 60, 70, 80, 90, 100, 110, which point to 11.0, 14.7, 18.5, 22.2, 26.1, 35.9, 45.5, 55.1, and 64.7 km, respectively. Each minor frame is a $\frac{1}{6}$ second integration and there are 3495 radiance profiles per day, each consisting of 125 MIFs. Each measured EOS MLS channel is shown as a colored-by-MIF + where the

width of the horizontal bar is the channel bandwidth and the height of the vertical bar is the precision reduced by the square root of the number of samples averaged, in this case 3495. To emphasize spectral continuity, a line joining the channels marked with bullets has been overlaid on the panels except the DACS channels and the R1B wide band filters or where there are breaks between good and bad channels as marked by Level 1. The excessive averaging makes the precision bar small and hard to see for most channels. A few channels are omitted that are not performing as well as the rest have been flagged "bad" by Level 1 processing [9]. An example are two of the four wide band channels in R1A. The edge channels of the digital autocorrelator spectrometer (DACS) are extremely noisy because a prefilter to the DACS limits the signal to 10 MHz [9]. To keep the figure clean, only the useful DACS channels are shown. The spectral regions of R4 targeted on the weak signal species, BrO, HO_2, and HOCl are shown in the lower half of Fig. 14. The weak diurnal BrO lines are overshadowed by neighboring strong lines. It can only be seen in the radiances by taking a day minus night difference.

Under the spectra, the goodness of the radiance fit is shown (observed minus calculated). The calculated radiances use the forward model described here with the retrieved Level 2 state vector as input [4]. The displayed difference is a daily average of all differences from good retrievals. All channels used by the retrieval are shown and marked with a color coded + (channel bandwidth and precision). The retrieval uses a subset of good measured radiances. There are many reasons for this. First, where channels overlap, a judicious choice of channels (usually those with narrowest bandwidth) is selected to minimize the overlap. The noise in overlapping channels is highly correlated because they observe the same photons. The Level 2 retrieval currently requires uncorrelated measurements and therefore including overlapping channels would compromise the error calculation. Secondly, due to computer processing limitations, some non-linear channels that are time consuming to evaluate are omitted. These channels require too many line-by-line and frequency gridded radiative transfer calculations. Thirdly, some channels that are modeled with L2PC files are omitted when their radiances become non linear. Lastly, some channels producing inexplicably large differences are omitted [4].

Under the difference spectrum plot are the molecular line positions with a strength estimate. The lines are color coded by molecule and the strength is a simple estimate based on a representative high concentration for the molecule. It is not the actual concentration retrieved by level 2, therefore there should not necessarily be a good match between the stick spectrum magnitude and the measured. A given molecule includes all its isotopes and excited vibrational states listed in table I. For example ClO includes ^{35}ClO, ^{35}ClO-ν_1, ^{37}ClO, and ^{37}ClO-ν_1. The stick spectra show which molecules from table I that were found having sufficient intensity to be considered. The radiometers have different acceptance criteria accounting for the different line densities plotted. Radiometers R1A, R1B R3, R5H, and R5V, which are dominated by strong molecular signals, had a higher acceptance threshold [3].

Although the measured minus calculated differences are small in most cases, there are a few exceptions. The R1A DACS channels show large differences, which may be caused by errors in the thermospheric temperature and O_2 concentration used in the forward model calculation. At present these are not retrieved at thermospheric altitudes. The R1A band 1 filter banks also show a pressure shift-like residual artifact suggesting that O_2 has a non-zero pressure shift. It is noted here that the shift seen is about the same magnitude but opposite in sign to that published

by [31]. Laboratory measurements of O_2 conducted at JPL observe no shift [B. Drouin, personal communication, 2004]. The differences between observations and calculations are small for R2. There are some minor lineshape artifacts in the vicinity of the H_2O, N_2O, HNO_3, and O_3 lines. Level 2 (v01.51) is currently not using the band 23 DACS in its processing because of processing time constraints. The R3 radiometer which observes some very strong O_3 lines tends to have larger differences with some channels near the wings of strong ozone lines being omitted becuase those channels are too difficult to calculate accurately and quickly enough for level 2 processing. R5V and R5H, the terahertz radiometers measuring orthogonal polarizations, show some line shape artifacts in the vicinity of the OH line.

XVII. Interpreting Basis Coefficients

One feature of the EOS MLS forward model that differs from that normally used is its direct use of basis coefficients with the representation basis functions embedded into the algorithm. The motivation for this approach was to simplify the interface to the retrieval algorithm and to minimize the number of derivative calculations. However, it should be appreciated that the state vector representation is an approximation to an infinitely resolved profile. Therefore some care is needed when converting a higher-than-EOS MLS resolution profile into retrieval coefficient values.

It is customary to use the averaging kernel, $\mathbf{A}$, to smooth a high resolution profile to the resolution of the measurement system according to [32]

$$\hat{\mathsf{f}} = \mathbf{a} + (\mathsf{f} - \mathbf{a})\,\mathbf{A}, \tag{95}$$

where $\hat{\mathsf{f}}$ are the retrieved profiles, f are the true atmospheric profiles, and $\mathbf{a}$ are the a priori profiles, all sampled toward the limit of infinite resolution. A practical problem with (95) is that the retrieval coefficients are sampled much more coarsely than f and often more coarsely than in situ measurements or model calculations. Properly comparing the EOS MLS retrieval with another dataset requires recalculating the retrieval where the EOS MLS profile sampling matches the correlative dataset. The main defect of (95) is that users do not have access to any of the quantities except f.

Degrading (95) to the sampling resolution of EOS MLS gives

$$\hat{\mathbf{f}} = \overline{\mathbf{a}} + \left(\overline{\mathbf{f}} - \overline{\mathbf{a}}\right)\overline{\mathbf{A}}, \tag{96}$$

where $\hat{\mathbf{f}}$ are the retrieved coefficients (i.e. f^k_{lmn} of (3) or 4), $\overline{\mathbf{f}}$ is the forward model representation of the true atmosphere, $\overline{\mathbf{a}}$ are the a priori profile coefficients, and $\overline{\mathbf{A}}$ is the averaging kernel at the EOS MLS sampling resolution, the square matrix calculated by [4]. The finite profile sampling introduces a modeling error that is not captured by the averaging kernel. The interpretation of $\overline{\mathbf{f}}$ is developed here.

The forward model is represented by

$$\overset{\bullet}{I} - I_{\mathrm{bl}} = \overset{\star}{I} + \left(\mathsf{f} - \overset{\star}{\mathbf{f}}\,\eta\right)\mathbf{H}, \tag{97}$$

where $\mathbf{H} = \frac{\mathrm{d}\overset{\star}{I}}{\mathrm{d}\mathsf{f}}$ is a Jacobian of radiance sensitivities to profile values in the limit of infinite resolution, the same as the true profile f, η is a matrix containing the profile coefficient weights computed by (5)–8. The retrieval Jacobian

is $\overset{\star}{K} = \mathbf{H}\eta$. It is required that the forward model responds linearly to fine structure fluctuations of f that are not captured by the profile basis resolution, $\bar{\mathbf{f}}\eta$. If the forward model has no errors except those introduced by the limited sampling of the profiles, the atmospheric radiances relate to modeled radiances according to

true atmospheric radiances	model radiances
$\left(\mathsf{f} - \overset{\star}{\mathbf{f}}\eta\right)\mathbf{H}$	$\left(\bar{\mathbf{f}} - \overset{\star}{\mathbf{f}}\right)\eta\mathbf{H}$

The $\overset{\star}{\mathbf{f}}\eta\mathbf{H}$ is common to both sides and can be dropped out

$\mathsf{f}\mathbf{H}$	$\bar{\mathbf{f}}\eta\mathbf{H}$

This implies that

$$\mathsf{f} \equiv \bar{\mathbf{f}}\eta. \tag{98}$$

Equation (98) is not an equivalence because the left side has more degrees of freedom than the right. If $\left(\mathbf{H}\mathbf{H}^t\right)^{-1}$ is invertible it is easy to show that

$$\bar{\mathbf{f}} = \mathsf{f}\eta^{\mathrm{t}}\left(\eta\eta^{\mathrm{t}}\right)^{-1} \tag{99}$$

minimizes the square of the radiance differences between the model and true atmospheric radiances. We call $\eta^{\mathrm{t}}\left(\eta\eta^{\mathrm{t}}\right)^{-1}$, the forward model smoothing operator. Equation (99) would be the retrieved profile for an error-less measurement. In practice, $\left(\mathbf{H}\mathbf{H}^t\right)^{-1}$ may be singular because the measurement system is not sensitive at all altitudes, therefore (99) would apply to a subset of the profile coefficients.

Substituting eq. 99 into eq. 96 gives

$$\hat{\mathbf{f}} = \bar{\mathbf{a}} + \left[\mathsf{f}\eta^{\mathrm{t}}\left(\eta\eta^{\mathrm{t}}\right)^{-1} - \bar{\mathbf{a}}\right]\overline{\mathbf{A}}, \tag{100}$$

which is the proper way to convert high resolution data into retrieval coefficients. Since all the elements in an averaging kernel row tend toward zero for a coefficient not observable by the measurement system, we can disregard the requirement that $\left(\mathbf{H}\mathbf{H}^t\right)^{-1}$ is non singular when applied to (100).

Equation (100) offers some significant advantages over (95). For most EOS MLS products over their recommended altitude ranges [33], and if the retrieved quantity is not influenced by a priori information, (100) is well approximated by (99). The EOS MLS standard level 2 geophysical products (L2GP) file contains all the information needed to compute the forward model smoothing operator. The breakpoint values, ζ_l^k and ϕ_m^k are in the L2GP file and η is evaluated with eqs. 5–8. If one wishes to use (100), the averaging kernel is that produced by [4] with representative examples published in [34].

REFERENCES

[1] J. W. Waters, W. G. Read, L. Froidevaux, R. Jarnot, R. E. Cofield, D. A. Flower, G. K. Lau, H. M. Pickett, M. L. Santee, D. L. Wu, M. A. Boyles, J. R. Burke, R. R. Lay, M. S. Loo, N. J. Livesey, T. A. Lungu, G. L. Manney, L. L. Nakamura, V. S. Perun, B. P. Ridenoure, Z. Shippony, P. H. Siegel, R. P. Thurstans, R. S. Harwood, H. C. Pumphrey, and M. J. Filipiak, "The UARS and EOS Microwave Limb Sounder experiments," *J. Atmos. Sci.*, vol. 56, pp. 194–218, 1999.

[2] J. W. Waters *et al.*, "The EOS MLS experiment overview," 2005, IEEE Transactions on Geosciences and Remote Sensing: The EOS Aura Mission.

[3] W. G. Read, Z. Shippony, and W. V. Snyder, "EOS MLS forward model algorithm theoretical basis document," Jet Propul. Lab., Pasadena, Calif., Tech. Rep. JPL D-18130, http://swdev.jpl.nasa.gov/doc.html#ATBDs, January 16 2003.

[4] N. J. Livesey and W. V. Snyder, "Retrieval algorithms for the EOS Microwave Limb Sounder (MLS) instrument," 2005, IEEE Transactions on Geosciences and Remote Sensing: The EOS Aura Mission.

[5] D. L. Wu *et al.*, "Cloud ice measurements, forward model and retrievals," 2005, IEEE Transactions on Geosciences and Remote Sensing: The EOS Aura Mission.

[6] M. J. Schwartz *et al.*, "Polarized forward model," 2005, IEEE Transactions on Geosciences and Remote Sensing: The EOS Aura Mission.

[7] N. J. Livesey, "EOS MLS Retrieval Processes Algorithm Theoretical Basis," Jet Propulsion Laboratory, Mail Stop 183–701, 4800 Oak Grove Drive, Pasadena, Ca., 91109-8099, Level 2 ATBD, http://swdev.jpl.nasa.gov/doc.html#ATBDs JPL D-16159, 21 June 2004, version 1.3.

[8] B. Schwartzschild, "COBE satellite finds no hint of excess in the cosmic microwave spectrum," *Physics Today*, pp. 17–20, March 1990.

[9] R. F. Jarnot *et al.*, "Ghz radiometric calibration and performance," 2005, IEEE Transactions on Geosciences and Remote Sensing: The EOS Aura Mission.

[10] R. E. Cofield *et al.*, "Ghz optics design and performance," 2005, IEEE Transactions on Geosciences and Remote Sensing: The EOS Aura Mission.

[11] H. M. Pickett *et al.*, "Thz calibration and performance," 2005, IEEE Transactions on Geosciences and Remote Sensing: The EOS Aura Mission.

[12] C. C. Tscherning, Ed., *The Geodesist's Handbook*. Bureau Central De L'Association Internatiale De Géodésie, 1984, vol. 58, no. 3.

[13] R. J. List, "Smithsonian meteorological tables," Smithson. Inst., Washington, D. C., Smithson. Misc. Collect. 114, 1951.

[14] H. M. Pickett, R. L. Poynter, E. A. Cohen, M. L. Delitsky, J. C. Pearson, and H. S. P. Muller, "Submillimeter, millimeter, and microwave spectral line catalog," *J. Quant. Spectrosc. Radiat. Transfer*, vol. 60, no. 5, pp. 883–890, 1998, see http://spec.jpl.nasa.gov/.

[15] L. S. Rothman, C. P. Rinsland, A. Goldman, S. T. Massie, D. P. Edwards, J. M. Flaud, A. Perrin, C. Camy-Peyret, V. Dana, J. Y. Mandin, J. Schroeder, A. McCann, R. R. Gamache, R. B. Wattson, K. Yoshino, K. V. Chance, K. W. Jucks, L. R. Brown, V. Nemtchinov, and P. Varinasi, "The HITRAN molecular spectroscopic database and HAWKS (HITRAN atmospheric workstation): 1996 edition," *J. Quant. Spectrosc. Radiat. Transfer*, vol. 60, p. 665, 1998, see http://www.harvard.edu/HITRAN/.

[16] H. J. Liebe, G. A. Hufford, and M. G. Cotton, "Propagation modeling of moist air and suspended water/ice particles at frequencies below 1000 Ghz," in *52nd Specialists' Meeting of the Electromagnetic Wave Propagation Panel*. Palma De Mallorca, Spain: Adv. Group for Aerosp. Res. and Dev., May 17–21 1993.

[17] P. Kroopnick and H. Craig, "Atmospheric oxygen: Isotopic composition and solubility fractionation," *Science*, vol. 175, pp. 54–55, 1972.

[18] J. W. Waters, *Microwave Limb Sounding*. John Wiley & Sons, 1993, ch. 8, pp. 383–496.

[19] M. Abramowitz and I. A. Stegun, *Handbook of Mathematical Functions*. New York: Dover, 1965, national Bureau of Standards Applied Mathematics Series 55 (U.S. Government Printing Office, Washington, D.C., 1964).

[20] Z. Shippony and W. G. Read, "A highly accurate Voigt function algorithm," *J. Quant. Spectrosc. Radiat. Transfer*, vol. 50, pp. 635–646, 1993.

[21] H. M. Pickett, "Effects of velocity averaging on the shapes of absorption lines." *J. Chem. Physics*, vol. 73, pp. 6090–6094, 1980.

[22] D. L. Wu and J. H. Jiang, "EOS MLS algorithm theoretical basis for cloud measurements," Jet Propul. Lab., Pasadena, Calif., Tech. Rep. JPL D-19299, http://swdev.jpl.nasa.gov/doc.html#ATBDs, 4 June 2004, version 1.0.

[23] J. R. Pardo, E. Serabyn, and J. Cernicharo, "Submillimeter atmospheric transmission measurements on Mauna Kea during extremely dry El Niño conditions: Implications for broadband opacity contributions," *J. Quant. Spectrosc. Radiat. Transfer*, vol. 68, pp. 419–433, 2001.

[24] C. R. Webster and A. J. Heymsfield, "Water isotope ratios D/H, $^{18}O/^{16}O$, $^{17}O/^{16}O$ in and out of clouds reveal dehydration pathways and the origin of cirrus," *Science*, vol. 302, pp. 1742–1745, 2003.

[25] H. C. Pumphrey, "Validation of a new prototype water vapor retrieval for the UARS Microwave Limb Sounder," *J. Geophys. Res.*, vol. 104, no. D8, pp. 9399–9412, 1999.

[26] J. D. Kraus, *Radio Astronomy*. New York: McGraw-Hill, 1966.

[27] M. Born and E. Wolf, *Principles of Optics*. New York: The MacMillan Company, 1964.

[28] M. J. Schwartz, W. V. Snyder, and W. G. Read, "EOS MLS mesosphere-specific forward model algorithm theoretical basis document," Jet Propulsion Laboratory, Mail Stop 183–701, 4800 Oak Grove Drive, Pasadena, Ca., 91109-8099, Mesosphere Specific ATBD JPL D-28534, http://swdev.jpl.nasa.gov/doc.html#ATBDs, 4 June 2004, version 1.0.

[29] J. W. Waters and L. Froidevaux, "An Overview of the EOS MLS Experiment," Jet Propulsion Laboratory, Mail Stop 183–701, 4800 Oak Grove Drive, Pasadena, Ca., 91109-8099, Overview ATBD, http://swdev.jpl.nasa.gov/doc.html#ATBDs JPL D-15745, 2 April 2004, version 2.0.

[30] N. J. Livesey, W. G. Read, L. Froidevaux, J. W. Waters, H. C. Pumphrey, D. L. Wu, M. L. Santee, Z. Shippony, and R. F. Jarnot, "The UARS Microwave Limb Sounder version 5 dataset: Theory, characterization and validation," *J. Geophys. Res.*, vol. 108, no. D13, pp. 4378, doi:10.1029/2002JD002 273, 2003.

[31] M. Y. Tretyakov, V. V. Parshin, V. N. Shanin, S. E. Myasnikova, M. A. Koshelev, and A. F. Krupnov, "Real atmosphere laboratory mesurements of the 118 ghz oxygen line: Shape, shift and broadening of the line," *J. Mol. Spectrosc.*, vol. 208, no. 1, pp. 110–112, 2001.

[32] C. D. Rodgers, "Characterization and error analysis of profiles retrieved from remote sounding measurements," *J. Geophys. Res.*, vol. 95, no. D5, pp. 5587–5595, 1990.

[33] N. J. Livesey, "Data quality document for the EOS MLS version 1.5 level 2 dataset," Jet Propulsion Laboratory, Tech. Rep. Tech. Rep., 2005.

[34] M. Filipiak, N. J. Livesey, and W. G. Read, "EOS MLS Retrieved Geophysical Parameter Precision Estimates," University of Edinburgh, Department of Meteorology, Edinburgh, UK, Algorithm Theoretical Basis Document (ATBD) JPL D–16160, http://swdev.jpl.nasa.gov/doc.html#ATBDs, 28 June 2004, version 1.4.

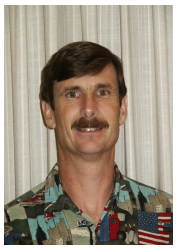

William G. Read was born in Rockville Centre, New York, on April 14, 1957. He received the A. B. degree from Occidental College, Los Angeles, CA., and the Ph. D. degree in physical chemistry from the University of Illinois, Urbana, IL in 1979 and 1983, respectively.

From 1983 to 1985 he held an NRC-NASA Resident Research Associateship award at the Jet Propulsion Laboratory, Pasadena. Currently he is a principal research scientist and a co-investigator for the Earth Observing System Microwave Limb Sounder at the Jet Propulsion Laboratory, California Institute of Technology, Pasadena, CA.

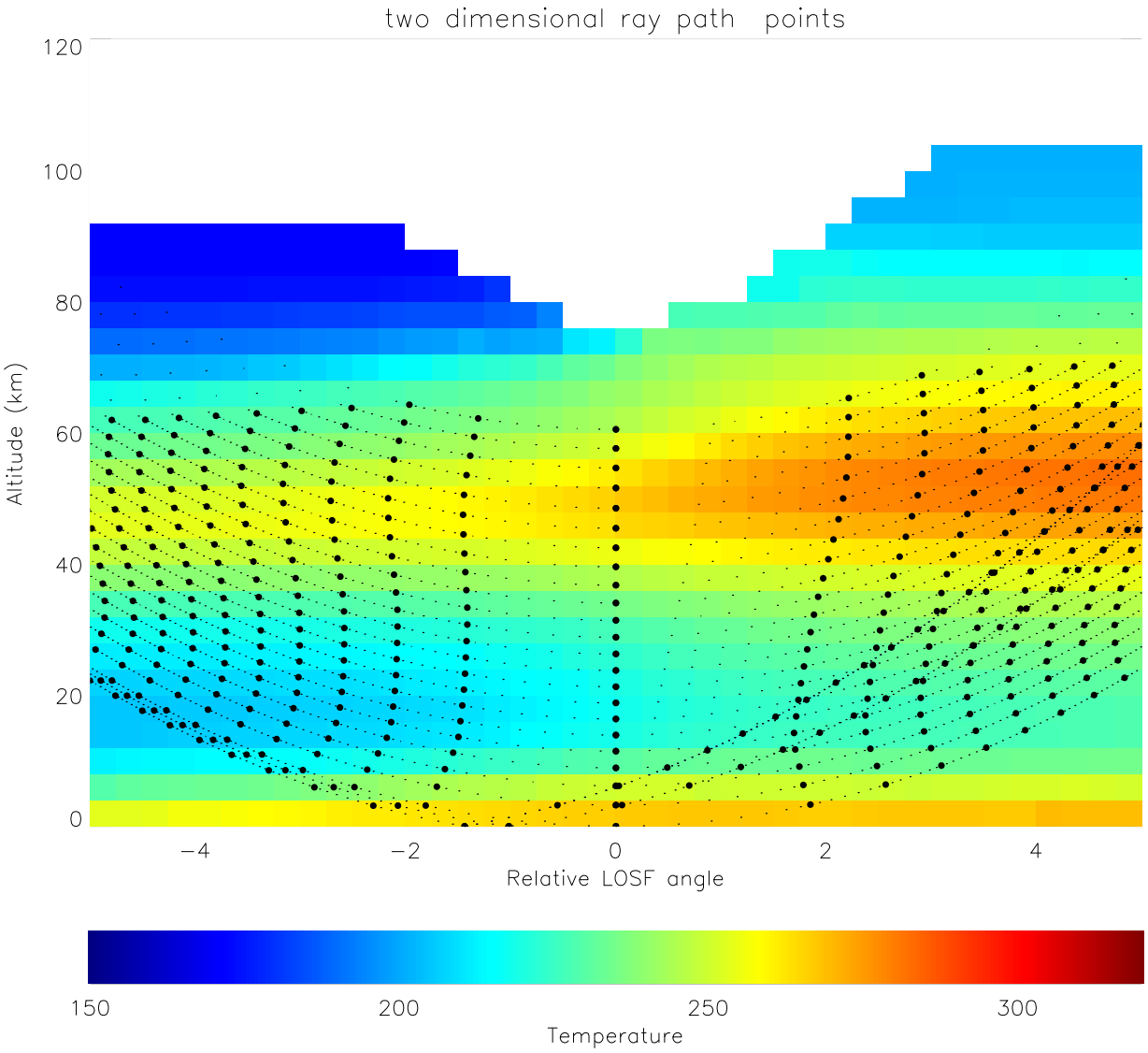

Fig. 8. An example of LOS ray ϕ and h calculated for the standard atmosphere with a 3.33 K/° horizontal gradient. The PSIG points are a grid consisting of 6 levels per decade change in log pressure (2.7 km per point) with two tangents reflecting off the Earth surface. The h and ϕ values for 27 tangent rays are overlaid on the temperature field. The PSIG points are large bullets and the augmented PSIG (8 point GL) are the small dots.

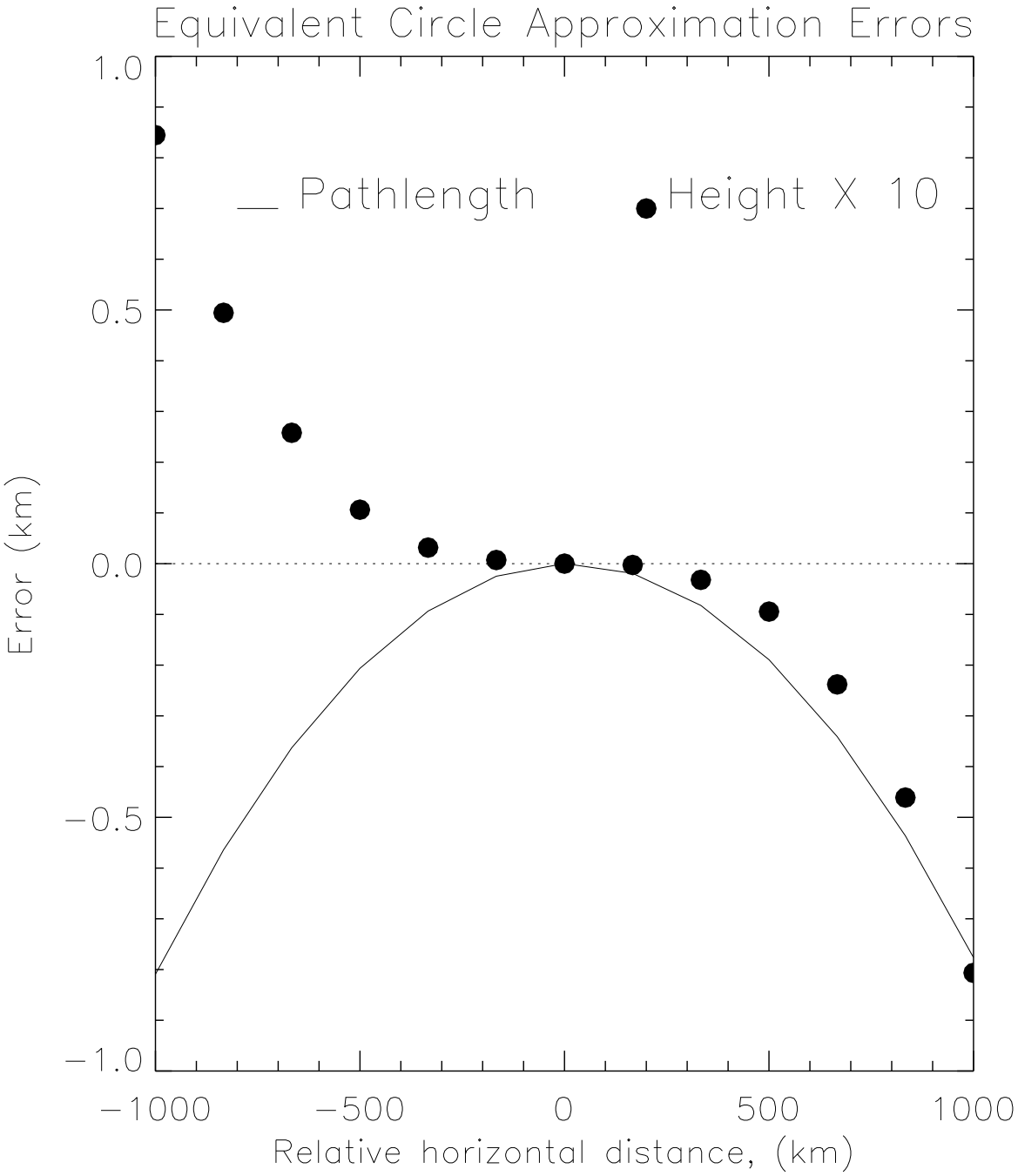

Fig. 9. Difference of h and s computed for ellipse and equivalent circular Earth representations at 45.0°.

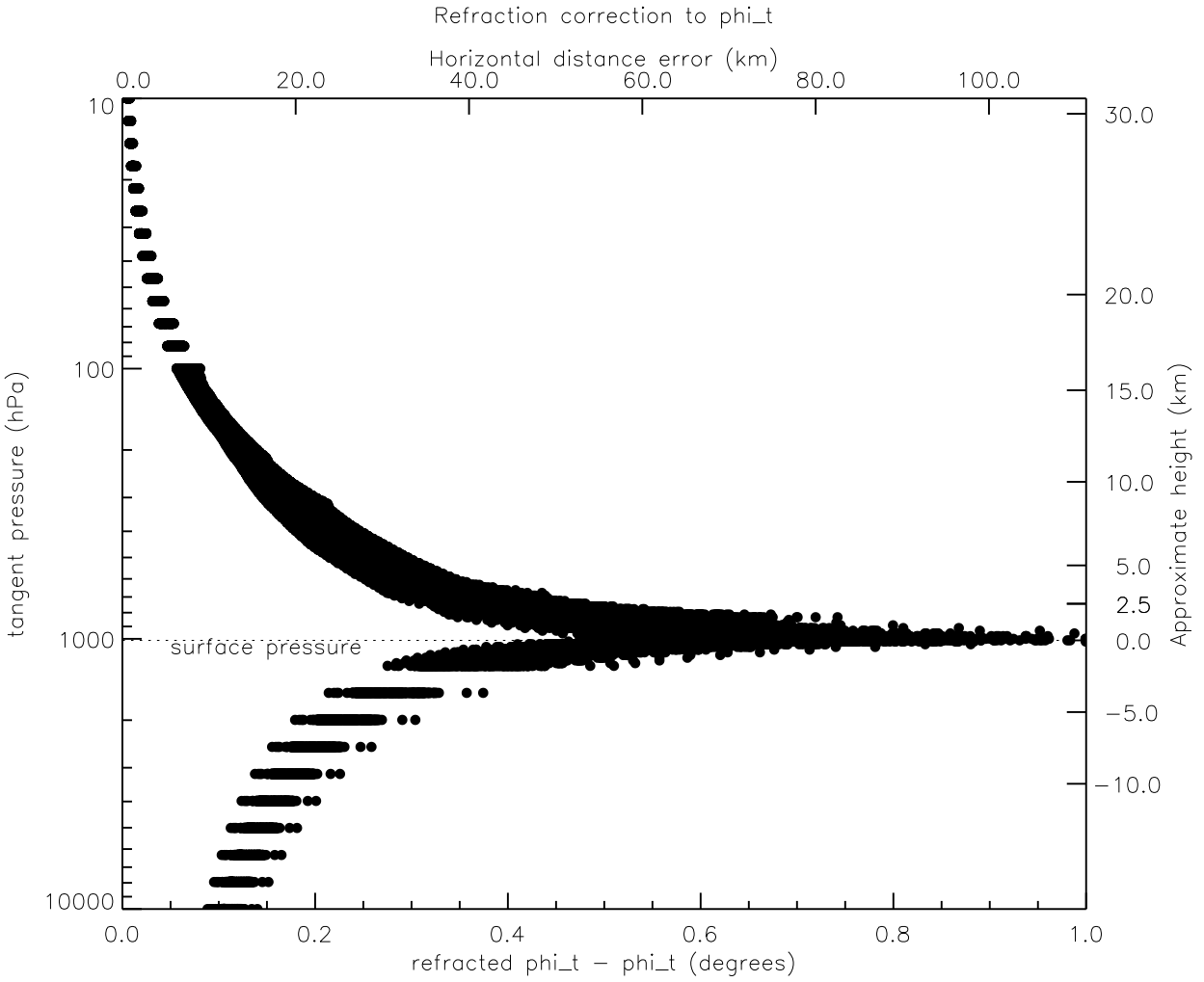

Fig. 10. Computed difference between refracted ϕ_t and unrefracted ϕ_t for several simulated February profiles over 2 Aura orbits and several tangent pressures (and heights)

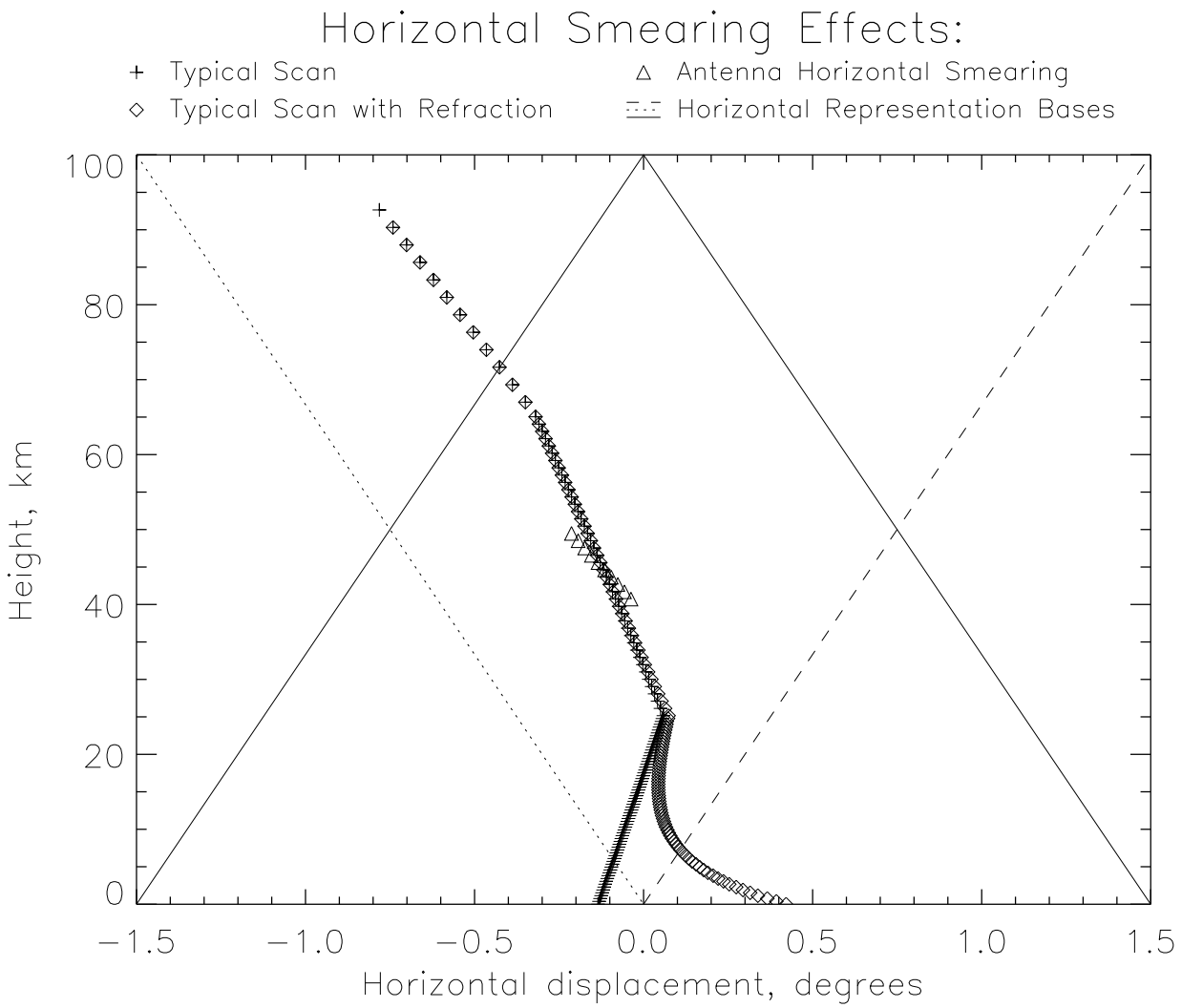

Fig. 11. The horizontal variations expected due to scanning with and without refraction and antenna averaging. These are shown in comparison with the EOS MLS LOS angle basis function.

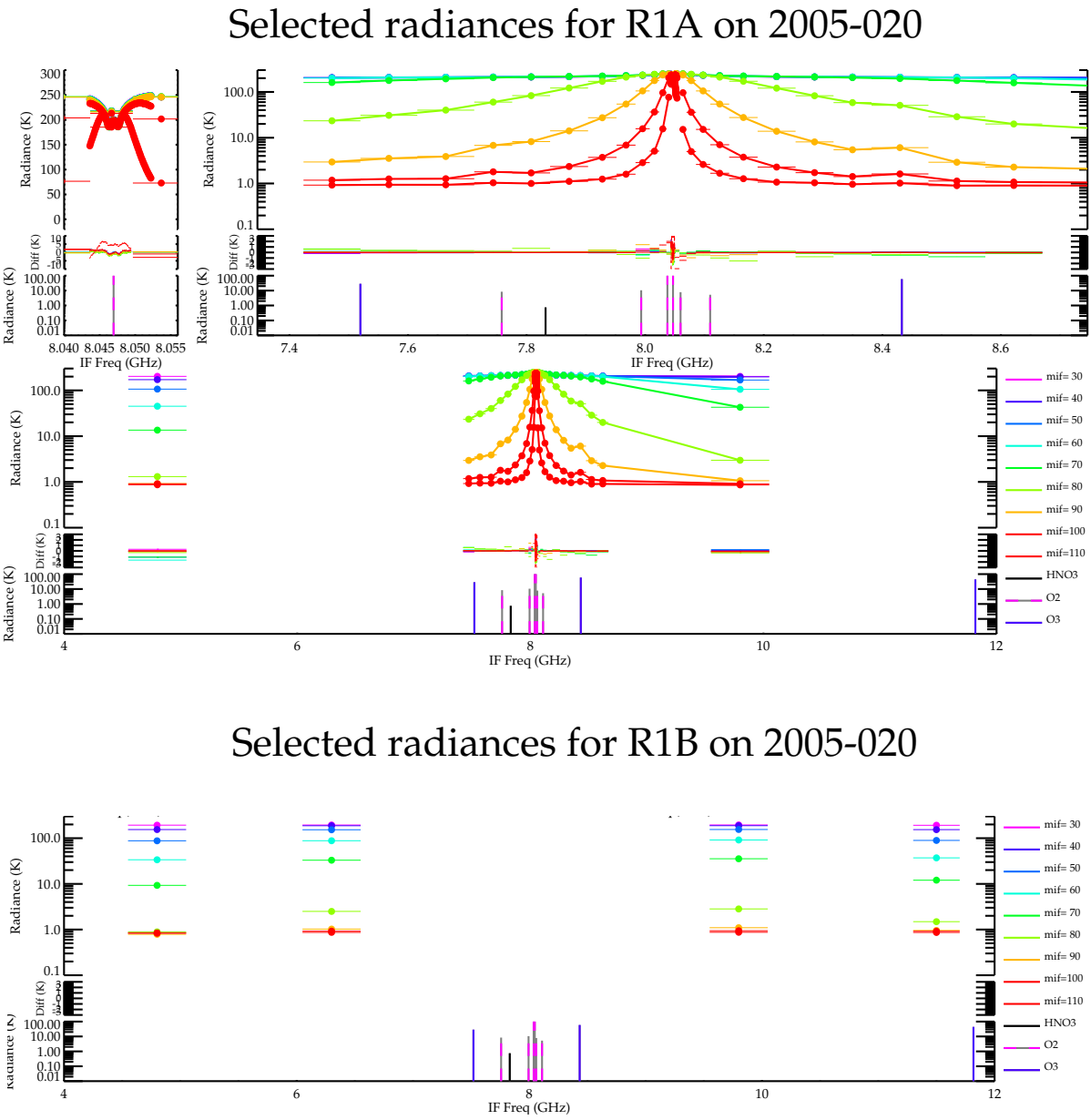

Fig. 12. Measured, residual, and molecular stick spectra for EOS MLS radiometers R1A, top and R1B, bottom. These radiometers measure orthogonal polarizations of the same spectral coverage. The local oscillator for these radiometers is 126000 MHz. Only the lower sideband is observed. The radiances are a daily average of all good radiances on 20 Jan. 2005 for 9 selected MIFs (color). Underneath show the daily averaged goodness of fitted radiances (observed minus calculated). Under that is a stick spectrum showing the identity (color), position and approximate strength of molecular signals in these radiometers. Multiple panels having different frequency ranges exist to emphasize the spectral coverage and resolution of EOS MLS. The R1B radiometer is redundant to R1A and its associated filter band and DACS are normally switched to other radiometers, hence omitted from this figure. See text for further discussion.

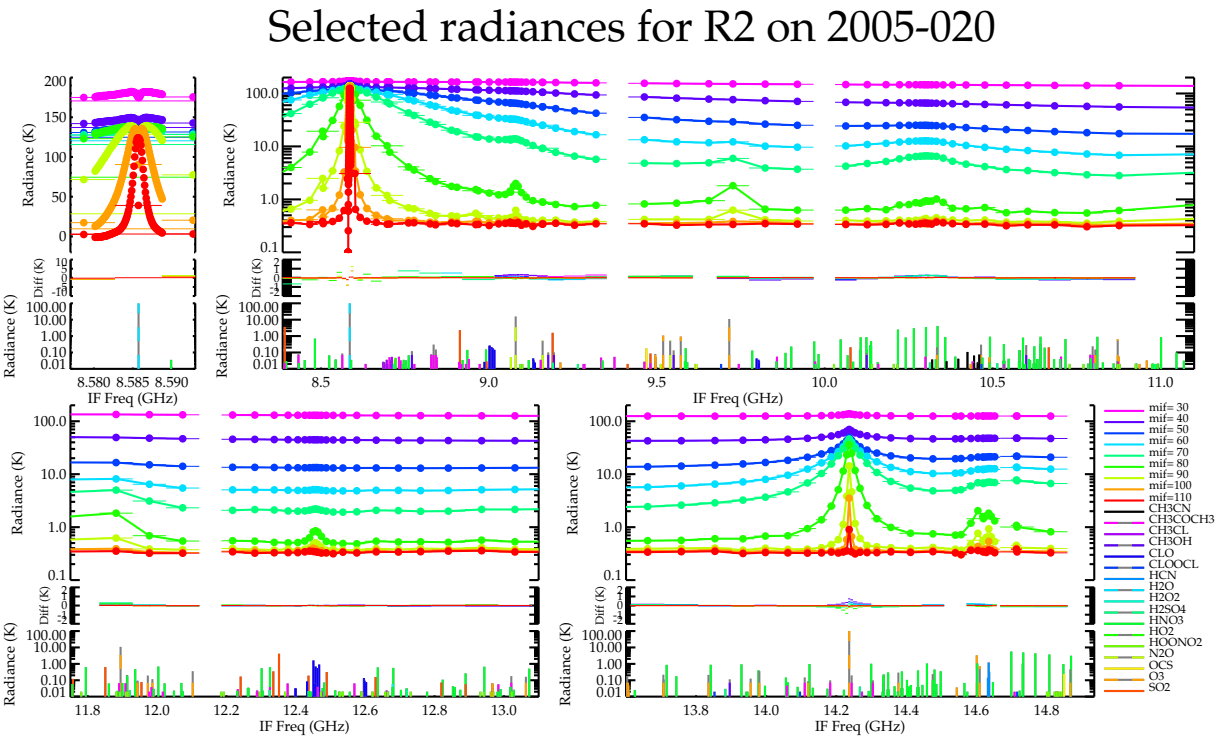

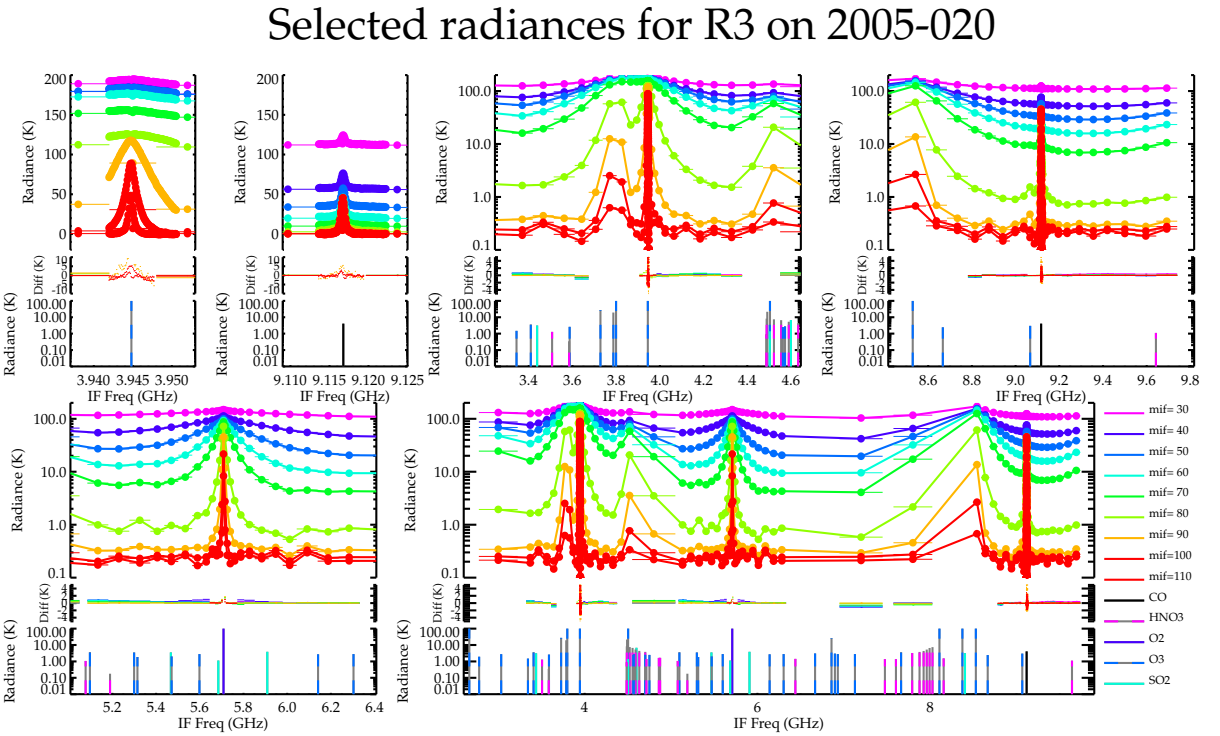

Fig. 13. Same as Fig. 12 but for EOS MLS radiometers R2 and R3. The local oscillator frequencies are 191900 MHz and 239660 MHz respectively. These are double sideband radiometers. See text for further discussion.

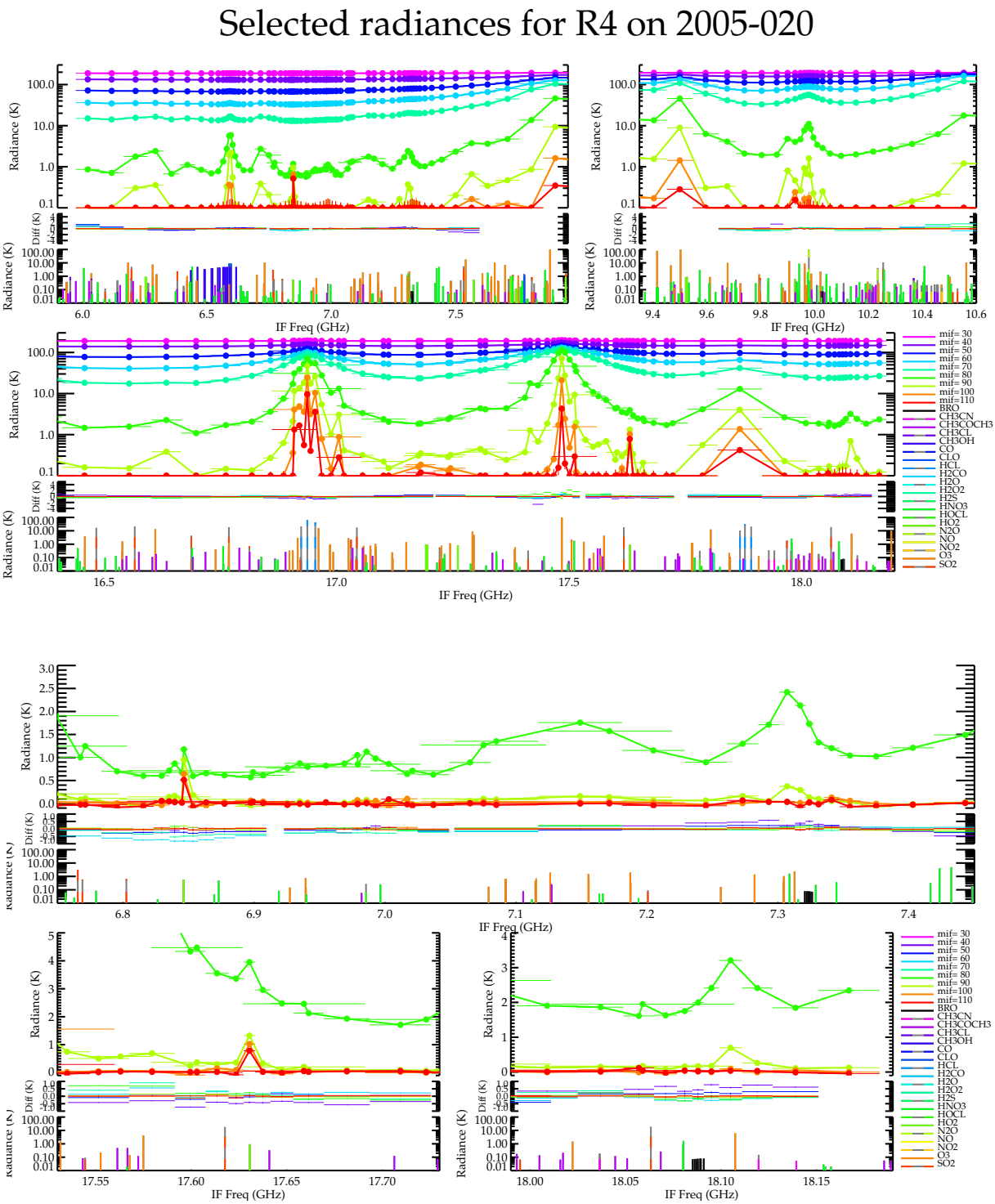

Fig. 14. Same as Fig. 12 but for EOS MLS R4 radiometer. The local oscillator frequency is 642870 MHz. R4 is a double sideband radiometer. See text for further discussion.

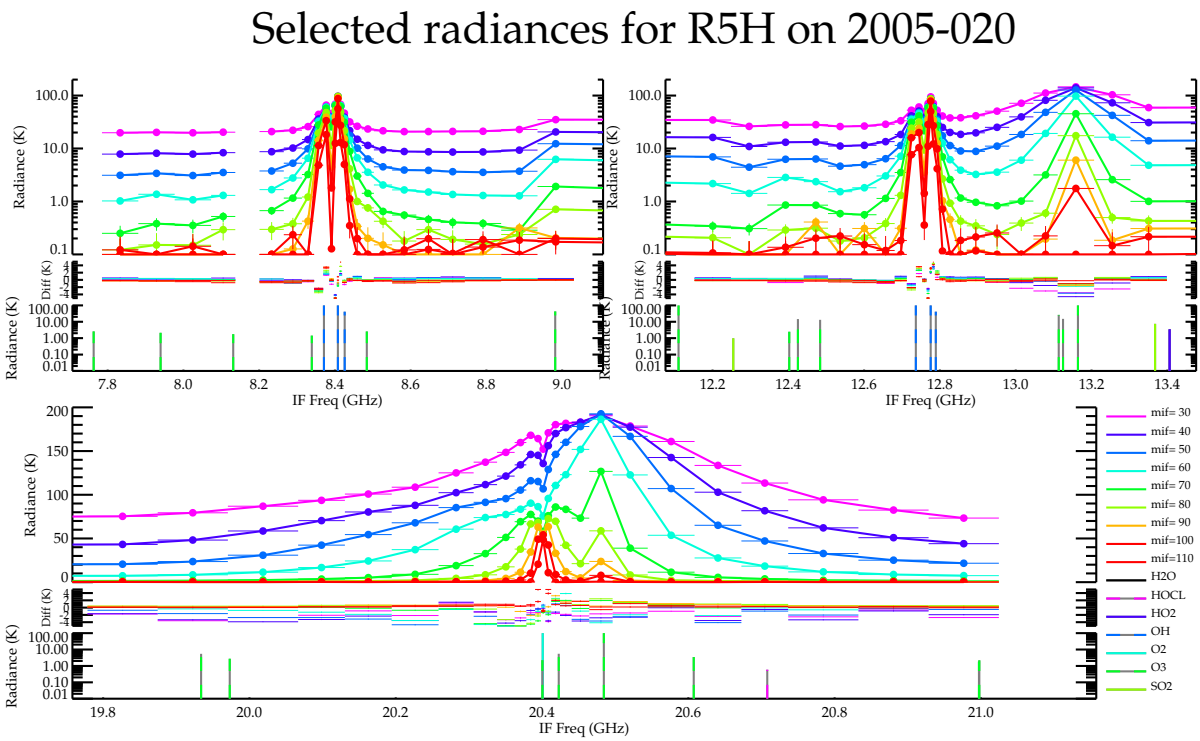

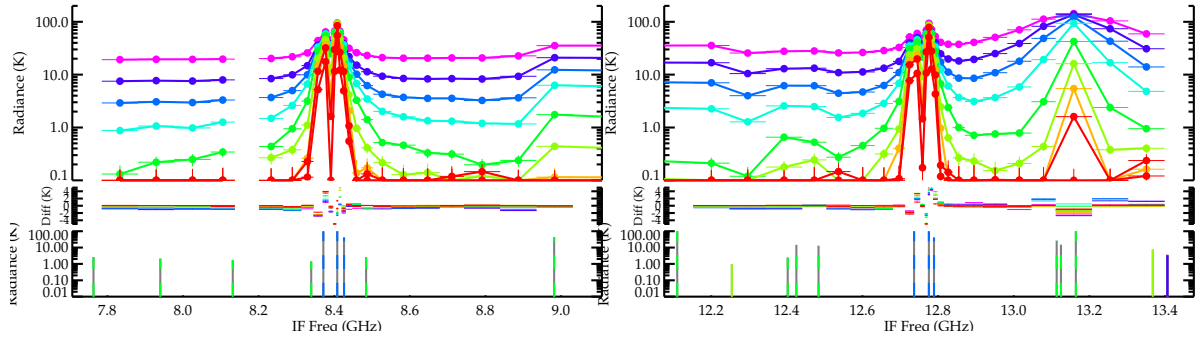

Fig. 15. Same as Fig. 12 but for EOS MLS R5H and R5V radiometers measuring orthogonal polarizations of the same spectral coverage. The local oscillator frequency is 2522781.6 MHz. These are double sideband radiometers. In normal science mode, filter bank 20 of R5V measuring O_2 is switched to another radiometer and is not shown. See text for further discussion.